UNIVERSIDAD DE INVESTIGACIÓN DE TECNOLOGÍA EXPERIMENTAL YACHAY

Escuela de Ciencias Físicas y Nanotecnología

TÍTULO: Synthesis of Graphene species in a simulated non-terrestrial environmental condition

Trabajo de integración curricular presentado como requisito para la obtención
del título de Física

Autor:

Dávila Porras Angie Carolina

Tutor:

Ph.D.- Chacón-Torres Julio

Urcuquí, junio de 2024

Autoría

Yo, **Dávila Porras Angie Carolina**, con cédula de identidad 0750548588, declaro que las ideas, juicios, valoraciones, interpretaciones, consultas bibliográficas, definiciones y conceptualizaciones expuestas en el presente trabajo; así cómo, los procedimientos y herramientas utilizadas en la investigación, son de absoluta responsabilidad de el/la autora (a) del trabajo de integración curricular. Así mismo, me acojo a los reglamentos internos de la Universidad de Investigación de Tecnología Experimental Yachay.

Urcuquí, junio de 2024.

_____
Angie Carolina Dávila Porras
CI: 0750548588

Autorización de publicación

Yo, **Dávila Porras Angie Carolina**, con cédula de identidad 0750548588, cedo a la Universidad de Investigación de Tecnología Experimental Yachay, los derechos de publicación de la presente obra, sin que deba haber un reconocimiento económico por este concepto. Declaro además que el texto del presente trabajo de titulación no podrá ser cedido a ninguna empresa editorial para su publicación u otros fines, sin contar previamente con la autorización escrita de la Universidad.

Asimismo, autorizo a la Universidad que realice la digitalización y publicación de este trabajo de integración curricular en el repositorio virtual, de conformidad a lo dispuesto en el Art. 144 de la Ley Orgánica de Educación Superior

Urcuquí, junio de 2024.

Angie Carolina Dávila Porras
CI: 0750548588

Dedication

To Rosita, Mauricio, and Bertha.

*This work symbolizes my sincere gratitude for the invaluable
support and trust you had in me over these years.*

Angie Dávila Porras

Acknowledgements

Resumen

El grafeno ha llamado la atención de muchos investigadores de todo el mundo debido a sus propiedades mecánicas, electrónicas y ópticas, que se han utilizado para elaborar nuevos materiales electrónicos. Este material no crece de forma natural en la Tierra, por lo que se han desarrollado varios métodos para su síntesis. Sin embargo, nuevos estudios revelaron la formación de grafeno a nanoescala en dos meteoritos de tipo CV3 ricos en carbono: QUE 94366 y Allende. Este hecho ha llamado la atención por descubrir cómo pudo haberse formado el grafeno en el espacio exterior. Este trabajo se basa en la simulación de la envoltura circunestelar (CSE) de una estrella de la rama gigante asintótica (RGA) rica en carbono, la cual es aproximada mediante deposición química de vapor (CVD) sobre un sustrato no cristalino de 6H-SiC compuesto por granos de diferentes tamaños: i) tamaño 1 (>180 µm, <700 µm), ii) tamaño 2 (>90 µm, <190 µm), y iii) tamaño 3 (>30 µm, <90 µm). Considerando la abundancia de gas hidrógeno en el espacio, la presencia de metano cerca de las estrellas ricas en carbono, y el ambiente inerte del espacio exterior, las muestras fueron expuestas a los gases de hidrógeno (H_2) y argón (Ar), y precursores de carbono como el metano (CH_4), a diferentes flujos de gas y una temperatura de 1000 °C. Las muestras sintetizadas se caracterizaron mediante espectroscopía Raman y difracción de rayos X (DRX), las cuales mostraron la presencia de la huella digital de grafeno sobre los granos de 6H-SiC. Finalmente, se demostró que en condiciones extraterrestres se puede formar grafeno defectuoso incluso a temperaturas de hasta 1000 °C, concretamente en la envoltura de las estrellas RGA ricas en carbono. Además, el tamaño del grano no es un factor determinante para el crecimiento del grafeno, pero los gases que fluyen a su alrededor se convierten en un factor extremadamente relevante a considerar para explicar la formación del grafeno en el espacio exterior.

Palabras clave: Carburo de silicio, Espectroscopía Raman, deposición química de vapor, rama asintotica gigante, estrellas ricas en carbono, Grafeno, envoltura circunestelar.

Abstract

Graphene has caught the attention of many researchers worldwide because of its unique mechanical, electronic, and optical properties, which have been used to develop novel electronic materials. It does not grow naturally on Earth, as a result, various methods for its synthesis have been developed. Nevertheless, new studies revealed the formation of nanoscale graphene in two different ancient CV3-type carbonaceous meteorites: QUE 94366 and Allende. This fact has caught the attention of finding how graphene could have been formed in outer space. This work is based on the simulation of the circumstellar envelope (CSE) of a carbon-rich asymptotic giant branch star (AGB) approximated via chemical vapor deposition (CVD) over a non-crystalline substrate of 6H-SiC composed of grains of different sizes: i) Size 1 (>180 µm, <700 µm), ii) Size 2 (>90 µm, <190 µm), and iii) Size 3 (>30 µm, <90 µm). Considering the abundance of hydrogen gas in space, the presence of methane near the carbon-rich star, and the inert environment of outer space, the samples were exposed to various carrier gasses such as hydrogen (H_2) and argon (Ar), with carbon precursors as methane (CH_4), at different flow rates and a temperature of 1000 °C. The synthesized samples were characterized via Raman spectroscopy and X-ray diffraction (XRD), which showed the presence of the graphene fingerprint over the 6H-SiC grains. Finally, it was demonstrated that defective graphene can be formed under extraterrestrial conditions even at temperatures up to 1000 °C, specifically in the envelope of carbon-rich AGB stars. Furthermore, grain size is not a determining factor for growing graphene, but the gasses flowing around become an extremely relevant factor to be considered to explain the formation of graphene in outer space.

Keywords: Silicon carbide, Raman spectroscopy, chemical vapor deposition, asymptotic giant branch, carbon-rich stars, Graphene, circumstellar envelope.

Contents

List of Figures

List of Tables

Chapter 1

Introduction

Nowadays, graphene has called the attention of many researchers worldwide because of its unique mechanical, electronic, and optical properties, which have been used to develop novel electronic materials such as transparent conductive electrodes, photodetectors, and light-emitting devices[1]. However, this promising material does not grow naturally on Earth. For this reason, various methods of synthesis of graphene have been developed by scientists, such as CVD growth on transition metals[2–4], micromechanical exfoliation or scotch tape method[5], thermal decomposition of Silicon Carbide (SiC)[6–9], among others, which are carried out under specific parameters that can affect the quality of graphene produced. These parameters are time, the flow rate of the precursor gasses (e.g. methane, hydrogen), types of substrates used, (e.g. metals, carbides), etc.

Nevertheless, it has become very surprising the fact that new studies revealed the formation of nanoscale graphene in two different ancient CV3-type carbonaceous meteorites: within a chondrule inclusion in QUE 94366 meteorite, and inside a refractory Calcium-Aluminum-Inclusion (CAI) rim in Allende meteorite[10]. This unexpected discovery has caught the attention of many researchers to find how graphene could have been formed in outer space. However, the specific possible scenarios that could have led to its formation remain a mystery.

Beyond the borders of Earth, there exists a rich environment of chemical structures and molecules that can not be found naturally there: the extraterrestrial medium. Among the elements coexisting in this medium, the formation of carbon constitutes an important hint for the growth of graphene. Carbon (C) is an element exclusively formed in the hot interiors of stars and expelled into the interstellar environment to be part of the stellar dust, from which $\sim 80\%$ has been incorporated into gaseous polycyclic aromatic hydrocarbon (PAHs) and other carbon derivatives such as nanodiamonds, fullerenes, amorphous carbon,

1

graphite, silicon carbide (SiC), among others[11]. Even though carbon atoms are the overall component of graphene, it is not enough to make it grow. The substrate has to accomplish Some specific features such as surface orientation, negligible carbon precursor decomposition, low surface irregularities, internucleation distance[12], substrate remotion/depletion rate[13], etc.

Following the previously said, SiC is the best extraterrestrial substrate for the formation of graphene since this material is commonly used as a substrate for the epitaxial growth of graphene (EG)[13]. This is due to the facility it has to produce large-scale monolayer graphene[14]. Moreover, this carbide is the best-studied presolar grain in meteorites because of its relatively large grain size and high abundance found in ancient meteorites[15]. Also, it has been detected in the proximities of Asymptotic Giant Branch (AGB) carbon-rich stars[16], providing significant information on the physical and chemical conditions occurring in the circumstellar envelope (CSE) of carbon-rich stars (C-stars), as well as on the internal nucleosynthesis processes[17] they suffered.

The aim of this work is to give a proposal of the possible conditions that could give way to the formation of graphene in outer space after doing a deep search of the possible extraterrestrial sources and stellar dust components that could help to the growth of graphene in this medium. Following this purpose, the viability and required conditions for graphene formation in outer space is experimentally proved by approximating an extraterrestrial-controlled environment in the laboratory of Yachay Tech University.

1.1 General and Specific Objectives

1.1.1 General Objective

The main goal of this work is to synthesize graphene species on a poorly controlled surface, simulating an extraterrestrial environment by adapting extraterrestrial conditions to a simulated system in the laboratory of our university, in order to justify and prove the potential formation of graphene species without the presence of highly controlled human systems.

1.1.2 Specific Objectives

- To determine the proper conditions (temperature, gasses, time, and pressure) for growing graphene.

- To synthesize graphene on silicon carbide (SiC) by Chemical Vapor Deposition (CVD) and thermal decomposition of SiC.

- To characterize Graphene species using Raman Spectroscopy and XRD techniques.

- To determine the purity of the graphene samples obtained by analyzing its number of layers and level of defects, by using the FWHM principle and I_D/I_G ratio, respectively.

- To investigate the possibility of forming graphene in an extraterrestrial environment.

Chapter 2

Theoretical Background

The following section gives a brief introduction to the core of this research, starting from the mean features of chondrites, the properties of graphene, SiC as a presolar grain, and the existence of carbon allotropes in space with the favorable conditions necessary for their formation Also, each of the methods used for the synthesis and characterization of silicon carbide (SiC) and graphene are shown.

2.1 Chondrites

A meteorite is an astronomical body, defined as a single unit of matter existing in the universe. They are rocky remnants of asteroids (or comets) that have fallen on Earth[18]. Chondrites are the largest classification of meteorites[19] that provide unique clues for the origin of the solar system. They are named after the once-molten and quasi-spherical singularities of millimeter size (~ 0.01–10 mm)[20] embedded inside their matrix, called as chondrules[21]. Matrix is composed of a mixture of fine-grained materials (10 nm to 5 μ m) formed in diverse locations of the Solar System, that coats refractory inclusions (e.g. CAIs, AOA) and chondrules[22]. These chondrules are highly composed of low-Ca pyroxene ($Mg_xFe_{1-x})_2SiO_3$, olivine ($Mg_xFe_{1-x})_2SiO_4$, with x=Mg/(Mg+Fe) ratio[22], metallic iron (Fe), and nickel (Ni)[20], with a characteristic crystallization rate of hours or minutes, between ~ 1300 K and ~ 1800 K[22].

They also contain refractory inclusions, small features (tens of micrometers to centimeters) resistant to any stimulus, which are the products of high-temperature processes of melting (~ 1800 K), evaporation (≥ 1800 K)[21], and condensation[20]. These inclusions are entirely composed of metallic Fe and Ni grains, fine-grained olivine, aluminum-diopside, spinel, anorthite, and a rare melilite for Amoeboid Olivine Aggregates (AOA), and crystalline silicates and oxides rich in Calcium (Ca), Aluminium (Al), and

Titanium (Ti) for Ca–Al-rich inclusions (CAIs)[20]. An example of the presence of chondrules, CAIs, and matrix can be seen in Figure 2.1 which corresponds to samples of (a) Murchison and (b) Allende chondrites.
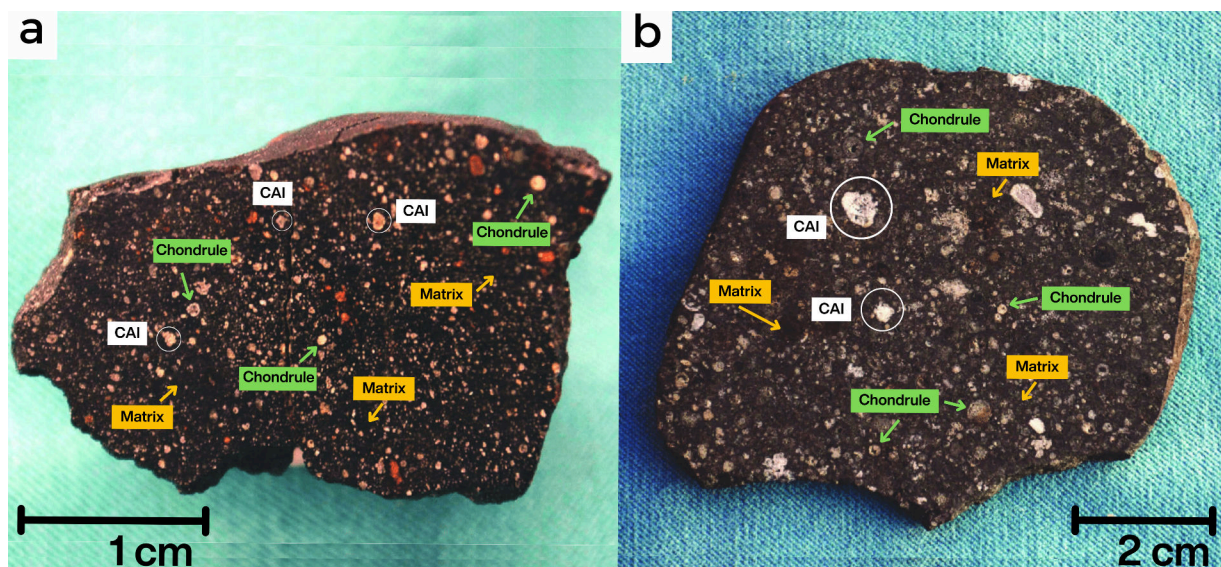
Figure 2.1: **Murchison and Allende carbonaceous chondrites.** (a) A sample of a wedge-shaped endpiece of Murchison (CM2) chondrite (20 g) and (b) a sample of Allende chondrite (32.7 g) are presented, showing their most characteristic components: CAIs within white circles, chondrules pointed in green, and their dark matrix pointed in yellow. © Adapted from Shanos (2016)[23].

In general, the importance of chondrites relies on the history of their origin, since they resemble the heavy elements composition of the sun and the first steps of the nebular disk turning into the planets of the solar system and the sun itself[21], which explicitly says that chondrites were assembled from the solids of the nebular disk that formed the sun (solar nebula). This fact helps to determine the age of the sun, which accreted 4.56 billion years ago[21]. Regarding the classification of chondrites, there exist about 15 groups, from which 13 are classified into 3 classes: ordinary (LL, H, and LL), carbonaceous (CM, CI, CV, CO, CR, CH, CK, and CB) and enstatite (EL and EH)[20]. In this section, the nature and composition of the most important carbonaceous chondrites for this work will be detailed next.

2.1.1 Carbonaceous chondrites

Carbonaceous chondrites are dark color, fine-grained C-rich meteorites[24]. They are the most primitive meteorites yet found that have survived to the processes within the solar nebula[25]. They are sub-classified depending on their refractory elemental abundances[20], which depends on the processes they suffered during their formation. Carbonaceous chondrites were first subdivided into three different types I, II, and III, which depended on carbon and water abundances, to later designate them as C1, C2, and C3 types[26]. The C3-type was divided into 2 subtypes, Vigarano C3(V) and Ornans C3(O), considering its petrographic composition, in addition to the CM, CI, CR, CH, CK, and CB subtypes[20]. Petrographic types range from 1 to 6, where n=3 indicates a small secondary processing (i.e. temperature), n<3 indicates an increase in aqueous alteration (presence of water), while n>3 indicates a high thermal metamorphism[18]. A summary of the main types of carbonaceous chondrites for this work is seen in Table 2.1.

Group	Type	Components	Description
CI	1	Fine-grained matrix of hydrated ferromagnesian silicates[24] and olivine "rich" lithologies[27]	Lack of chondrules[24]
CM	1-2	Fine-grained matrix of hydrated ferromagnesian silicates[24]	Small (< 0.5 mm) chondrules
CV	3	Larger amounts of fine-grained ferromagnesian matrix material[24]	Larger chondrules (0.5-2 mm) and abundant refractory CAIs (> 1 mm)[24]
CO	3	Minor amount of interstitial matrix of ferromagnesian silicates (mainly olivine)[24]	Small closely-packed chondrules (< 0.5 mm)[24]

Table 2.1: Classification of group, type, chemical composition, and features of carbonaceous chondrites

The chemical variations between the different types of chondrites are attributed to their refractory elements (found in CAIs), magnesium silicates formation, metallic Fe and Ni condensation, and moderately/highly volatile elements[22]. A short description of some of the best known carbonaceous chondrites is described below.

Murchison Meteorite

This ancient meteorite has its origin in Murchison, Australia, where hundreds of primitive meteorites fell on the Earth's surface in 1969[28]. It is one of the best studied chondrites due to the large amount of sample material available. Also, it has a classification of CM petrologic type 2[29], which indicates an uniform and

low degree of aqueous (water)[30] and less thermal alteration[29]

This chondrite contains a matrix composed of intermittent porphyroblasts of olivine and/or pyroxene, surrounded by a small number of chondrules[31], metals, sulfides, oxides, carbonates, and CAIs[29], see Figure 2.1 (a). Additionally to these components, a small percentage (2%) of the total carbon distribution in this chondrite is represented by interstellar grains of diamonds (400 ppm), silicon carbide (7 ppm), fullerenes ($\geq$ 400 ppm), and graphite (<2 ppm), as well as carbonate minerals (2-10 %), aminoacids (>10 ppm), among others[32].

Allende Meteorite

Allende is a CV type 3 chondrite[33] characterized to have dark lithic chondritic clasts[34]. It fell on the Earth's surface in Pueblito de Allende, a town in Chihuahua state, Mexico, on February 8, 1969[35], from which it gets its name. Its composition (in vol %) consists of amoeboid olivine inclusions (3.2 %), chondrules (43 %), CAIs (9.4 %), matrix (38.4 %), lithic and mineral fragments (2.9 %), and opaque minerals (3.1 %)[36], see Figure 2.1 (b) . Furthermore, it also has rims grown in its matrix, which encloses fragments of olivine chondrules[34] and dark inclusions, as seen in Figure 2.2 (a). Allende has an anhydrous mineralogy (no presence of water), except for some hydrous phases. However, Allende is not a pristine chondrite, since its original mineralogy has been modified in a different number of ways through various alteration processes[36].

Two types of models have been proposed for the formation of their dark inclusions: nebular and asteroidal. In the nebular one, these inclusions are a combination of nebular condensates that experienced high-temperature reactions within the nebular gas, while in the case of the asteroidal one, they are fragments that experienced alteration in the presence of an aqueous environment at temperatures < 300°C.[34].

Murray Meteorite

Murray is a CM type 2 chondrite that fell in Calloway County, Kentucky in 1950 as a group of stones[37]. It contains (in vol %): matrix (59%), monomineralic grains (mostly olivine) (21%), chondrules (14%), refractory inclusions (5%), and metallic Fe-Ni. sulfide and magnetite (1%)[37]

QUE 94366 Meteorite

QUE 94366 is a CV type 3 chondrite discovered in Queen Alexandra Range, Antarctica in 1994 by the US Antarctic Search for Meteorite Program[10]. It is tiny and almost covered with a dull, black crust, composed of small areas of crystalline material[38]. The examination of a thin section of this chondrite shows irregular

granular aggregates and very small chondrules (~ 1.2 mm), and a brown-black matrix. Its chondrules and aggregates are mostly composed of olivine, iron-rich serpentine, and other phyllosilicates, as well as trace amounts of Ni-Fe and troilite[38]. In Figure 2.2 (b), the presence of
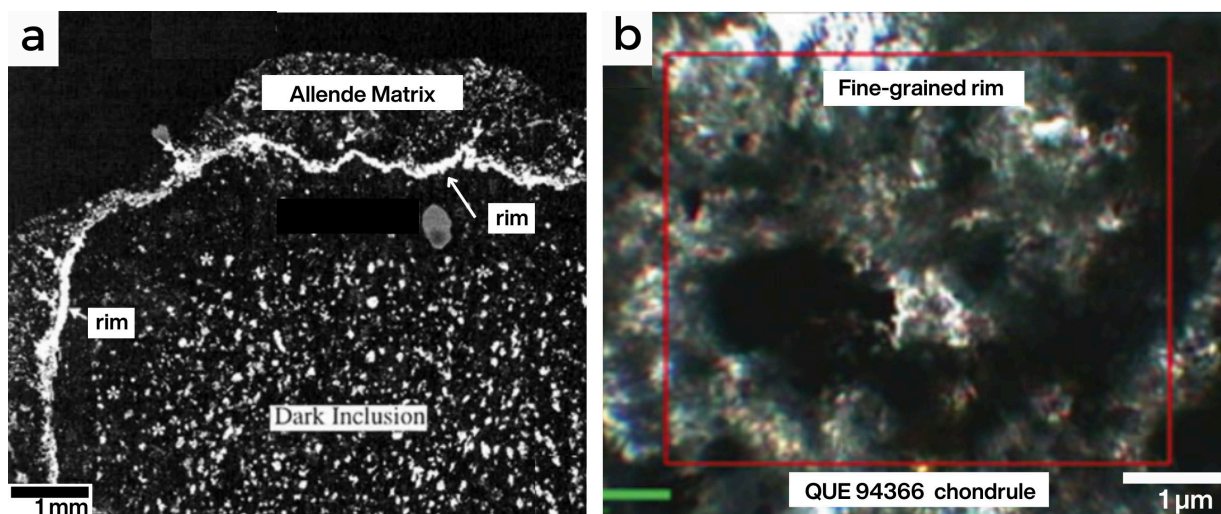
Figure 2.2: **Characteristic components in Allende and QUE 94366 carbonaceous chondrites.** (a) X-ray map in Ca of an Allende dark inclusion sample. It can be seen a large Ca-rich rim surrounding a dark inclusion[34]. (b) Transmitted light microscopy micrograph of a fine-grained rim on a chondrule in the QUE 94366 chondrite[39]. © Adapted from A. N. Krot et. al. (2000), and T. Dieing, et. al. (2011).

2.2 Graphene: A 2D Carbon allotrope

Graphene is a 2D material formed by the arrangement of hexagonal rings (honeycomb lattice) composed of carbon atoms with sp^2 bonding. It constitutes the basis of some of the most known carbon structures from 0D to 3D materials, such as fullerenes, formed by the wrapping of graphene sheets, carbon nanotubes (CNTs), formed by the rolling of graphene sheets, and graphite, built from the stacking of graphene sheets, as seen in Figure2.3. Despite this fact, graphene sheets do not share the same properties as their derivatives, differing in their conductivity and mechanical strength[40]. Among the superior properties of this material, it can be mentioned: strong ambipolar electric field effect, high thermal conductivity, high transparency (97.7%), superior carrier mobility at room temperature, good electrical conductivity, very high theoretical

specific surface area, environmental compatibility, high adsorption capacity[41], and others. This chapter is mainly dedicated to the electronic structure, properties, applications, synthesis, and characterization methods of graphene.
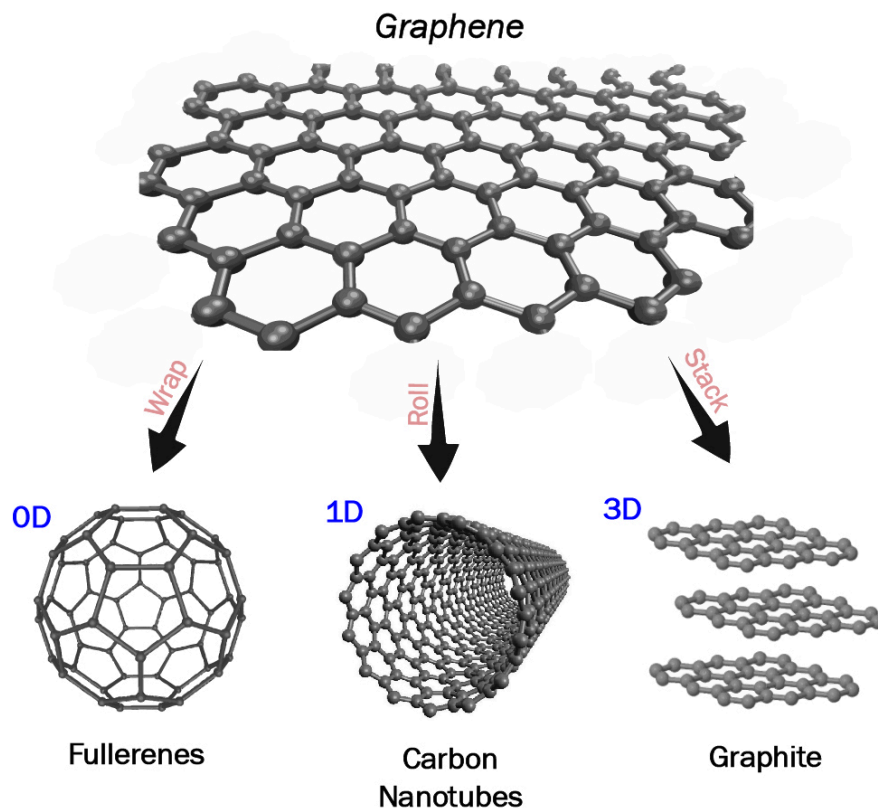
Figure 2.3: **Graphene-derived structures.** 0-dimensional fullerenes, 1-dimensional carbon nanotubes, and 3-dimensional graphite built from the wrapping, rolling, and stacking of graphene layers, respectively.

2.2.1   Principal Characteristics

Graphene is a honeycomb lattice structure with a characteristic C-C bond distance of a_{c-c}= 1.42 Å, which are linked together forming one σ bonding, see Figure 2.4 (a). Each atom conforming the graphene layer has a fourth bond on its z-direction, best called π-bonding. Later on, all of these π-bondings are hybridized together to form the π-band and π*-band[8] (bonding and anti-bonding) of graphene electronic structure, as

seen in Fig 2.4 (b).
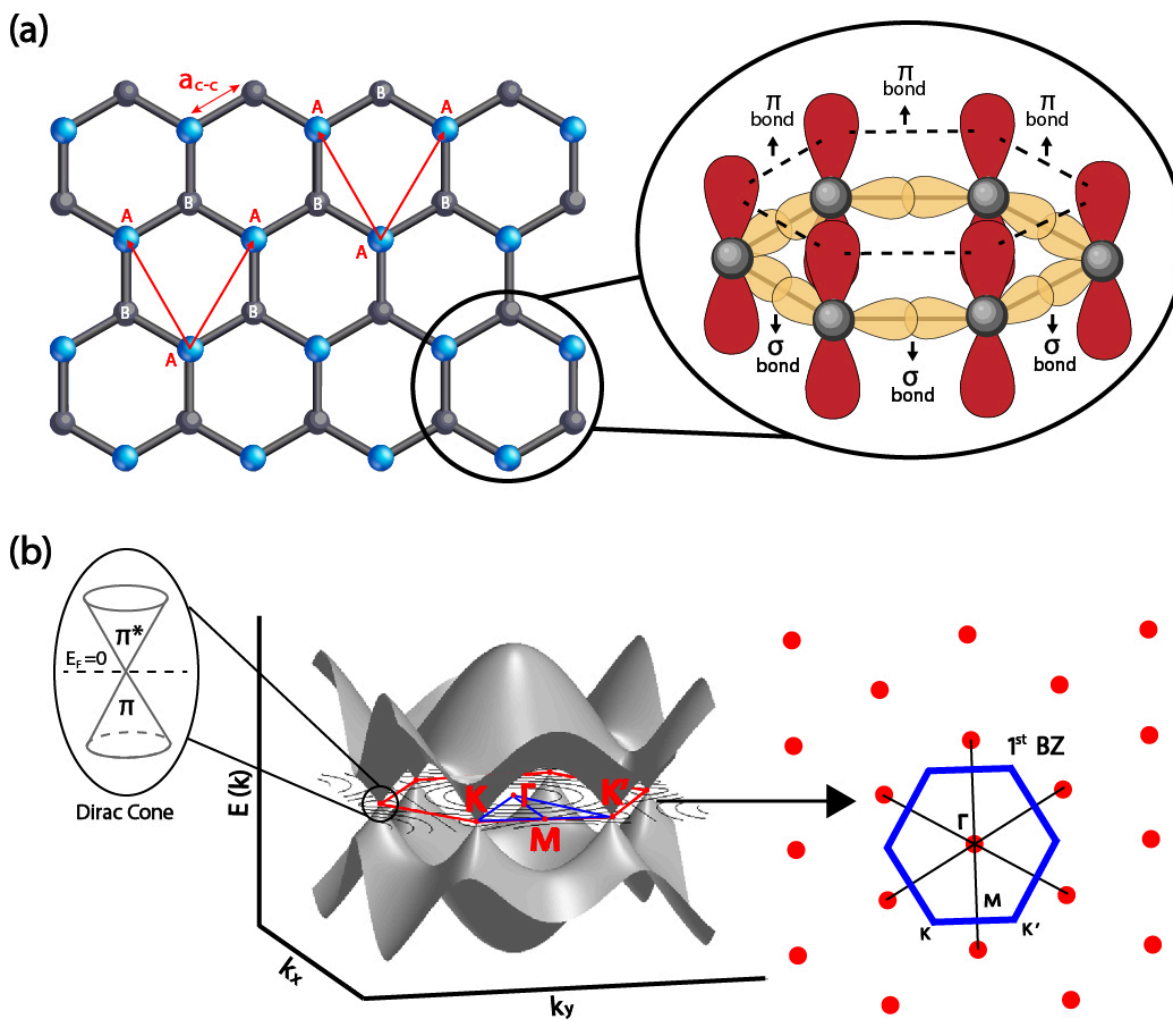
Figure 2.4: **Crystal and electronic structure of graphene.** (a) In a layer of graphene, each (A) atom has 3 nearest neighbors in (B) atoms and viceversa. (b) 3D representation of the first Brillouin zone (BZ) of graphene (horizontal plane), where K and K' are the Dirac points, M is the midpoint between K and K', while Γ is the center of the BZ[8]. Touching between bonding (π-band) and antibonding (π*-band) orbitals at the Dirac points results in the formation of Dirac cones.

Graphene has a hexagonal Bravais lattice with primitive lattice vectors that can be described as follows [42],

$$\vec{a_1} = \left(\frac{a}{2}, \frac{\sqrt{3}}{2}\right) \qquad \vec{a_2} = \left(\frac{a}{2}, -\frac{\sqrt{3}}{2}\right) \tag{2.1}$$

where their lattice constant a $=\|\vec{a_1}\| = \|\vec{a_2}\|$, is given by a= 2.46 Å, as seen in Figure 2.6 (a). The Bravais lattice is a group of points (lattice points) composed of one atom per unit cell, that are equivalent and similarly situated [43] in real space. In graphene, the hexagonal lattice is the Bravais lattice for its honeycomb structure, in which the unit cell is denoted by A and B atoms in the shaded rhombus seen in Figure 2.6 (a). Moreover, the reciprocal lattice is a "frame of reference" for describing the wave-like phenomena (i.e. electrons, photons) within a crystal [44]. Then, the best way to describe this behavior is in terms of momentum (ρ) and wavelength (λ), since they describe the transition from a particle (atoms) in real space, to a wave in reciprocal space. The relationship between these two quantities is given by the wavenumber **k**,

$$\mathbf{k} = \frac{2\pi}{\lambda} \tag{2.2}$$

which comes from the momentum of a particle defined by [44]

$$\rho = \hbar \cdot \mathbf{k} \tag{2.3}$$

In the reciprocal lattice (**k**-space), there also exists a unit cell which is defined as the First Brillouin Zone (1 BZ), see Figure 2.4 (b). It is the space between the origin (**k**=0) and the reciprocal lattice points nearest to this origin [45], see Figure 2.4 (b). It is obtained by tracing perpendicular planes into the reciprocal lattice vectors, where each vertex corresponds to the high symmetry points of the reciprocal lattice [46], see Figure 2.6 (b). The reciprocal lattice vectors of graphene are given by [42]

$$\vec{b_1} = \left(\frac{2\pi}{a}, \frac{2\pi}{\sqrt{3}a}\right) \qquad \vec{b_2} = \left(\frac{2\pi}{a}, -\frac{2\pi}{\sqrt{3}a}\right) \tag{2.4}$$

satisfying that $\vec{a_1}\vec{b_1} = \vec{a_2}\vec{b_2} = 2\pi$.

Furthermore, the relationship between kinetic energy (E) and momentum (ρ) of electrons plays an important role in analyzing the band structure of a material. The electrons in the hexagonal lattice of graphene follow a linear dispersion relation (E_G) which can be explained with the Dirac dispersion relation (E_D) for wave-like particles [42],

$$E_D(\mathbf{k}) = \pm \sqrt{m^2 c^4 + \hbar^2 c^2 |\mathbf{k}|^2} \tag{2.5}$$

where E_D is the energy dispersion, c is the speed of light, and m corresponds to the relativistic mass. This equation represents a quadratic dispersion, see Figure2.5. However, when m=0 (for massless particles), there exists a zero bandgap, as seen in Figure 2.5, so giving the resultant linear dispersion relation,

$$E_D(\mathbf{k}) = \pm\hbar c\mathbf{k} \tag{2.6}$$
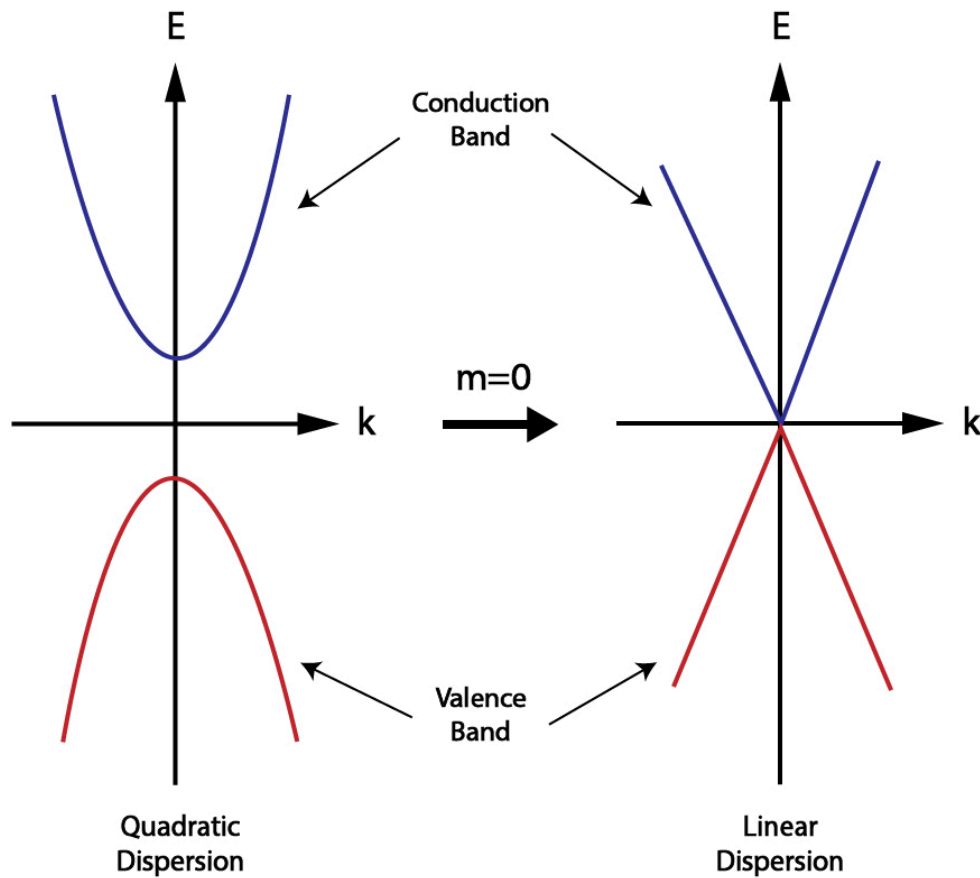
Figure 2.5: **Linear dispersion of graphene.** On one hand, when m>0, the contribution of the quadratic term in Dirac's equation, mc^2, makes the gap between valence (red) and conduction (blue) bands not to be zero, generating a quadratic dispersion (left). On the other hand, at m=0, the gap between the valence (red) and conduction (blue) bands becomes zero with a linear dispersion (right), resulting in the formation of Dirac cones.

For graphene, this linear dispersion relation becomes

$$E_G(\mathbf{k}) = \hbar v_F \mathbf{k} \qquad (2.7)$$

where $\rho = \hbar\,k$ is the momentum and $v_F = 10^6 \frac{m}{s}$ is the Fermi velocity of electrons[47], at the points (Dirac points) where valence and conduction bands touch each other. The Fermi velocity (v_F) is $\frac{1}{300}$ the speed of light[8], which corresponds to the velocity that electrons have near the highest energy level that an e^- can occupy (Fermi level), giving graphene the particularity of being a semi-metal with zero-bandgap[47]. This analogy implies that charge carriers (e^-) and holes at these Dirac points of graphene, see Figure 2.4 (c), behave like photon-like relativistic Dirac fermions with zero mass[42]. A graphical representation of the 1 BZ of graphene seen in Figure2.4 (b) shows that both bonding π and anti-bonding π^*, which correspond to the valence and conduction bands respectively, are directly meeting at the Dirac points at each energy bands K and K' at $E_F=0$[8].

(a) Direct Lattice

(b) Reciprocal Lattice
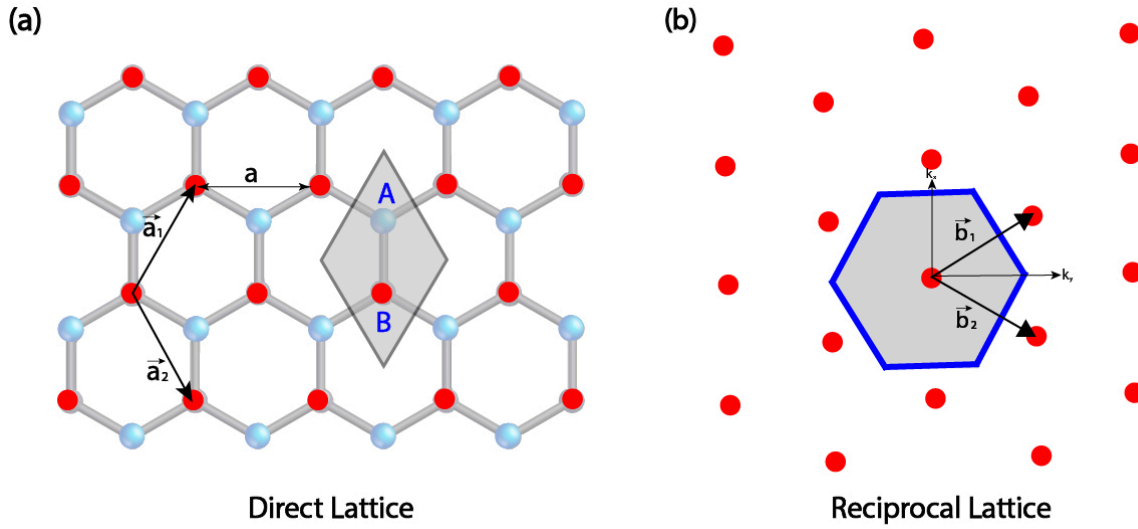
Figure 2.6: **Scheme of Bravais lattice and reciprocal lattice of graphene** (a) Atoms A and B are part of the unit cell of graphene (shaded rhombus). The red points are the position of the lattice points in the hexagonal Bravais lattice of graphene, with a basis of two atoms (one A and one B) at each lattice point. Also, its primitive lattice vectors are seen in $\vec{a_1}$ and $\vec{a_2}$. (b) Reciprocal lattice of graphene with red points indicating the reciprocal lattice points. $\vec{b_1}$ and $\vec{b_2}$ are the reciprocal lattice vectors, while the shaded region constitutes the first BZ in the reciprocal space.

2.2.2 Properties of Graphene

The exceptional behavior of e^- traveling at $\frac{1}{300}$ the speed of light (Dirac fermions), as well as its stacking geometry and π and σ bindings, are responsible for most of the peculiar properties of graphene. These properties have turned graphene into a captivating material with huge applications in different devices and industries.

Electronic properties

Electronic properties in graphene are very dependent on the number of layers, as a result, the properties shown by a one-layer, two-layer, or multi-layer graphene, are so different. In the first place, graphene has the possibility of varying charge carriers from holes to electrons[5]. This exceptional property makes this material to be able to be used in transistors, however, it is only applicable to one-layer graphene sheets since this effect decreases when the number of layers increases. In second place, transport in graphene exhibits chirality[8], referring to the inability to transform the unique linear dispersion of its band structure into another (e.g. quadratic).

Finally, in graphene, charge carriers cannot be confined by electrostatic potentials as is common in traditional semiconductors[8]. It means that an electron will turn into a hole when it hits an electrostatic barrier, then it will propagate through the barrier until it reaches the other side and turns into an electron again. This effect is best called "Klein tunneling". In general, these wonderful properties have led graphene to be widely used as a manufacture in many optical and electronic devices, such as[48] photodetectors, light-emitting diodes, solar cells, electronic sensors, biomolecule sensors, gas molecule sensors, among others.

Optical properties

Among the optical properties of graphene, it can be stated that this material absorbs ≈ 2.3 % of the white light[5]. This value increases linearly when increasing the number of layers, then for a bilayer graphene sheet, its percentage is around 4.6%. The equation determining this absorbance rate is given by,

$$A = 1 - T = \pi\alpha = 2.3\%, \tag{2.8}$$

with a fine structure constant of $\alpha \approx \frac{1}{37}$. In pristine graphene, incident photons of low energy E= $\hbar\omega$ are absorbed to excite electrons in the valence band. These excited e^-s jump to the conduction band (interband transition), passing through the E_F, as seen in Figure 2.7 (a). When the intensity of light starts to increase, the thermalized e^- will cool down and redistribute (intraband transition). Also, the

electron-hole recombination process, where an e^- occupies the position of a hole, is carried out[49] to create an equilibrium distribution. In Figure 2.7 (b), the electron-hole recombination dynamic is seen. Later, when higher excitation intensities hit a graphene layer, the photons cause the energy states close to the border of the valence and conduction bands to fill[50], blocking the absorption of light, as seen in Figure2.7 (c). This property is called saturable absorption, generated as a result of the Pauli blocking principle, which explains that two electrons can not fill the same state.
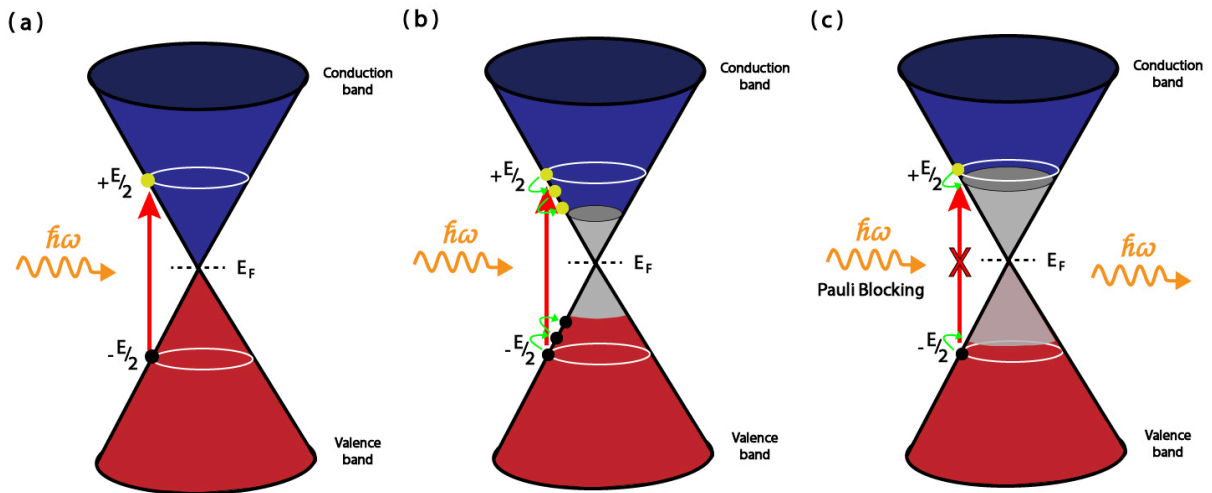
Figure 2.7: **Absorption of light in graphene.** Excitation process for absorption of light in graphene. (a) Electrons (black) from the valence band (blue) are excited to occupy the position of holes (yellow) into empty states in the conduction band (red). (b) The thermalized electrons cool down and redistribute (intraband transition) through electron-hole recombination when the intensity of light starts to increase. (c) The energy states start to fill when there are too many excited electrons as a result of very high wavelengths of excitation. It causes a saturable absorption, generated by the Pauli blocking principle. After, no more photons are allowed to be absorbed.

Also, the optical transparency of graphene helps it to be identified via optical microscopy on a Si/SiO_2 substrate[5]. Thanks to this, the number of graphene layers of a sample can be identified by different contrasts.

2.2.3   Methods of synthesis

The synthesis of graphene has become a challenge since scientists have put efforts into finding the most suitable way to produce high-quality graphene on a large scale. In this section, some of the methods used for synthesizing graphene such as[1] micromechanical exfoliation from Graphite, epitaxial growth from thermal deposition of SiC, and chemical vapor deposition (CVD), are mentioned.

CVD growth on transition metals

The working principle of this method consists of the decomposition of hydrocarbon gases such as methane (CH_4) and ethylene (C_2H_4), to grow graphene on metallic catalysts. Metals such as copper (Cu) and nickel (Ni) can catalyze the deposition of the mentioned carbon sources when heated at high temperatures of around 1000°C.

In general, one way to perform the growth of graphene on Ni[8] is to anneal the Ni foils until 1000°C in a hydrogen (H_2) environment to increase its grain size, later, there are added CH_4 and argon (Ar) gasses at atmospheric pressure during 20 mins. At this point, the hydrocarbon from methane decomposes, leaving only carbon atoms to dissolve and form a solid solution into the Ni foil[2]. Finally, the resulting Ni/C foils are cooled in Ar gas where carbon atoms start to segregate from the solid solution and precipitate on its surface to form graphene. It is important to take into account that the cooling rates of Ni substrate are very determinant for carbon segregation, so faster cooling rates result in thicker graphene layers, while slower cooling difficult for carbon to precipitate to the surface, producing thin graphene layers. Moreover, in 2018[3], Martinez-Gordillo, et.al, synthesized graphene over a Ni_2 C/Ni(111) substrate using temperatures lower than 500°C, evidently using temperatures lower than the one used by the synthesis on Cu. Ni (111) surface has been used as an excellent substrate for graphene growth since it has a similar hexagonal lattice to the one of graphene. However, it is not easy to produce a monolayer graphene due to the poor control that scientists have over its layer number and uniformity[4].

The solubility of carbon atoms in their substrate is very important to get good carbon segregation, this is the reason why scientists have tried other kinds of material as a graphene substrate. Besides, copper (Cu) has attracted attention due to its low solubility[4], low cost, excellent control of graphene layers, and good ability to be transferred[2]. The process consists of the annealing of a Cu foil in a hydrogen atmosphere at 1000 °C to later add H_2 and CH_4 gasses into the system for 30 minutes. After that, a graphene layer is formed over the Cu foil, as seen in Figure2.8 (a). Also, a SEM image of the resultant substrate + graphene in Fig 2.8 (b,c) shows the Cu and graphene grains with color contrast, where the darker flakes indicate high carbon concentration in multiple-layer graphene.
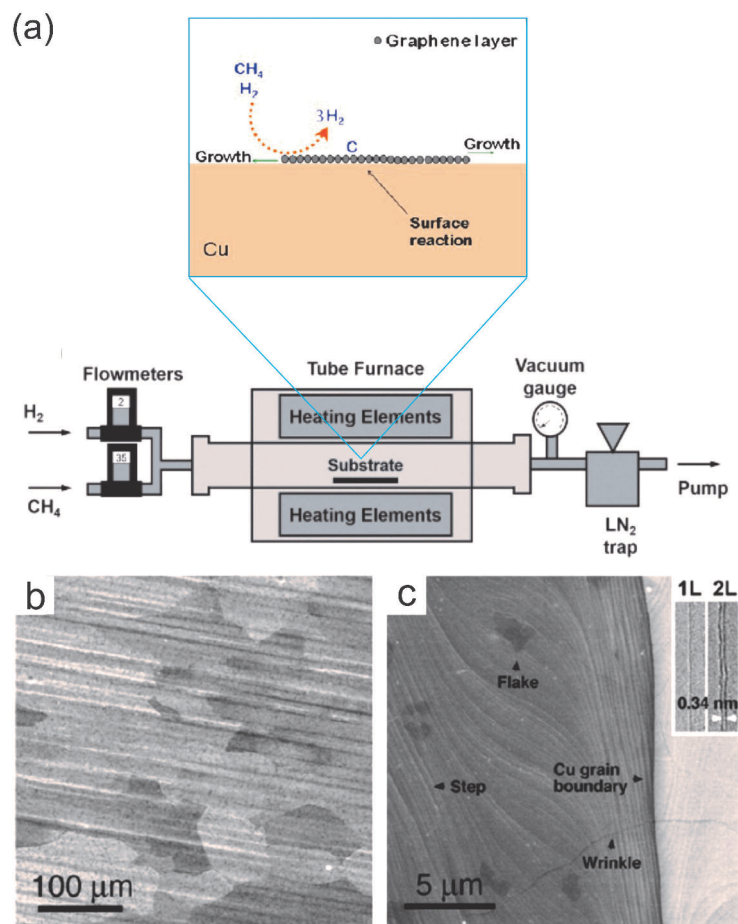
Figure 2.8: **Growing mechanism of graphene on Cu substrate** (a) Scheme of typical CVD chamber and Cu/CH_4 reactions for graphene growth. (b) SEM image of Cu + graphene foil (c) High-resolution SEM image with color contrast. The darker flakes indicate high carbon concentration in multiple-layer graphene, while Cu is seen in a light-gray color. © Adapted from Zhang et al. (2013)[2] and Li et al.(2016)[51].

Thermal decomposition of Silicon Carbide (SiC)

Graphene can also be prepared through this promising method called epitaxial growth of graphene (EG), best known as the thermal decomposition of silicon carbide (SiC). It consists of exposing 4H-SiC or 6H-SiC crystal to around 1200°C-1600 °C to sublimate its Si atoms from the surface, leaving the remaining C atoms of each SiC molecule to gather and form a hexagonal arrangement of a graphene layer[52]. Furthermore, the

physical characteristics of the resultant layer depend on the SiC surface chosen for the synthesis[6], since there exist two arrangements of Si and C atoms in SiC. On one hand, in a C-terminated face (000$\bar{1}$), the growth process is faster, in which up to 100 disordered graphene layers with domains of $\approx$ 200 nm are formed[53]. These layers exhibit defects and a specific ordering pattern with 0° and 30° rotations relative to the SiC surface[7]. On the other hand, in the Si-terminated face (0001), the growth process is slower and has small domains up to $\approx$ 30–100 nm, so that one can control the number of graphene layers. It was reported that these graphene layers are not directly grown over the SiC substrate, but instead on a 6 $\sqrt{3}$ x 6 $\sqrt{3}$ R 30° layer partially covalent bonded to the substrate (buffer layer)[7]. The thickness of graphene depends considerably on the temperature of synthesis, then in Figure 2.9, a plot showing the graphene thickness as a function of annealing temperature for a 6H-SiC (0001) surface can be seen.
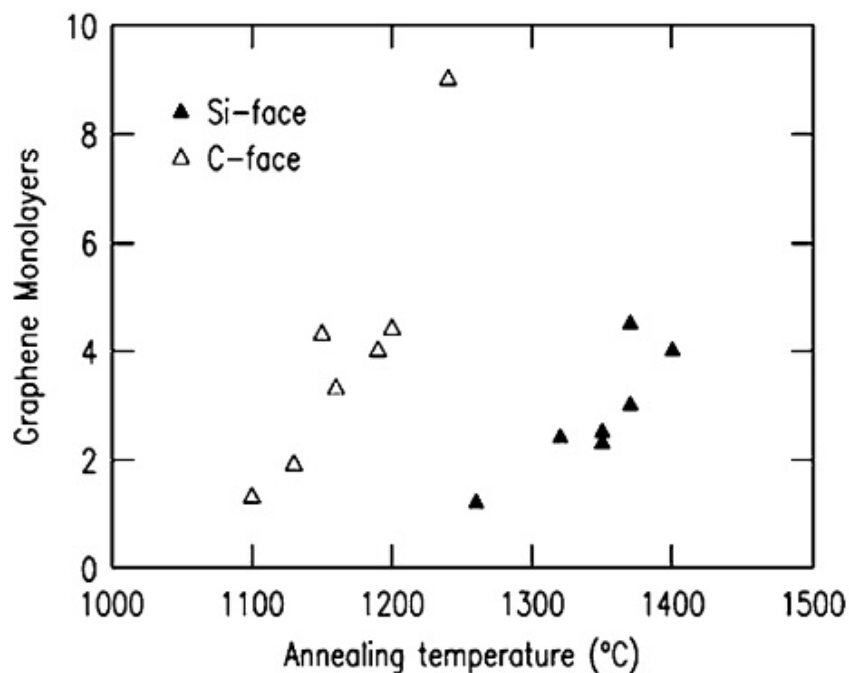
Figure 2.9: **Graphene thickness as a function of annealing temperature for 6H-SiC (0001) surfaces.** Results for both C-face (000$\bar{1}$) and Si-face (0001). © Adapted from American Physical Society (APS)

In both cases, the electron mobility is affected considerably, then in the first case, the mobility is higher than the one in the second case. SiC samples also have been synthesized at UHV as done by Walt de Heer and Claire Berger[54] in 2004. They used a 6H-SiC crystal with a Si-terminated face which was prepared

via H_2 etching in order to enhance its surface quality. Later, the sample was heated at 1000°C by electron bombardment in UHV to remove the oxidized layer to finally heat it again at 1250–1450°C. As a result, they obtained thin layers of graphene. Nevertheless, this experiment done at 900 mbar was able to reduce the surface roughness of graphene and produce much larger flakes[8]. In 1975, Van Bommel et al.[9] performed various experiments at 10^{-10} torr (UHV) and a temperature of 250°C/800°C/1000°C/1500°C on a sample of α-SiC. They reported the formation of a graphitic layer on the surface of each sample, suggesting that the collapse of the carbon atoms from three successive SiC layers is the most probable mechanism for the formation of one graphitic layer.
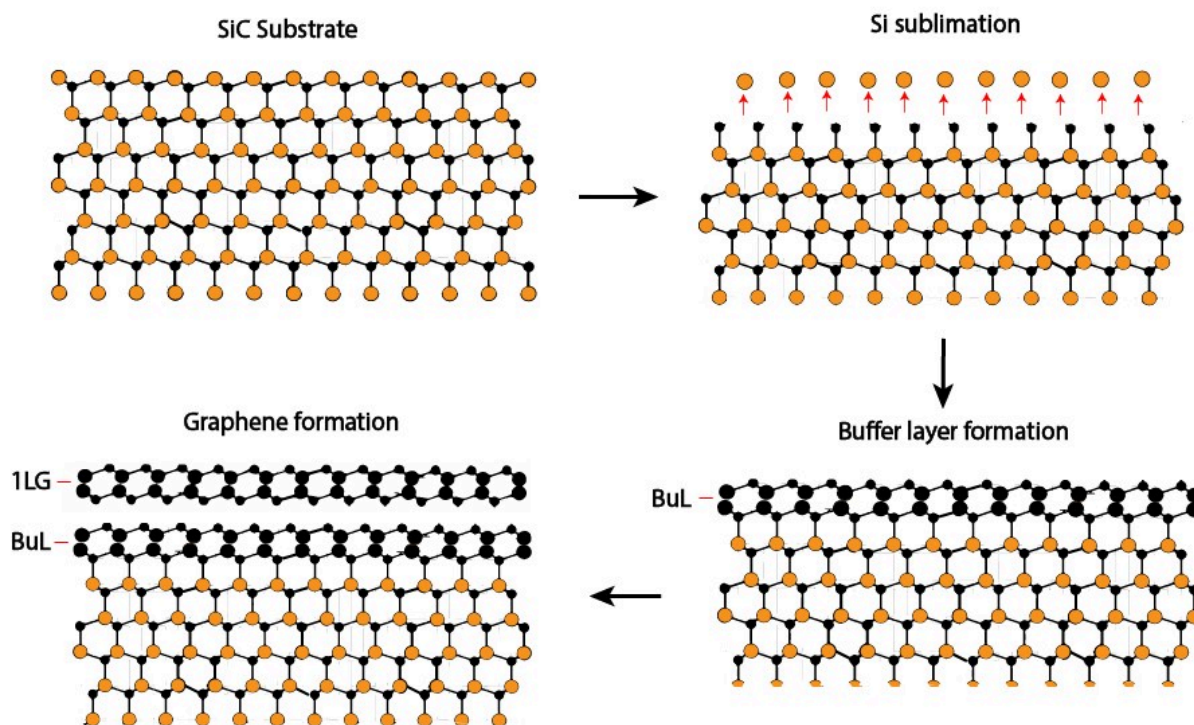
Figure 2.10: **Scheme of the thermal decomposition process of SiC with Si-face termination.** Si atoms (orange) start their sublimation process from a SiC substrate. After this, the carbon atoms (black) start to arrange forming a buffer layer (BuL) covalently bonded to the substrate. Finally, a graphene layer is formed over the BuL

In summary, the synthesis of graphene via thermal decomposition of any Si-face SiC substrate involves

the following 3 steps seen in Figure 2.10 :

1. Si sublimation carried out at an enclosure in highly controlled conditions of gas, pressure, and time.

2. Formation of a carbon-rich 6 $\sqrt{3}$ x 6 $\sqrt{3}$ R 30° layer.

3. Formation of the graphene layer over the buffer layer.

Micromechanical Exfoliation or Scotch tape method

The micromechanical exfoliation or micromechanical cleavage (MC) is so simple that there are used only two materials: one adhesive tape and some flakes of graphite. The mechanism of MC consists of the adhesion of graphite on the sticky face of the scotch tape and then peeling it off many times. The continuous peeling causes the flakes to get very clean flat surfaces, resulting in few-layer and even one-layer graphene sheets[5]. Despite it being an easy method for graphene production, its scalability and the control of its number of layers are two important problems.

2.2.4 Characterization Methods: Raman Spectroscopy

The Raman phenomenon is related to the relationship between frequency and intensity when light is scattered by the atoms present in a sample. The information that this technique gives us is related to the chemical structure, identity, phase, polymorphism, intrinsic stress/strain, contamination, and impurity of any material[55]. This technique has become widely used nowadays due to the convenience it offers in contrast to techniques involving the absorption of infrared light, such as the Fourier-transform infrared (FTIR) spectroscopy, when working with samples containing aqueous solutions[56]. The main principle of this technique relies on the molecular vibrations produced by matter. The change of frequency produced by the scattering of light, from higher to lower frequency and vice versa, can be shown as

$$v_s - v_0 = \Delta v \tag{2.9}$$

where v_0 is the frequency of the incident light and v_s is the frequency of the scattered light[57]. This magnitude, which can be both negative or positive, is called *Raman Shift* (cm^{-1}), while the set of these Raman frequencies constitutes the *Raman Spectra*. This spectra is produced when using a laser beam of high intensity which passes through a Raman Spectrometer (see Figure2.11). When the laser's beam interacts with the atoms of the sample, characteristic vibrations are produced, which are carried out in their nucleus. As a result, the energy of the scattered photon can increase or decrease[58].
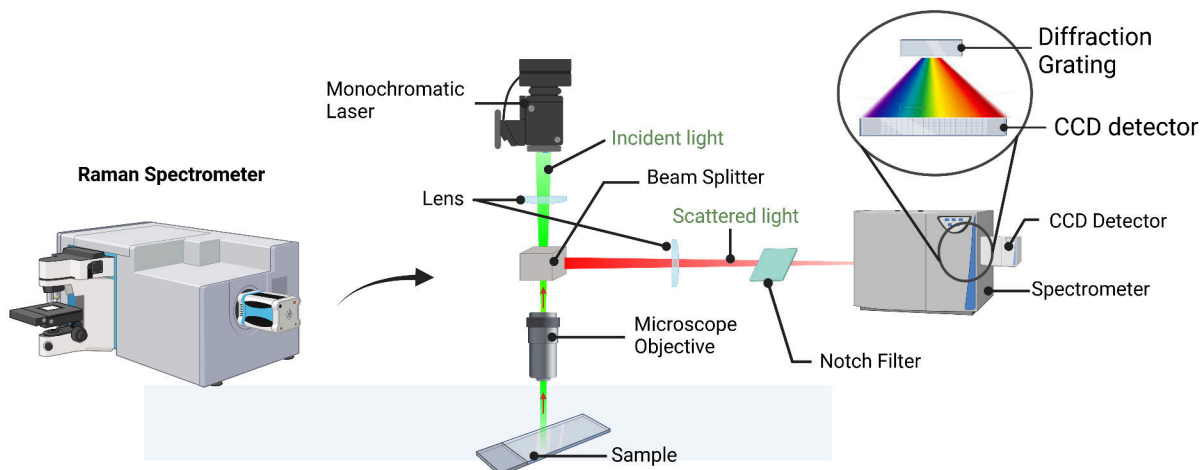
Figure 2.11: **Schematic diagram of the Raman Spectrometer working principle.** The light from a monochromatic laser passes through a convex lens, which focuses the light beam to cross a beam splitter. The microscope objective focuses the laser beam on the sample, which returns to the beam splitter to pass through another convex lens, a Notch filter, and a diffraction grating for dispersing the light into different wavelengths. Finally, the Raman scattered dispersed light is collected into a CCD sensor. *Created with BioRender.com*

In order to explain the main process carried out at Raman spectroscopy, it is important to introduce the concept of *phonons*. Phonons are considered as quasi-particles produced from the vibrations of atoms (coupled motion) in their lattice[59]. Their properties arise when interacting with photons or electrons in Raman scattering, a process of inelastic light-scattering of photons by phonons[59]. In this case, there exist two main processes for their creation and annihilation called: Stokes and anti-Stokes scattering, respectively.

Following this fact, we can have three types of scattering. The first one is carried out when electrons are excited by the photons of the laser. When the photon reaches an e^-, it makes it jump into a next energy state. However, part of the incident light is scattered from the e^-. Since electrons are light particles, these photons will be scattered with tiny frequencies, which will not produce a change in their initial energy. Consequently, an elastic process occurs when energy remains conserved. This process is called Rayleigh Scattering, see Figure 2.12. In the last two types of scattering, an energy transfer between the photon and the atom takes place (inelastic scattering) (See Figure 2.12). On one hand, an excited e^- inelastically scat-

ters and excites a phonon, consequently reducing the energy of the e^{-}[59], see Figure 2.13. At the same time, the incident photon is scattered, which energy is lower than the one of the incident photon. Consequently, we are witnessing a redshift (energy decreases) in the resultant wavelength (see Figure 2.12). This process is called *Stokes Raman scattering*. On the other hand, an excited e^{-} annihilates a phonon, which causes an increase in the energy of the e^{-}. In this case, a photon is emitted due to the transition of the e^{-} to a higher state[59], see Figure 2.13. Consequently, the incident photon is scattered with higher energy than the one of the incident photon, resulting in a blue-shift (energy increases) of the resultant wavelength (see Figure 2.12). This process is called *anti-Stokes Raman scattering*[60].
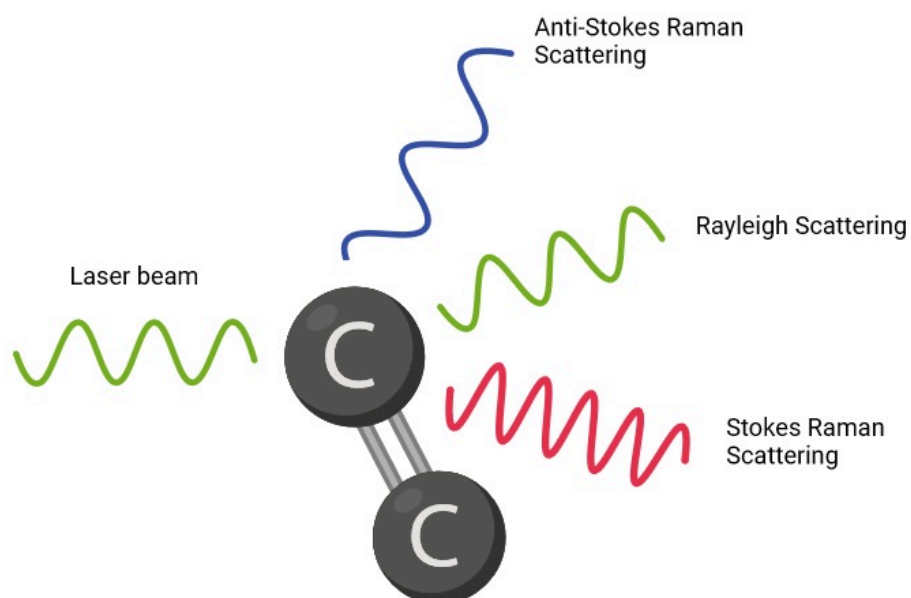
Figure 2.12: **Types of scattering produced by photons in Raman Spectroscopy.** In Stokes scattering, the resultant wavelength is redshifted due to the decrease in its energy, then its frequency increases ($v_0 > v_s$). In anti-Stokes scattering, the resultant wavelength is blueshifted, due to the increase in its energy, then its frequency decreases ($v_0 < v_s$). For the case of Rayleigh scattering, the energy and frequency of the incident beam of light remain the same as the resultant one ($v_0 = v_s$). *Created with BioRender.com*

The equations representing the change in frequency for each case can be written as

$$\nu_s = \nu_0 \tag{2.10}$$

for Rayleigh scattering.

$$\nu_s = \nu_0 + \Delta\nu \tag{2.11}$$

for Anti-Stokes scattering, and

$$\nu_s = \nu_0 - \Delta\nu \tag{2.12}$$

for Stokes scattering
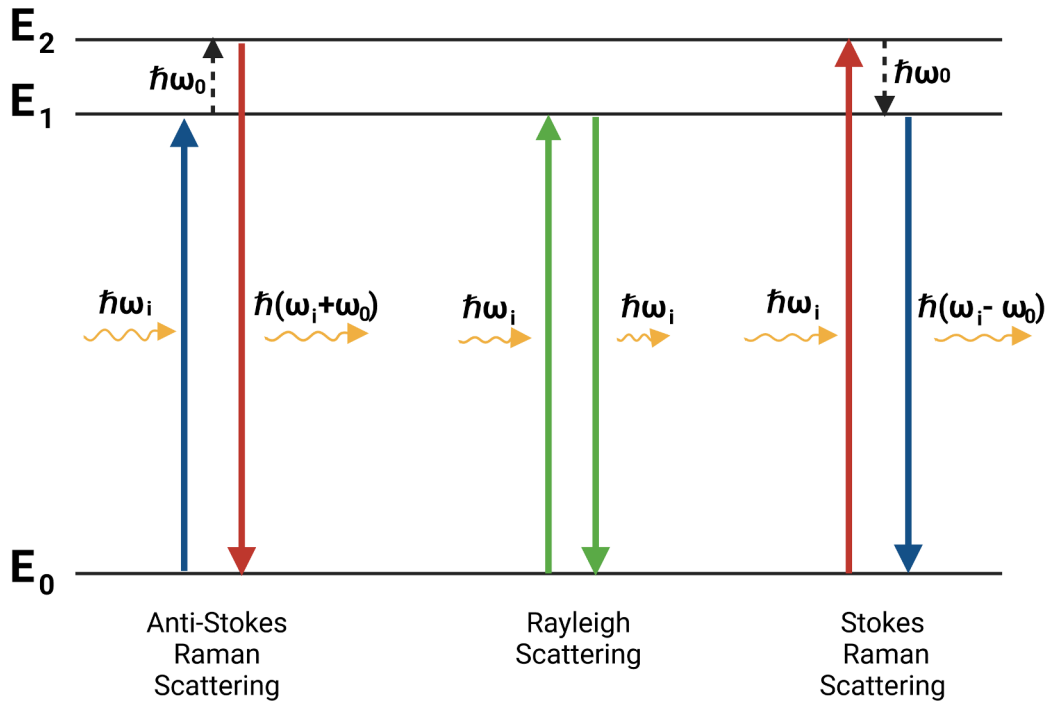
Figure 2.13: **Raman scattering processes of phonon creation and annihilation.** In anti-Stokes scattering, an incident photon ($\hbar\omega_i$) excites an e^-, which annihilates a phonon ($\hbar\omega_0$). Then the energy of the incident photon increases ($\hbar\omega_i + \hbar\omega_0$). In Stokes scattering, an e^- excites a phonon, decreasing its energy ($\hbar\omega_i$ - $\hbar\omega_0$). Finally, in Rayleigh scattering no phonon is produced, thus ($\hbar\omega_i = \hbar\omega_0$) *Created with BioRender*

The Raman spectrum of graphene has 3 principal Raman modes[61] which are produced in 2 different order Raman scattering processes, as seen in Fig 2.22. In the first one, a mean peak is produced by the G band at 1580 cm^{-1}. Moreover, in a second-order overtone, two main peaks arise, the 2D band whose peak is produced at 2690 cm^{-1} and the D band whose peak arises at 1350 cm^{-1}. The G band is provoked by the Raman active E_{2g} phonon, close to the Γ point[62] which produces an inelastic scattering, while the D band is produced by the phonons around the K point[63]. In general, both the 2D and D bands are characterized by a dispersive behavior due to the change of their frequencies in the Raman spectra which depends on the energy of the incident laser[63].

The double-resonance process (DR) for D and 2D band begins with an electron (e^-) around the K point which is excited by absorbing a photon from the incident laser. Then, an inelastic scattering is produced by a phonon which leads the scattered e^- to reach the K' point. Finally, this e^- is scattered back to the K point and emits a photon[63]. Although both processes are quite similar for 2D and D bands, there is a difference involving scattering produced by defects and phonons. For the case of the 2D band, both processes are inelastic involving two phonons[63]. Moreover, in D-band, the two processes are inelastic scattering events caused by emitting or absorbing phonons, and elastic provoked by the defects of the structure[61].

2.2.5 Defects determination and impurities

When the amount of disorder in the structure of graphene increases, the Raman intensity also increases for its three disorder bands[61]: D at 1350 cm^{-1}, D' at 1620 cm^{-1} and D+G at 2940 cm^{-1}, as seen in Fig 2.15. This figure also shows the shift of the D band to lower frequencies when its intensity starts to increase. The contrary happens to the 2D band, whose frequency increases when increasing the level of defects. One reliable way to identify the level of disorder in graphene and quantify the crystallinity of its structure is by using the I_D/I_G ratio of peak intensities[61]. It is also know as the Tuinstra-Koenig relation[64] shown in eq.(2.13),

$$\frac{I_D}{I_G} = \frac{C(k)}{L_a} \tag{2.13}$$

where I_D and I_G correspond to the intensities of the D peak and the G peak respectively. C(k) is the proportionality constant which depends on the wavelength k of the incident laser and L_a is the size of crystalline sp^2 clusters[64]. On one hand, as disorder in graphene increases, I_D/I_G will increase as there exists a high defect density which creates more elastic scattering reflected in the D band, resulting in an amorphous carbon structure[61].
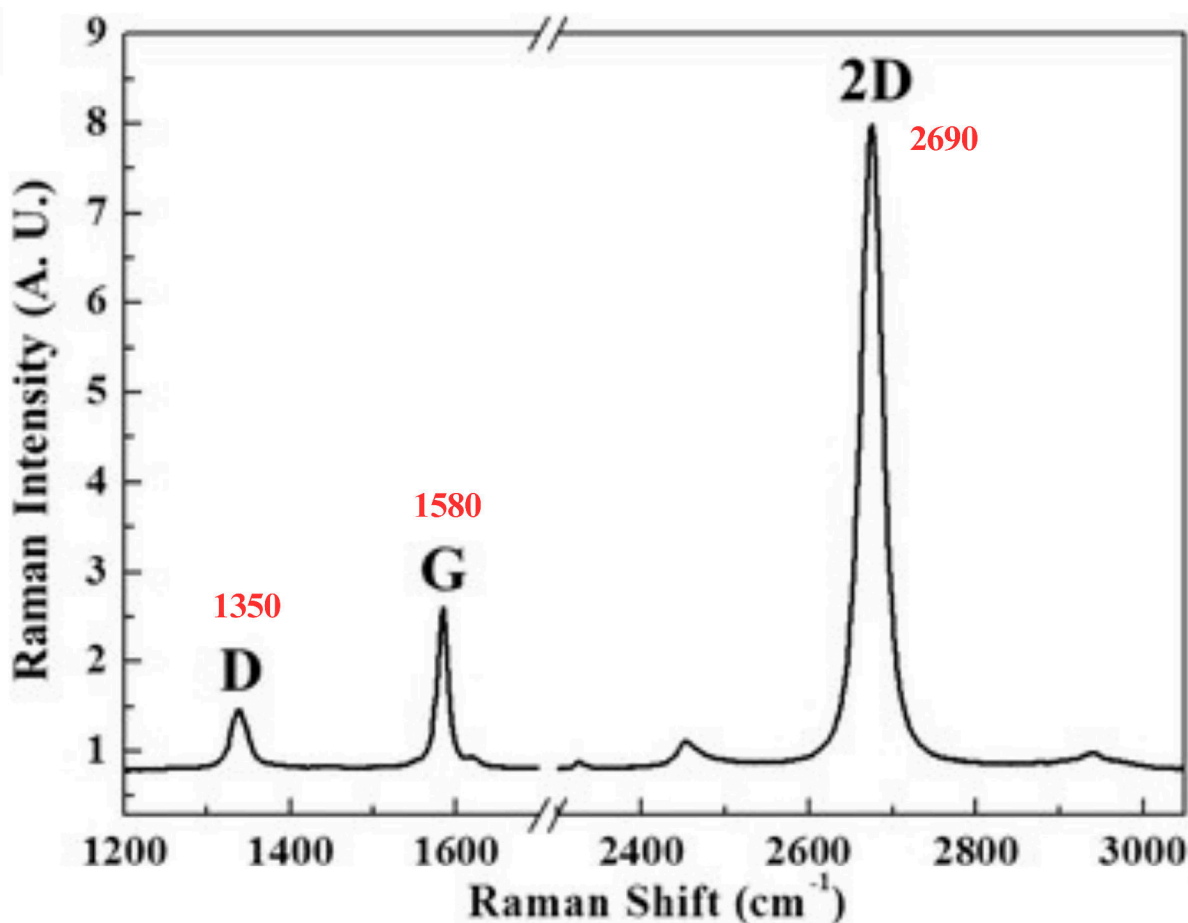
Figure 2.14: **Raman spectra of monolayer graphene with its first and second resonances processes.**
(a) Monolayer graphene's Raman spectra showing D, G and 2D bands at 1350 cm^{-1}, 1580 cm^{-1}, and 2690
cm^{-1} respectively. © Adapted from Heo G. et al. (2015)[65].

On the other hand, I_D/I_G will decrease if the number of defects in graphene is low. Illustration
Figure2.15 also shows the relationship between the I_D/I_G behavior when increasing the level of defects.
Besides, the number of layers in graphene is affected due to the synthesis method used to produce the
layers since we have poor control over them. However, D. Graf et al. (2006) suggest that the width of the
2D band can detect the difference between one-layer and multi-layer graphene[62]. This is explained due to
the increase of the width of the 2D peak, which increases with the number of layers, so that this can be

split into different subpeaks, as seen in Figure 2.16.
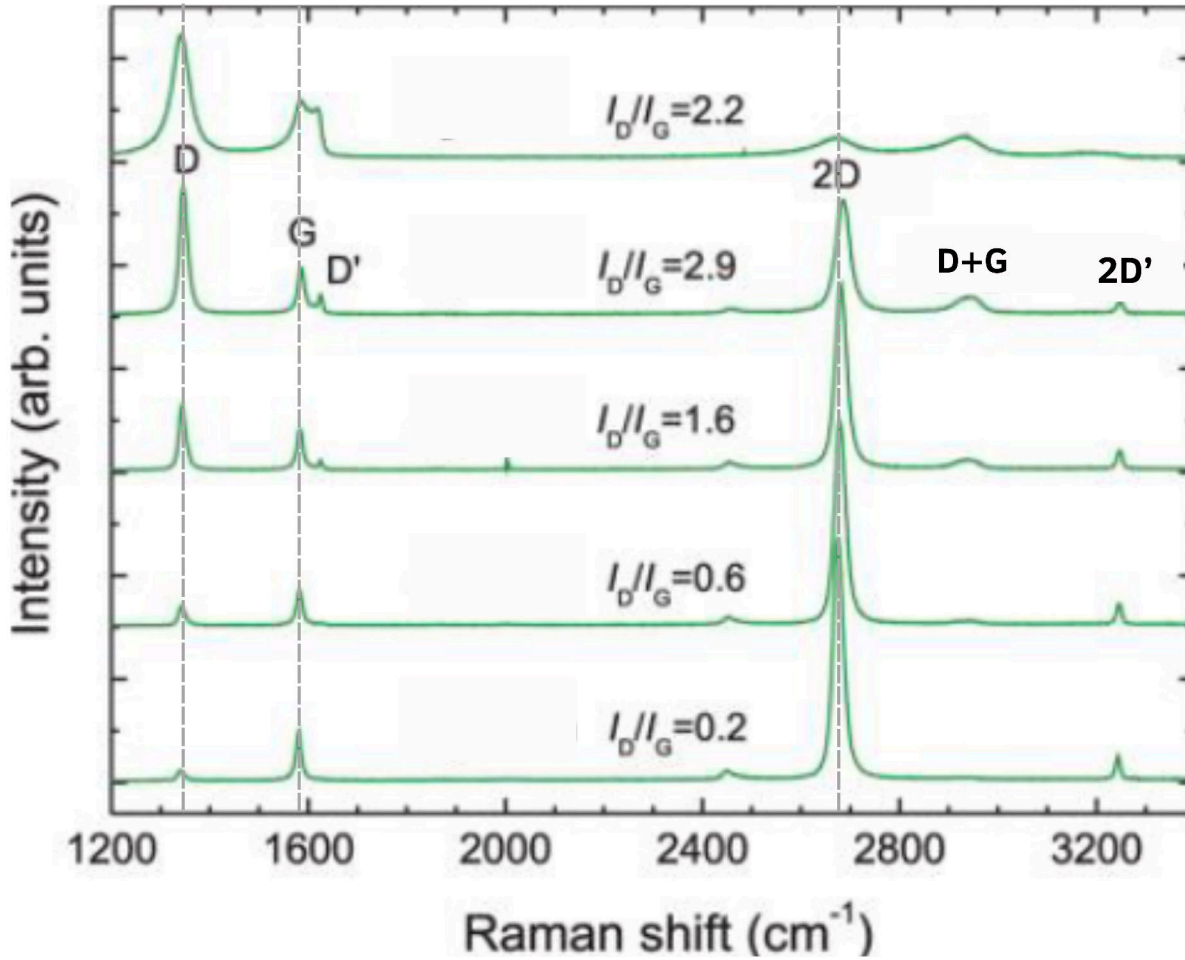
Figure 2.15: **Raman spectra and respective I_D/I_G defective graphene.** This plot shows that the I_D/I_G ratio increases when increases the intensity of the defective D band. Also, D' and D+G peaks start to arise. © Adapted from L. G. Cançado (2011)[66]
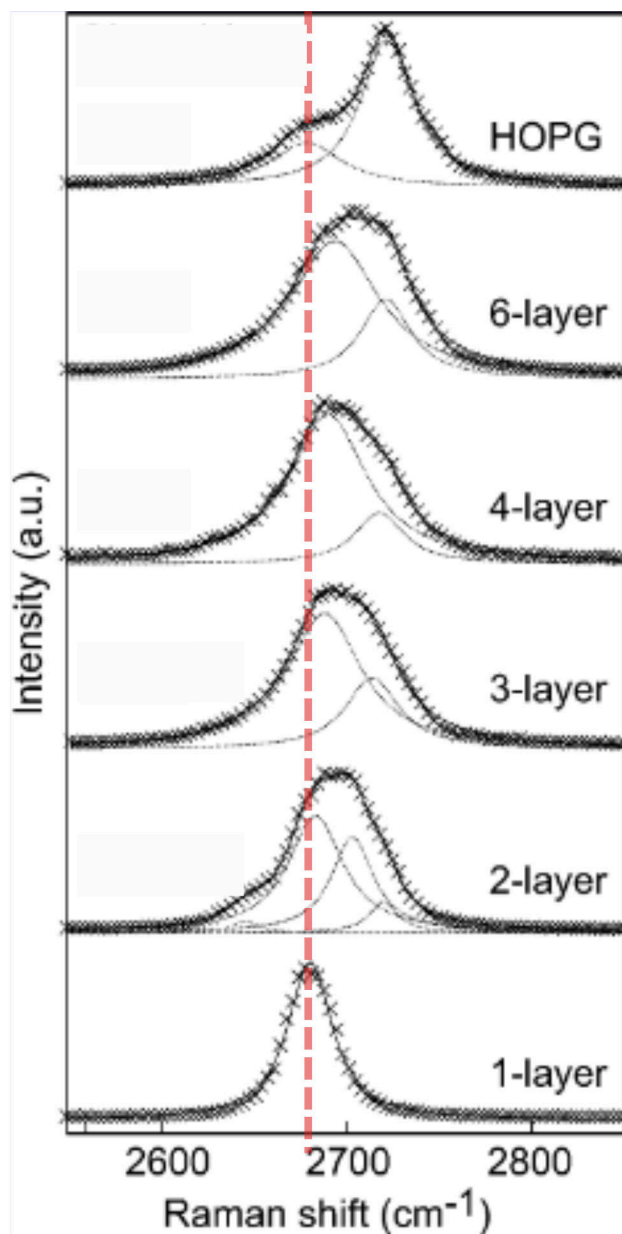
Figure 2.16: **2D width behavior for a different number of layers.** The dashed lines show the Lorentzian peaks are used to fit the data, while the solid lines are the result. Highly oriented pyrolytic graphite (HOPG) is shown as a reference. © Adapted from Graf D. et al. (2007)[62]

2.2.6 Carbon structures derived from Graphene

Fullerenes

Fullerenes are a large type of carbon allotropes that are considered to be very useful as inorganic and organic materials. They usually have hollow soccer-ball structures arranging different numbers of C- atoms, but they can also have ellipsoid or tube shapes[67]. Each C atom is linked to three near neighbors, with three of their four valence e^- forming a σ bonding. Many fullerenes have now been isolated, such as $C_7 0$, $C_7 6$, $C_8 2$, and $C_8 4$; however, $C_7 0$ and $C_6 0$ are the most accessible structures[68]. Among their properties, fullerenes possess a large specific surface area, high chemical stability, unique 3D structure, and good electrical conductivity[69]. Moreover, some of its applications are related to the areas of photocatalysts, including organic synthesis, the degradation of pollutants, antibacterial and disinfection in water, and hydrogen production[69].

Carbon Nanotubes

Carbon Nanotubes (CNTs) are sp_2 nanometric carbon materials composed of rolled-up graphene sheets[70] as seen in Fig 2.17 (a). As their name says, carbon nanotubes have a "tubular" appearance with a characteristic diameter of 4 nm approximately[71]. Furthermore, some ways exist to synthesize CNTs, going from arc discharge and vapor-grown carbon fibers to laser-abrasion and catalytic chemical vapor deposition (CCVD)[72], most used to obtain high-purity CNTs. Furthermore, these structures can be classified in three main groups, Figure 2.17, single-wall carbon nanotubes (SWCNTs), double-wall carbon nanotubes (DWCNTs), and multi-wall carbon nanotubes (MWCNTs), which is an important factor for the emergence of their properties.

Graphite

Graphite is a 3D material that constitutes the most common form of carbon occurring in nature. It is the result of the stacking of various parallel graphene layers, 3-coordinated sp_2 carbon, linked by Wan der-Waals interactions[73]. It is a mineral that occurs most abundantly in some igneous rocks, a variety of meteorites, and metamorphic rocks as a result of the dehydration of rich carbon sediments[73]. This form of carbon is characterized by softness and greasiness to the touch, followed by unique properties such as refractoriness, high heat and electrical conductivity, high thermal resistance, and readily soluble in iron[74].
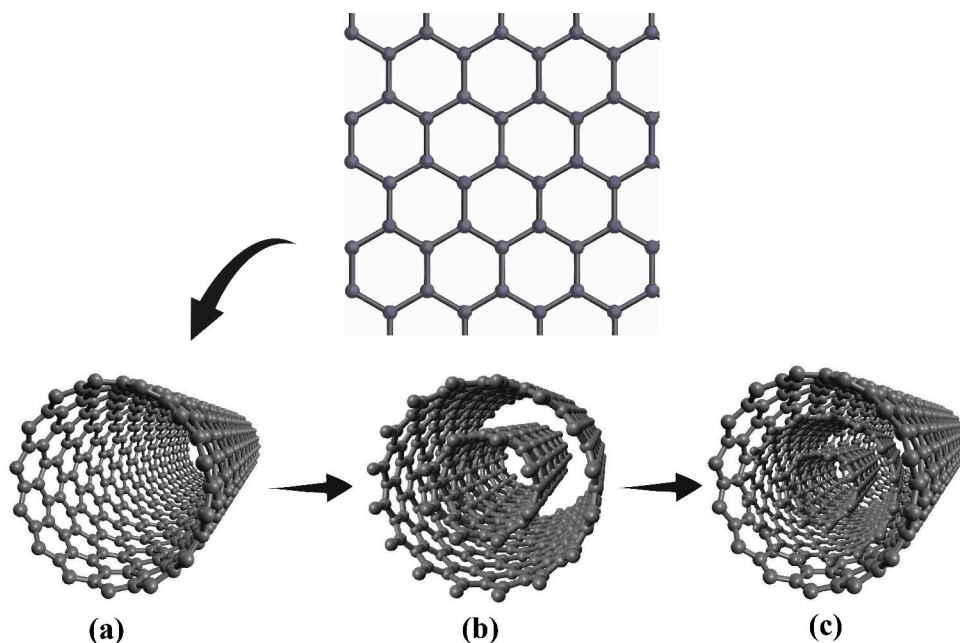
Figure 2.17: **CNTs formation and classification** (a) Graphene layer from which carbon nanotube is created after rolling (b) single-wall carbon nanotube (SWCNT) (c) double-wall carbon nanotube (DWCNT) (d) multi-wall carbon nanotube (MWCNT).

2.3 Silicon Carbide: the source for the formation of interstellar graphene

SiC has a refractory nature and a high ability to retain trace elements (e.g. Mg, Li, B, K, Al, V, Ca, Cr, Ti) in its crystal lattice, for this reason, it is the best studied presolar grain type[75]. It is commercially known as carborundum[73] and is classified within the group of carbides since carbon (C) is bonded to silicon (Si), an element with lower electronegativity (χ_C=2.55, χ_{Si}=1.90). It is also a wide-bandgap (2.3-3.3 eV)[76] semiconductor, which is used as a substrate for the heteroepitaxy of nitride materials and the synthesis of graphene via Si sublimation[77]. It can be found very rarely in nature, as well as in meteorites and diamonds[76].

2.3.1 Properties and synthesis methods of terrestrial SiC

SiC has outstanding characteristics such as erosion resistance, chemical and thermal stability, high hardness and strength, oxidation resistance, high melting point, and high erosion resistance, leading it to have

promising applications in high temperature and high power electronic devices, cutting and abrasion applications[78]. A synthesis method of SiC has been developed employing an electrochemical reaction using sand and carbon at temperatures until 2550 °C[76], through the called "Acheson process". This solid-state reaction has been improved over time using different components for its synthesis, such as petroleum coke[78] and salt[79]. The resultant product of this process is small platelets of 6H-SiC. However, due to the poor quality of this product, Tairov and Tsvetkov[80] developed a method to manufacture SiC ingots with large diameters through the "seeded sublimation method"[79].

2.3.2 SiC polytype classification

There exist a variety of SiC structures, each one characterized by its stacking arrangement, better known as polytypes, such as 3C- (often called β-SiC), 2H-, 4H-, 6H-(often called α-SiC), 8H-, 10H-, 14H-, 2OH-, 21H-, 9R-, 15R-, 19R-, and 24R-[78]. These polytypes correspond to the hexagonal (H), rhombohedral (R), and cubic (C) crystallographic categories. In general, the most common polytypes used and obtained easily from synthesis, are the 4H-SiC, 6H-SiC, and 3C-SiC, which differ from their electrical properties and band gap energies as detailed next.

3C-SiC (β - SiC) is a polytype with a low band-gap of $\sim$ 2.4 eV[78] compared to other polytypes with a characteristic zinc blende crystal structure. In this case, the number three (3C-) corresponds to the number of SiC layers needed for its periodicity, then in Figure 2.18 (a), a 3C-SiC structure can be described by the repeating sequence of ABC. This polytype can be synthesized at 1700 °C[78], but it is unstable at high temperatures >1900°C - 2000°C, which makes it difficult to grow[79].

The 4H-SiC polytype has a band gap of 3.26 eV[81], the largest one compared to 3C- and 6H- polytypes. It is favored to grow at very low temperatures of 2125°C[78] in contrast to 6H-SiC. Additionally, it is the most important SiC polytype for its use in electronics since it possesses the highest electric breakdown field of 2.3 MV/cm and a high carrier mobility[81]. This structure has an ABCB stacking order (see Figure 2.18) following its denomination as 4H polytype, since there are needed 4 SiC layers to achieve its periodicity. Otherwise, 6H-SiC (α - SiC) is a polytype with a band-gap of $\sim$ 3.02 eV[78] with a periodicity established every 6 layers, following a stacking order of ABCACB, as seen in Figure2.18(c). It has a characteristic wurtzite-like structure with an extremely great hardness of 9.5 and a density of 3.1-3.2 g/cm^3[82]. In general, it is often found as grains in rounded shapes and as crystal clasts.
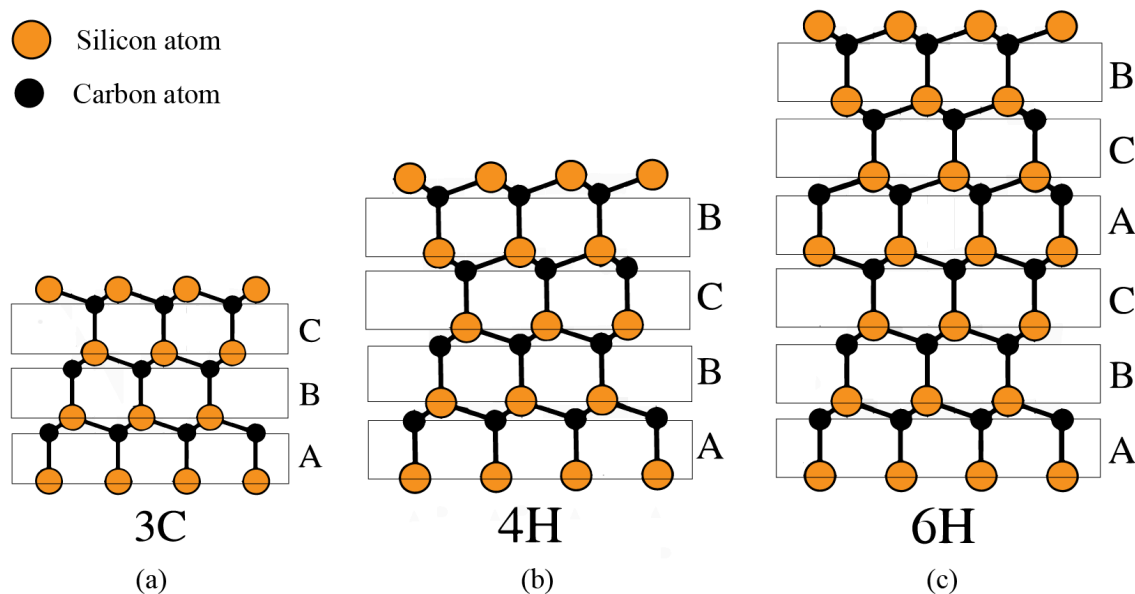
Figure 2.18: **Ball-stick model of 3C-SiC, 4H-SiC and 6H-SiC structures.** (a) 3C-SiC with an ABC-ABC stacking order. (b) 4H-SiC with an ABCB-ABCB stacking order. (c) 6H-SiC with an ABCACB-ABCACB stacking order. The rectangles correspond to a SiC layer designated with ABC letters.

The origin of α-SiC has been the center of attention for years because of the controversy behind the history of its provenance. This polytype was first documented in 1893 by Henri Moissan, who found SiC grains in the residues of the Canyon del Diablo meteorite in Arizona state, USA, consequently, in his honor, this mineral is often referred to as "Moissanite". Nevertheless, this theory was not widely accepted since it was associated with contamination during the treatment with artificial SiC (carborundum) from the cutting tools used to prepare the samples of the meteorite. Given this curious yet plausible fact, experiments on meteorites have been done, revealing residuals of SiC that have been definitively identified as of presolar origin[83]. After its first discovery, it also has been found in serpentinites, ophiolite complexes, meteorites, chromitites, and inclusions within diamond[73], giving it the property of heterogeneity for its possibility to grow in intrusive, basic, alkaline, acid, extrusive, sedimentary, ultrabasic and metamorphic conditions[82]. Considering the previous classifications related to its origin, SiC can be considered as part of the minerals from the Earth's deep mantle that have reached the surface.

2.3.3 Characterization methods

Raman Spectroscopy

One of the most powerful methods of characterization for recognizing the polytype of a material is Raman Spectroscopy, due to the detailed information that the phonons of a material can give. The principal branches of phonon dispersion consist of LA (longitudinal acoustic), TA (transverse acoustic), LO (Longitudinal optical), and TO (transverse optical) modes. The branches or phonon modes are the sinusoidal patterns (standing waves) of the motion of phonons, which highly depend on the type of vibration (i.e. optical, longitudinal, acoustic). The unit cell of a νH polytype ($\nu = 2, 4, 6...$) along the z-axis is ν times larger than the accepted bilayer SiC length (unit length)[79]. In other words, for the case of 4H- and 6H- their unit cell is 4 times and 6 times larger than that of 3C-SiC respectively, and their Brillouin zone is one-fourth and one-sixth of that of 3C-SiC. Therefore, the dispersion curves of such polytypes can be approximated by folding their principal LA, TA, LO, and TO modes, creating new intersections at Γ point as shown in Figure 2.19. From this fact, new phonon modes or "folded modes" are created.

In Figure 2.20, the Raman spectra for 3C-, 4H-, and 6H- polytypes are seen. For the case of 3C-SiC, TO and LO phonon modes scatter light at 796 cm^{-1} and 972 cm^{-1} respectively. Otherwise in 4H-SiC, TO and LO phonon modes scatter light at 796 cm^{-1}, 776 cm^{-1} and 964 cm^{-1}, 838 cm^{-1}, respectively. In the following Table 2.3.3 by Nakashima S. and Harima H.[84], a summary of the corresponding Raman frequency (cm^{-1}) for each phonon mode is shown.

Polytype	Phonon Modes (cm^{-1})			
	FTA	FTO	FLA	FLO
3C-SiC		796		972
4H-SiC	196, 204, 266	796, 776	610	964, 838
6H-SiC	145, 150, 236, 241	797, 789, 767	504, 514	965, 889

Table 2.2: Raman frequency of 3C-, 4H- and 6H- polytypes for its corresponding phonon modes
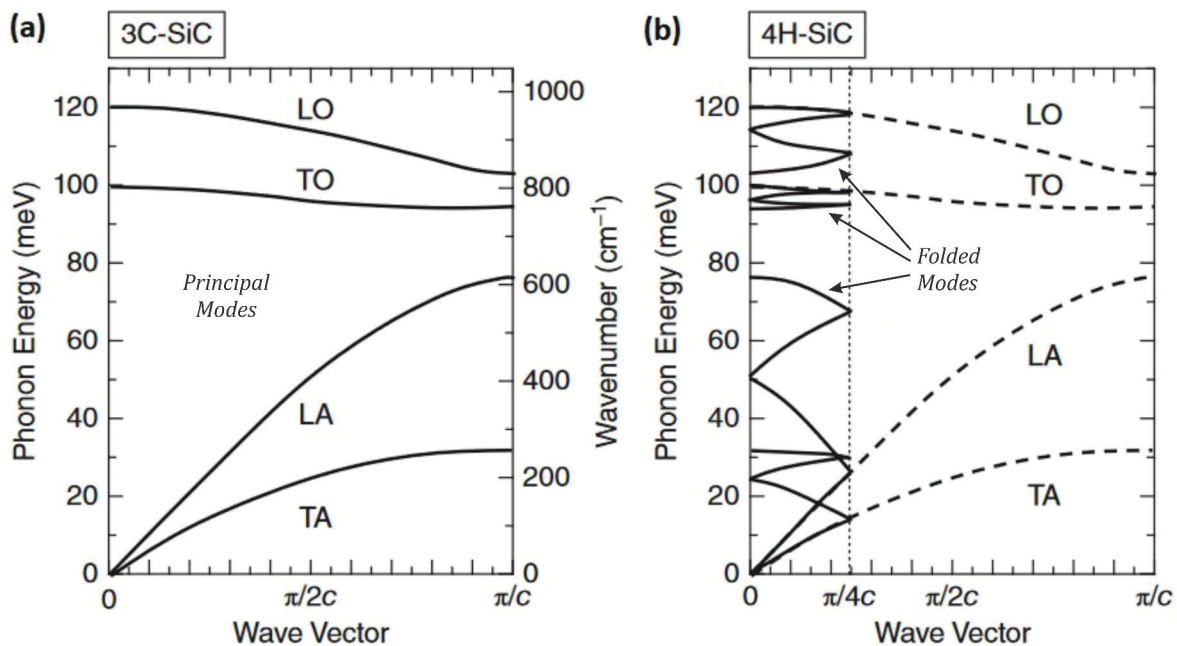
Figure 2.19: **Phonon dispersion of 3C-SiC and 4H-SiC polytypes.** (a) Principal phonon modes seen in the cubic structure of SiC. (b) In 4H-SiC, new phonon modes are created at the Γ point. © Adapted from Kimoto T. and Cooper J.
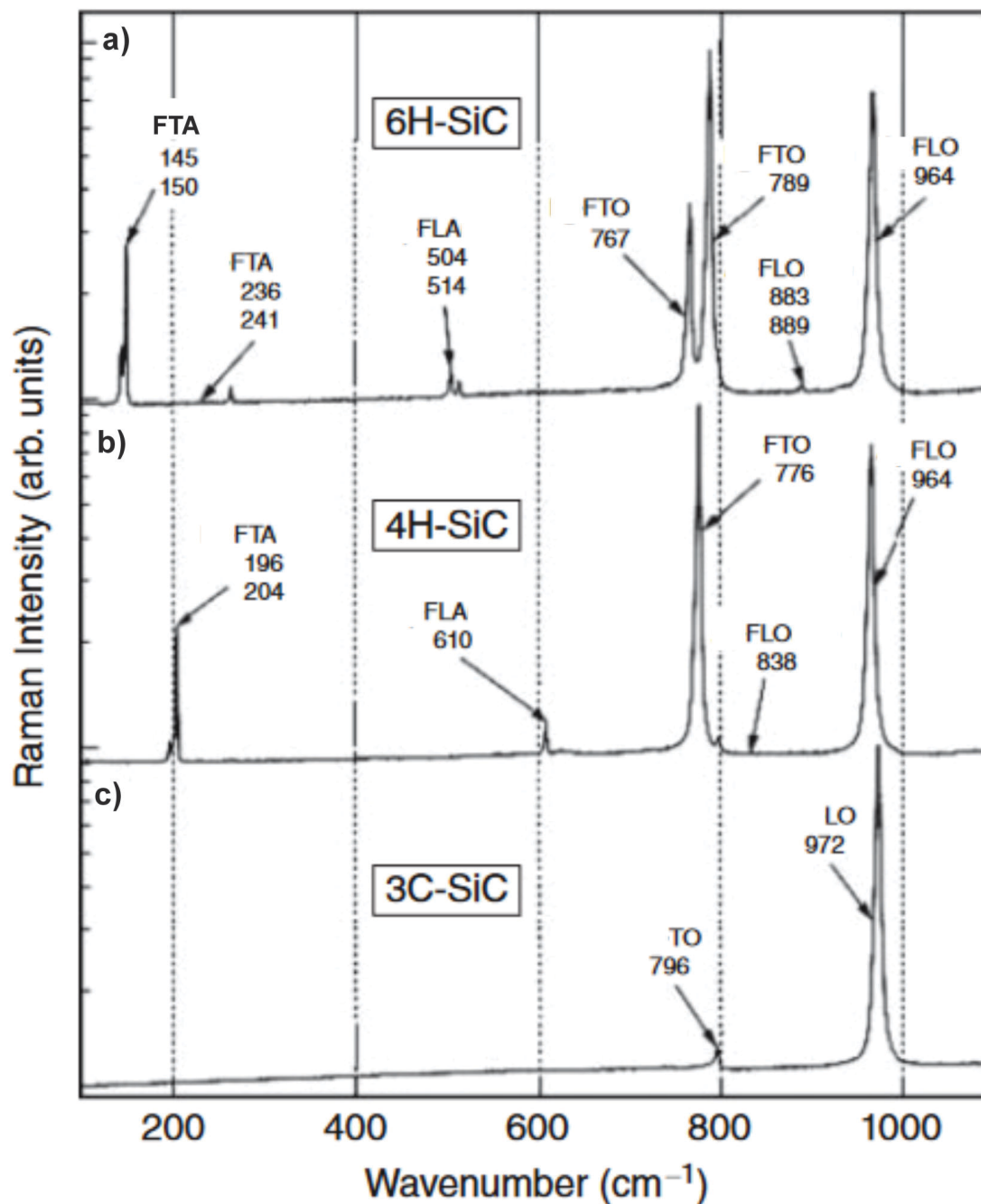
Figure 2.20: **Raman Spectra of 3C-, 4H- and 6H- SiC polytypes.** (a) 6H-SiC, (b) 4H-SiC, and (c) 3C-SiC raman frequencies. FTA and FLA modes appear at low Raman frequencies around 140-630 cm^{-1}. FTO and FLO modes appear at high Raman frequencies around 760-970 cm^{-1}. © Adapted from Kimoto T. and Cooper J.[79]

X-Ray Diffraction

X-ray diffraction (XRD) is a non-destructive technique of characterization for crystalline materials which provides information about phases, structures, crystal orientations (texture), average grain size, crystallinity, and crystal defects[85]. The resultant diffraction pattern is a fingerprint produced by constructive interference of a monochromatic beam of X-rays over the periodic atomic arrangement of any material[85]. This interference is produced when satisfying Bragg's law from eq. 2.14:

$$n\lambda = 2d\,Sin\theta \tag{2.14}$$

where λ is the wavelength of the X-rays, n is an integer, θ is the diffraction angle generated, and d is the interplanar spacing which produces the diffraction[85]. This law relates the wavelength (λ) of X-rays to the lattice spacing d and the diffraction angle θ in a crystalline sample. The whole process consists of the X-ray laser beam being scattered at determined angles by the atoms of the material, which pattern is a Fourier-transformed image of its crystal structure in reciprocal space[86]. This can be seen in Figure 2.21.

In general, an X-ray diffractometer is built with three basic elements:

- A cathode ray tube where X-rays are generated from the heating of a filament to produce e^-, which are highly accelerated towards the target sample.

- An X-ray detector that receives the information from the scattered X-ray beam, processes it, and converts the signal to counts.

- Sample holder where the sample of interest is bombarded for measurements.

Two geometries of X-ray diffractometers can be mentioned: the source-detector and the rocking curve. The source-detector geometry, Figure2.23(a), makes the X-Ray tube rotate at a θ angle, as well as the detector, which moves at a 2θ angle, while the sample holder is fixed to be bombarded by X-Rays. The rocking curve geometry, see Figure2.23(b) makes the sample rotate following the incident X-ray beam at a θ angle, while the detector is fixed to collect the diffracted X-rays. The most used source of X-rays for single crystal radiation is CuKα radiation, which corresponds to λ= 1.5418 Å[85].

Additionally, the diffraction patterns produced by X-rays can help to determine the Miller indices of a specific material based on the preferential orientation rule[87]. Then, they specify the orientation of planes in space. A crystallographic plane of a material is defined by three nodes in a 3D space lattice, each one expressed as the Miller indices ($h\,k\,l$), in curvilinear brackets ( ). Each index corresponds to the interception between one crystal facet and one coordinate axis in a unit cell, a/h, b/k c/l, where a, b, and c are the lattice constants of the unit cell[87]. This is represented in Figure 2.22 (a) and (b). The crystallographic planes
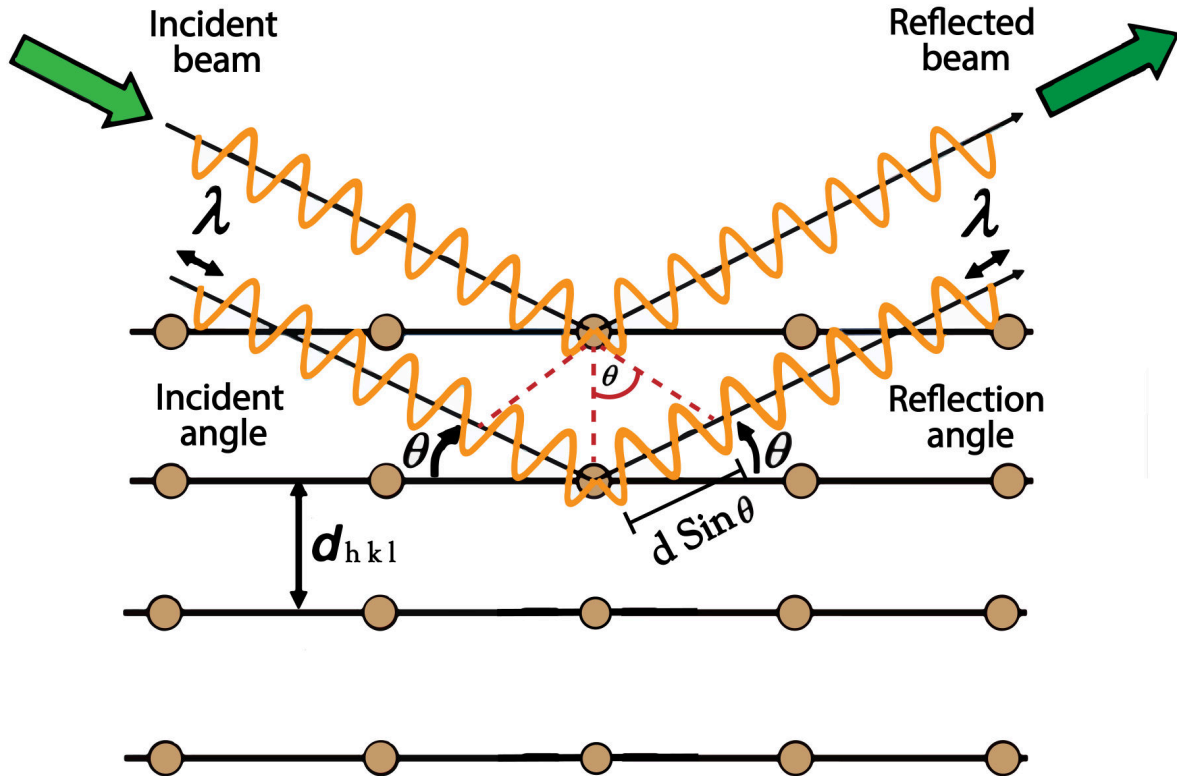
Figure 2.21: **Scheme of XRD working principle.** The incident beam of wavelength λ is scattered at different angles θ by the atoms in the lattice. A constructive interference is created when 2d Sinθ.

are equivalent to each other by symmetry if the interplanar spacing ($d_h kl$) is the same[88]. As a result, there exists a one-to-one between interplanar spacing ($d_h kl$) and each crystallographic plane ($h\,k\,l$), which can be evidenced analytically as follows[88]:

$$d_{hkl} = \frac{a}{\sqrt{h^2 + l^2 + k^2}} \tag{2.15}$$

where a is the lattice constant. This equation is given to determine the interplanar spacing of a cubic lattice. Nevertheless, there are different equations for each cell type (i.e. tetragonal, hexagonal, orthorhombic). In summary, there exists a specific plane ($h\,k\,l$) for a particular incident x-ray wavelength and cell type (of lattice constant a) at which diffraction can occur.
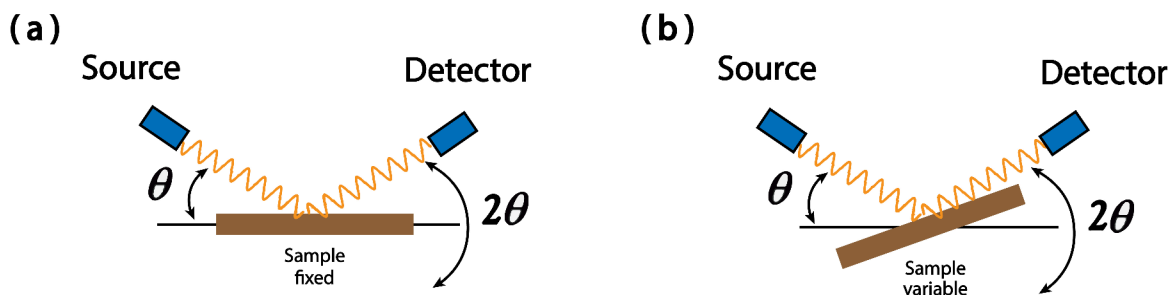
Figure 2.22: **Geometries of XRD diffractometers** (a) The X-Ray tube rotates at a θ angle, as well as the detector, which moves at a 2θ angle, while the sample holder is fixed. (b) The sample rotates following the incident X-ray beam at a θ angle, while the detector is fixed at $2\,\theta$ to collect the diffracted X-rays.
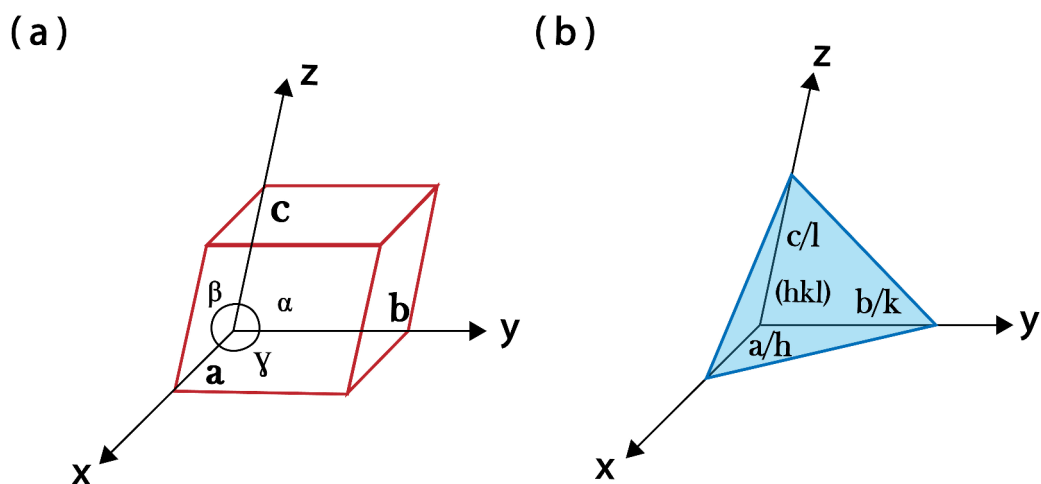
Figure 2.23: **Representation of Miller indices and planes** (a) Interception between one crystal facet and one coordinate axis in a unit cell, represented as a/h, b/k c/l. (b) Crystallographic plane (*h k l*) of a material expressed with the Miller indices: h, k, l

XRD in SiC is the best tool used for identifying its variety of polytypes, in which diffractograms change depending on the in-plane arrangement of atoms. In Figure 2.24 (a) and (b), the XRD diffraction patterns of the most abundant SiC polytypes, α-SiC, and β−SiC, are shown with their respective planes. As can be

seen in Table 2.3, α-SiC has around 9 diffraction angles derived from its hexagonal structure, while β-SiC scattered angles are seen at 4 representative peaks[89]. It is important to mention that some of the XRD peaks seen in Table 2.3, are not seen in Figure 2.24 (a) since it was synthesized at a different temperature and using another method than the one used for α-SiC. Furthermore, depending on the method by which these polytypes are produced, the samples can have small amounts of other SiC polytypes in their structure, as is the case of its production via the sublimation method[90]. Additionally, graphite and other impurities causing stacking faults can be detected.
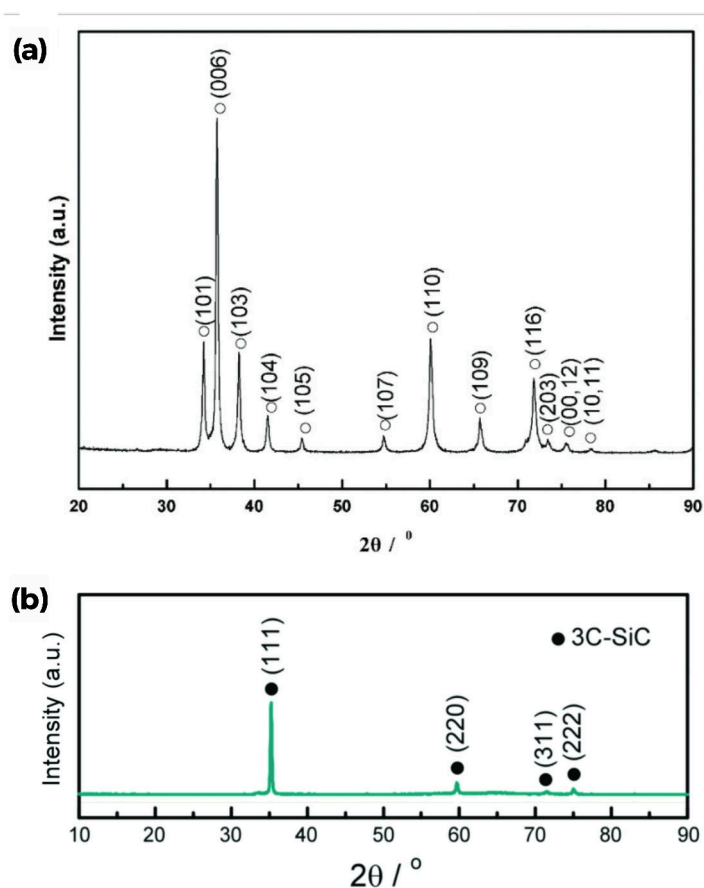
Figure 2.24: **X-Ray diffraction patterns of α-SiC and β-SiC**. (a) α-SiC diffraction pattern with peaks around 34°, 36°, 38°, 42°, 46°, 55°, 61°, 66°, 72° and 74°. (b) β-SiC diffraction pattern with characteristic peaks and planes around 35°, 60°, 72° and 75°. © Adapted from Yang (2021)[91] and Zhigang Y. et al. (2019)[92].

Polytype	2θ
α-SiC	25.92°, 27.25°, 35.35°, 45.56°
	49.36, 56.48°, 59.72°, 62.60°, 71.56°
β-SiC	35.35°, 59.72°, 71.56°, 75°

Table 2.3: 2θ diffraction angles for α and β SiC

2.3.4   Sources and evidence of SiC formation in space

Approximately, 10.000 SiC presolar grains have been analyzed for their isotope compositions of different elements[75]. As mentioned previously in Section 2.3.2, "moissanite" has a presolar origin since it has been detected in some carbonaceous chondrites and has been shown via IR that it is very common in the covering of carbon-rich AGB stars[73], even more, because of the presence of noble gasses within their grains, such as Xe, Ne[93], and Kr[94]. The very first studies of the isotopic and chemical composition of meteorites have given important information about the presence of SiC in their structure. The most analyzed chondrites are Murray and particularly Murchison[94]. In this last one, it was found that SiC grains range from < 0.2 μ m to 6 μ m[95]. Also, it was seen that they have cubic 2.25 (a) and hexagonal, 2.25 (d), shapes; however, their lattice structures mostly correspond to cubic (β-SiC) according to their Raman spectra[96]. In general, only two polytypes of interstellar origin are present, the hexagonal 2H (α-SiC) which corresponds to the ~ 2.7% of all studied grains, and the cubic 3C (β-SiC) polytype with a corresponding ~ 79.4%[93]. The remaining population corresponds to 2H/3C intergrowths (17.08%), disordered SiC (% 0.89) and other polytypes < 0.20 %[93]. Also, some of the SiC analyzed have subhedral shapes, as seen in Figure 2.25 (c), while most of them are roughly and platy equant, as seen in Figure 2.25 (b), with fractured surfaces[95]. However, other SiC grains have shown euhedral shapes as a result of poorly interstellar processing before reaching Earth[15].

The anomalous noble gas components, Ne-E(H) and Xe-s, allowed the discovery of presolar SiC in which all Xe-s isotopes show enrichment of ^{132}Xe, ^{130}Xe and ^{128}Xe isotopes and depletion of ^{129}Xe and ^{131}Xe isotopes[16]. In this case, SiC is supposed to have been formed through the slow neutron capture process in AGB or RGB stars, while Ne-E(H) is estimated to be produced at high temperatures of ~ 1500 K[16].
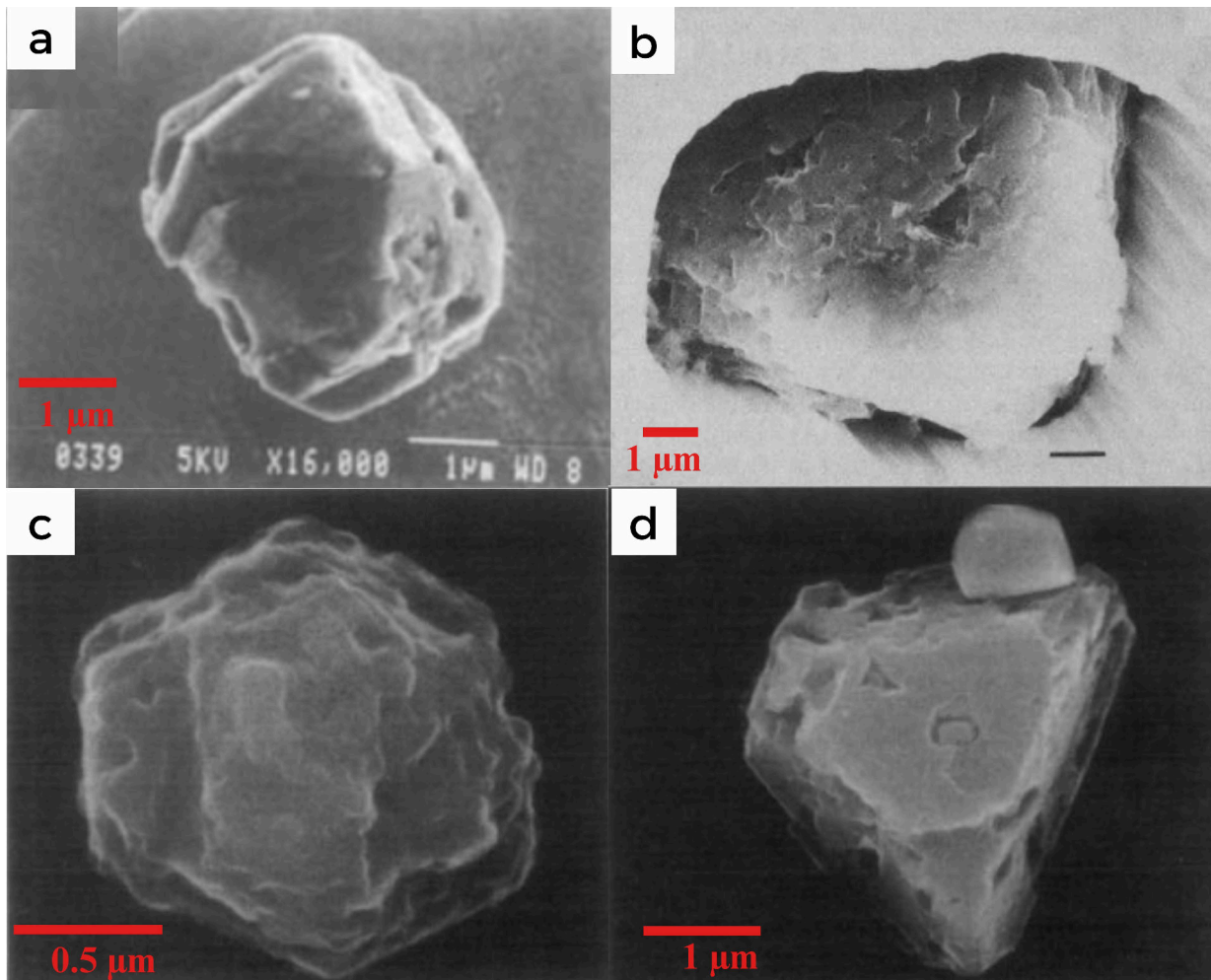
Figure 2.25: **SEM images of SiC grains from Murchison meteorite.** Micrographies of SiC grains with (a) cubic, (b) platy surface texture, (c) subhedral, and (d) hexagonal shapes. © Adapted from Amari S. et al. (1994)[95], Anders E. et al.(1993)[94] and Virag A. et al. (1992)[96].

2.4 Existence of carbon allotropes in space

The existence of carbonaceous molecules in space is a common topic in astrochemistry. Moreover, important questions arise when referring to its abundance and at what time of the universe's evolution they formed. Approximately the 80% of the total carbon in the universe has been incorporated into gaseous polycyclic aromatic hydrocarbon (PAHs)[97], as well as into Carbon Monoxide (CO), which is the second most abundant molecule in the gas phase existing in the ISM[98] (after H_2). Interstellar dust experiences many chemical and physical processes over time that can modify the composition of the molecules forming it. Among these molecules, a variety of carbon allotropes exist that participate in the building of the dusty interstellar medium, such as nano-diamonds, fullerenes, amorphous carbon, and graphite, among others[99]. This section will detail some of the extraterrestrial sources of carbonaceous molecules and the optimal conditions required for their formation in outer space.

2.4.1 Extraterrestrial sources of carbon

Nowadays, the dust composition of the interstellar medium, specifically carbon (C), is justified by direct observations and modeling, thus reaching various conclusions about the stages of nuclei formation. The most abundant elements within the universe, helium (He) and hydrogen (H), were formed in a short period after the Big Bang, during a process called *primordial nucleosynthesis*[100]. Meanwhile, heavier elements such as carbon (C), oxygen (O), silicon (Si), calcium (Ca), and iron (Fe), among others[101], were formed inside of stars through a process called *stellar nucleosynthesis*[100].

In general, carbon has two main stellar sources: mass loss from evolved stars and supernova explosions[102], as a consequence of the chemical reactions produced by high pressures and temperatures. The main process of C production is called *triple-alpha process* (3α)[103], one of the fundamental reactions in astrophysics, which occurs when two α-particles (^4He nuclei) resultant from the interior of stars fuse into beryllium (^8Be), as seen in eq. (2.16). Even though ^8Be has a short lifetime of 10^{-16} s, it has enough time to interact with a third α-particle to produce carbon (^{12}C), as shown in eq.(2.17).

$$^4He + {}^4He \rightarrow {}^8Be \tag{2.16}$$

$$^4He + {}^8Be \rightarrow {}^{12}C \tag{2.17}$$

This process occurs in the layered interior structure of very massive stars as they explode to become Type II supernovae[102]. Moreover, it is also carried out at the final evolution stage of low-to intermediate-

mass stars ($M_* \sim$ 1–8 $M_\odot$) during nuclear burning when they turn into Asymptotic Giant Branch (AGB) stars[104].

Carbon-rich AGB stars

AGB stars are the final phase of low-to intermediate-mass stars. Their evolution is very mass-dependent, distinguishing a classification as low-mass, intermediate, and massive (super) AGB stars[104]. Most massive intermediate-mass stars become super AGB stars. Only a fraction of the stars at the AGB phase (1.1–4 $M_\odot$)[105] become carbon-rich after a long process of various Hydrogen (H) and Helium (He) burning, and the ignition of star material (dredge-up). These stars go out from the main sequence stage when they have consumed all the hydrogen (H-burning) within their core to convert it into He.

When the hydrogen is totally spent, the stellar core starts to suffer a gravitational contraction, which causes H to start burning in a shell around the He core[102]. As the core continues to contract, the star's envelope expands and cools, giving way to the creation of a red giant star (RGB), followed by the ignition of the He core (He-burning). At this point occurs the first dredge-up[104], where the material processed in the core, such as ^{12}C and ^{13}C, is ejected via mass loss to the ISM. A second dredge-up is produced after the end of He supply, where more carbon ^{13}C is ejected. Later, the star will consist of a carbon and oxygen (C/O) core surrounded by H- and He-burning shells, giving way to the creation of an asymptotic giant branch (AGB) star[102]. During this phase, the 3α process produces more ^{12}C in the remaining He-burning shell. The third and final dredge-up is carried out where a great amount of ^{12}C is ejected to the star surface, leading to the formation of a *carbon-rich AGB star*, with a carbon-to-oxygen ratio of C/O > 1[106], also known as N-type stars for intrinsic carbon stars[17]. The complete evolution phase of AGB carbon-rich stars is seen in Figure 2.26.

The most of C-stars should have a mass between 1.5-2.5 $M_\odot$, while some of them exceed 3–4 $M_\odot$[17]. The mass ejected from these stars creates a circumstellar envelope (CSE) consisting of submicrometer-sized grain particles and gas-phase molecules[106] due to the difference in temperature and pressure close to the star. At the very near photosphere of high mass losing AGB stars, the inner shell of CSE can reach temperatures up to[106] $\sim$ 2000–4500 K with densities of $\sim 6 \times 10^{15}$ cm^{-3}, since the material has been recently ejected to the star surface. McCarthy[107] et al. (2019) states that the CSE can also reach temperatures up to $\sim$ 1000-2500 K and densities of about 10^8 - 10^{14} cm^{-3} inside the five stellar radius of the star (r $\leq 5R_*$). As the material in the CSE still flowing out, its temperature can descend up to $\sim$ 25 K[102], while its density can drop until $\sim 10^4$ cm^{-3}.
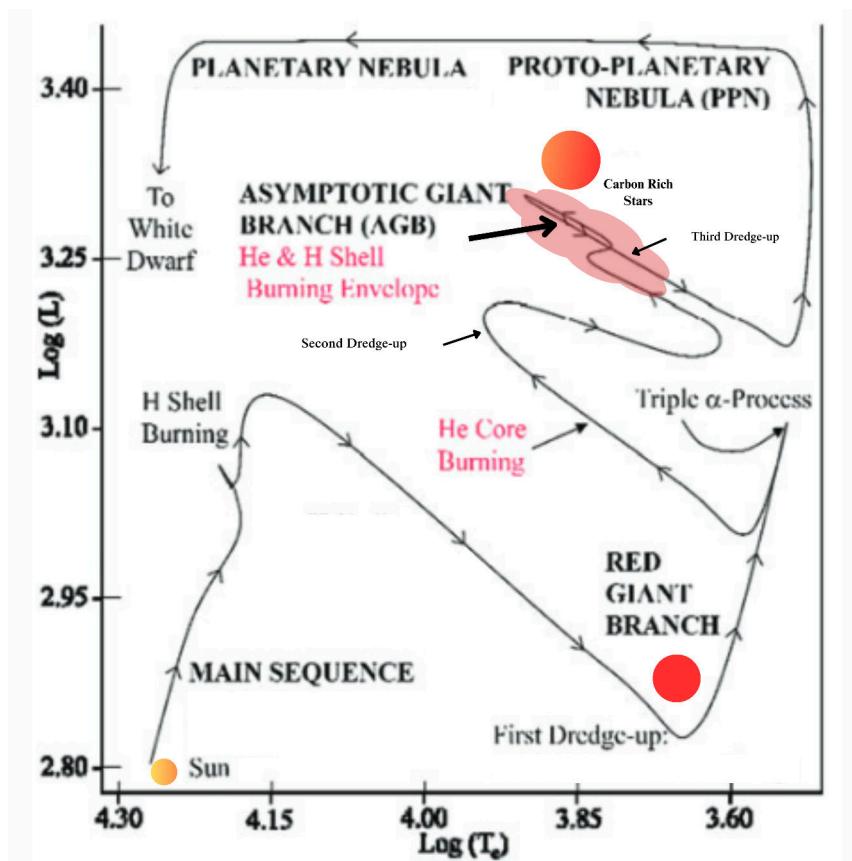
Figure 2.26: **Hertzsprung-Russel (H-R) diagram of AGB carbon-rich stars and PN stage evolution.** © Adapted from Ziurys, L. M. et al[102].

Planetary Nebulae (PNe)

Following the evolution of a carbon-rich AGB star, when its mass loss increases it promotes the post-AGB evolution at higher temperatures[108] to finally constitute the central star of a planetary nebulae (PNe)[104]. PNe are produced with different dust and molecular composition, then in the molecular zone, the abundant carbon monoxide (CO) encapsulates the less abundant element from both[109]. For abundances C/O >1, it leaves free carbon (C) to drive the chemistry and formation of amorphous carbon, polycyclic aromatic hydrocarbons (PAHs), fullerenes, and SiC[109].

2.4.2 Optimal conditions for carbon allotropes formation in space

When the stellar wind flows out of stars, it reaches pressures as high as 10^{-5}-10^{-3} Pa and low temperatures of about 2500-1000 K[99]. These conditions allow molecules and atoms to nucleate as small dust seeds. For the case of the CSE of carbon-rich AGB stars, the dust cools to about 1000-1200 K[106]. Therefore, the resultant dust seeds are highly composed of SiO, CS, SiS, C_2H_2, CH_4, C_2H_4, C_4H_2, HNC, and SiC[107], where carbonaceous grains and silicates represent a higher amount. These small grains leave the nucleation stage to enter the growth stage, where they interact with UV photons and cosmic rays, letting them participate in the creation of more complex carbon-based molecules, most of them acetylenic chain–type, such as[107] HC_5N, C_6H, SiC_4, SiH_4, among some carbonaceous allotropes such as fullerenes, polycyclic aromatic hydrocarbons (PAH's), nanodiamonds, graphite, and amorphous carbon[102]. The majority of pathways for the synthesis of carbon allotropes are given from molecular dynamics (MD)[110, 111] and laboratory experiments[112], which will be detailed next.

Graphite

Several studies show that carbon grains formed at around 1000 K have a very high sp^2 character with a very low content of H atoms[113]. The environment producing this carbon structure is at carbon-rich AGB stars ejection stardust, where carbon grains are composed of large stacked graphene sheets (graphite) up to 3 nm[113], but also and more likely from Type II supernova ejecta[15]. From the existence of cauliflower-type and onion-type graphite detected in the Murchinson meteorite, it was speculated that they could have formed in environments at high supersaturation levels of C (1 < C/O < 1.2) and low quantities of other molecules to allow C condensation[114].

Amorphous carbon

Most amorphous carbon had been detected in a hydrogenated form (HAC), as a result of the H incorporation via photo-processing occurring in HII regions[115]. These HACs can also be formed at the outer regions of CSE of AGB stars, at temperatures around 80-100 K, where the remaining carbon grains are processed by thermal H atoms and UV photons via shock waves, allowing the creation of a thin surface layer of a HAC material[113], as shown in Fig 2.27(b). However, after the formation of HACs, these structures can suffer a dehydrogenation process due to suffering heating at low temperatures (~ 800 K) via UV-photolysis, resulting in the growth of graphitic islands of low density identified as amorphous carbon (aC)[116]. Moreover, aC can also occur at the inner shell of CSE of more evolved AGB carbon-rich stars[102], where high mass ejection occurs.
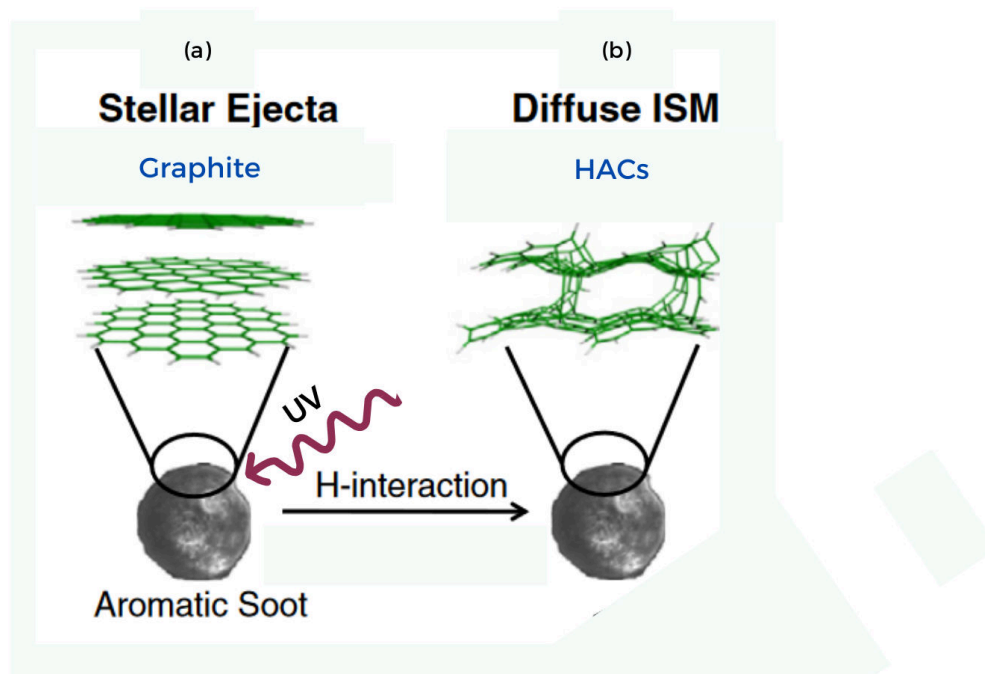
Figure 2.27: **Evolution of hydrocarbon dust in the ISM** from the formation of graphite to HACs ©
Adapted from Chiar J. E. et al.[113].

Nanodiamonds

Stellar nanodiamonds contain many C atoms and are mostly observed around young stars[117]. Their
origin is still controversial, talking about whether their formation was inside or outside the solar system.
Nevertheless, they are cataloged as presolar structures because of the noble gases they contain, such as
helium (He), neon (Ne), argon (Ar), xenon (Xe), as well as krypton (Kr)[118], from which Xe is related to
be formed at supernovae, thus constituting a strong evidence of a presolar origin[16]. About its formation,
some mechanisms have been proposed by different authors, including high-velocity collisions (shock
waves) that generate pressure waves within graphitic grains, formation by low-pressure condensation in
expanding gas envelopes[118] and irradiation-induced transformation of carbonaceous grains produced by
energetic ions[16]. After a further experimental evaluation of these mechanisms compared with Allende and
Murchison nanodiamonds structure, they found that star twin microstructures seen in these meteorites are
also seen in a large abundance in CVD nanodiamonds[16], see Figure 2.28 then the predominant mechanism

for meteoritic nanodiamond formation is the one of vapor condensation highly occurring in expanding Type II supernova gas[119] at temperatures around 1200–4000 K and pressures of 40–400 kbar[120].
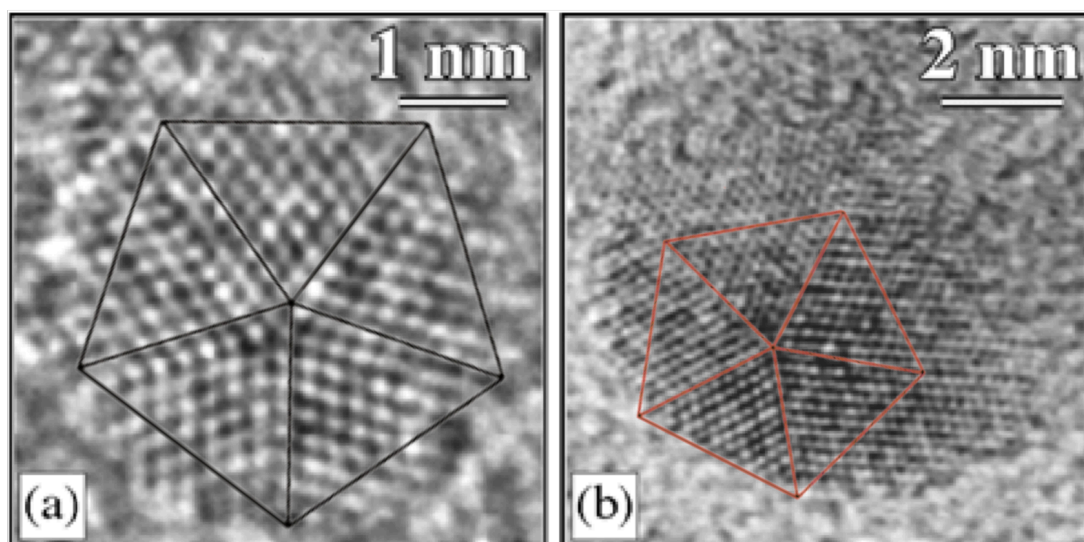
Figure 2.28: **Decahedra multiply-twinned particle (MTP) structure** in a) Allende meteorite and b) CVD-synthesized nanodiamonds seen in black and red decahedra © Adapted from Daulton T. L.[16].

Graphene

As the material resulting from the interior of the star still flowing, a series of significant processes are carried out in the inner and outer shells of the CSE. In a model presented by Merino[121] et. al. (2014), they conclude that the SiC grains present at CSE end with a graphene cover, as seen in Figure 2.29. They show that SiC grains are nucleated in the inner regions (1-5 R_*) of C-Rich Red Giant stars. Then, the remaining high temperatures ($\sim$ 1500 K), induce its Si sublimation and C segregation, for this reason, SiC grains always possess a graphitized surface (e.g. Monolayer and bilayer graphene). Also, as these grains still travel outwards, they reach cool temperatures of 1500–1000 K, where they are exposed to ultraviolet photodissociated atomic H, which leads to the formation of hydrogenated carbon derivatives (e.g. functionalized graphene). Later on, at T $\sim$ 1000 K, a thermal desorption of Polycyclic Aromatic Hydrocarbons (PAHs) is carried out around (5-20 R_*). Finally, when the material reaches the cold external layers of the envelope (circumstellar shell), at about 100 K, the incoming cosmic rays and UV photons from

the interstellar medium (ISM) process it to produce SiC_4, C_6H, C_5, MgCN, SiC_4, among other compounds.
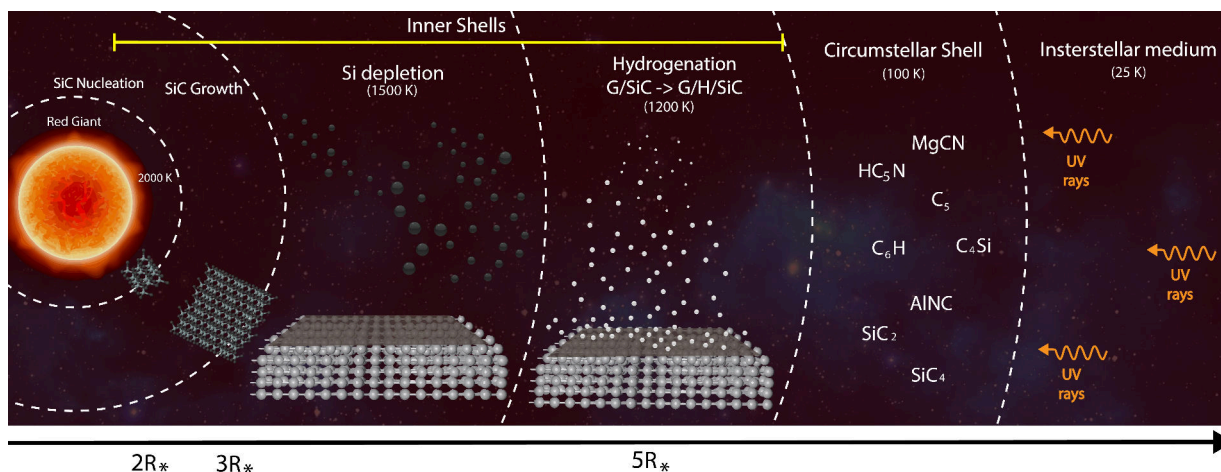
Figure 2.29: **Sketch of the evolution of SiC grains.** SiC grains nucleation occurs within the first 2 R_* at T= 2000 K. At this point the SiC grains condensate from the gas phase into μm- and nm-sized particles. Then, SiC is heated to T $\sim$ 1500 K due to the star radiation, causing Si depletion and the formation of C-rich structures (e.g. Graphene). Then, the graphitic surface is exposed to atomic hydrogen at T$\sim$ 1200 K. As the particles still flowing out, the temperature decreases (T $\sim$ 100 K) and incoming cosmic rays and UV photons from the interstellar medium (ISM) processes these particles to produce SiC_4, C_6H, C_5, MgCN, SiC_4, among others

2.4.3   Evidence of extraterrestrial carbon allotropes formation

A lot of carbon-rich material with an interstellar origin remains pristine encapsulated in many ways in comets, interplanetary dust particles and meteorites, which later is delivered to Earth[102]. Several studies over ancient meteorites have been done to analyze their chemical composition, searching for clues about the very first steps of the universe's formation. Among all the evidence, there have been found amorphous carbon[122], graphite whiskers[123], nanodiamonds[124], etc.

Amorphous carbon emission is difficult to observe since it is only seen close to stellar ejects through featureless blackbody-like continuum emission[99]. However, an experimental analysis done in the Murchinson (CM2) meteorite has shown the existence of amorphous carbon from SEM and TEM images, see Figure2.30 (a) and Figure 2.30 (b), of carbonaceous B4a-X-1 grains and a Raman spectra with overlapping and very

broad peak widths of G and D bands in B4a-W-1 and B4b-7-1 grains, see Figure2.30(c), which matches with the presence of amorphous highly disordered carbon[122]. Moreover, high amounts of nanodiamonds have been found in meteorites such as Allende, Murchinson[16], and ureilites DaG 868 and Dho 3013[124]. In both ureilites, carbon is commonly present in long-shaped and vein-like granulate graphite areas in which micrometer-sized diamonds (1-10 μ m) are present in SEM, Figure 2.31 (a), and cathodoluminescence analysis (CL), Figure 2.31 (b), in DaG 868 ureilite.
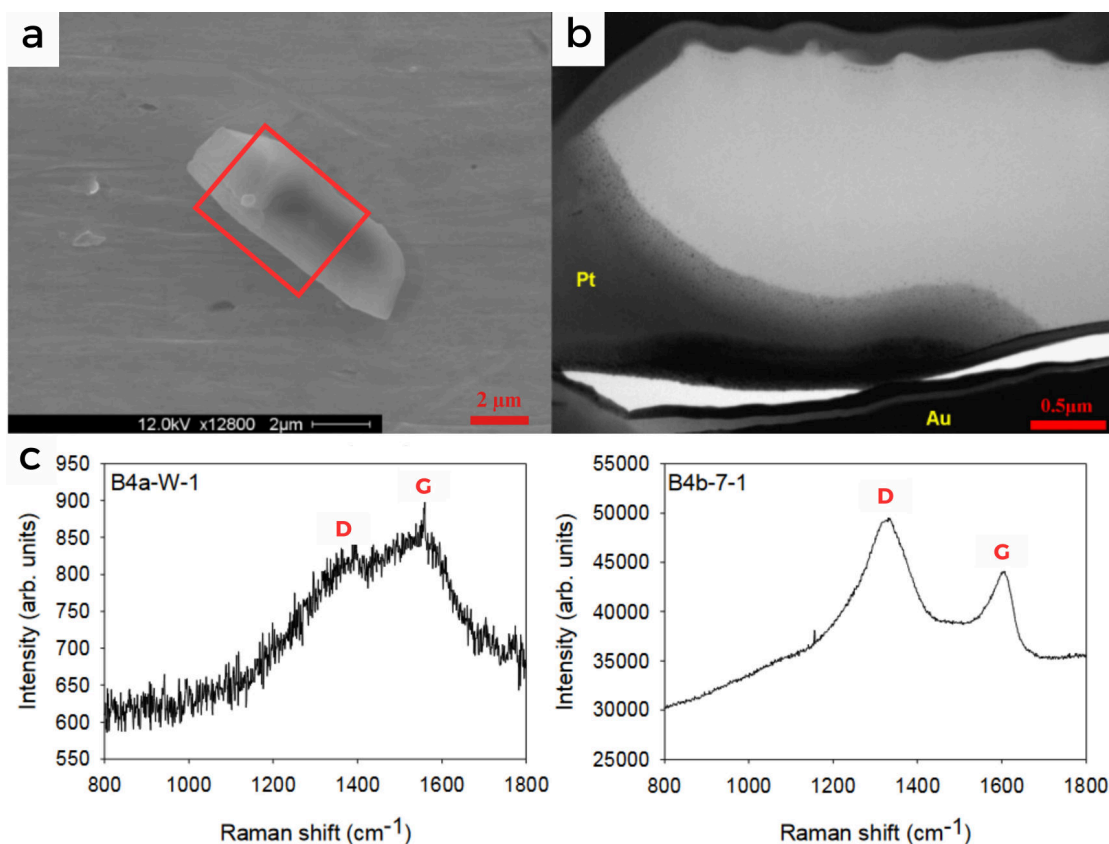
Figure 2.30: **SEM, TEM, and Raman spectra images from Murchinson (CM2) meteorite.** (a) SEM image of carbonaceous grain B4a-X-1 and (b) TEM image of the same grain confirming its amorphous nature. (c) Raman spectra of amorphous B4a-W-1 grain sample showing an overlapping of D and G bands, and more ordered B4b grain sample. © Adapted from King et al. (2011)[10].

For the case of graphite, it has been discovered graphite whiskers (GWs)[123] are associated with high-temperature components within CV3-type carbonaceous meteorites. These components are referred to as
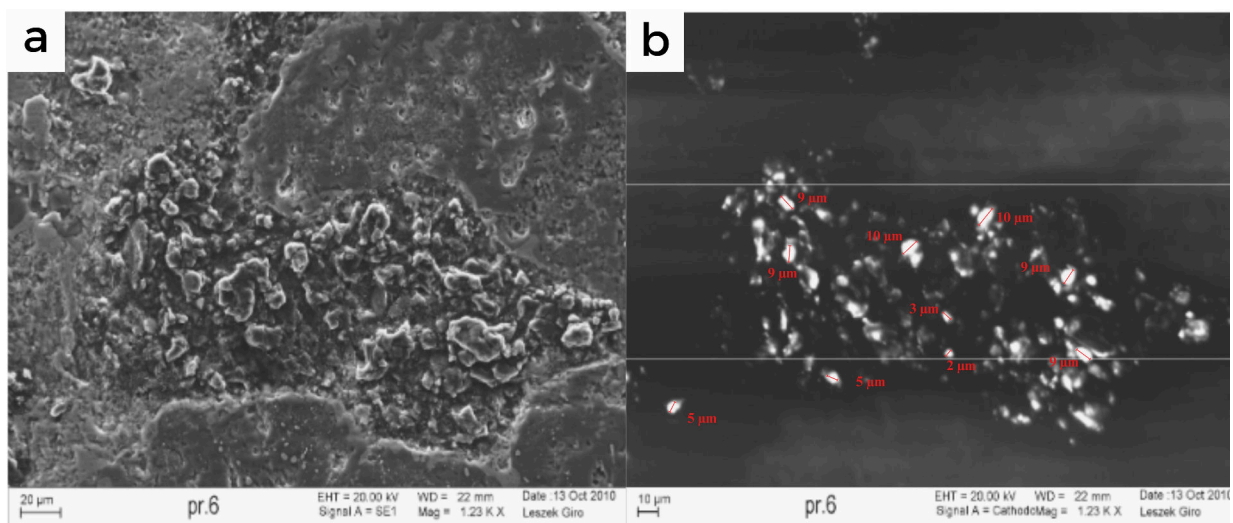
Figure 2.31: **SEM and CL images from DaG 868 ureilite meteorite.** Diamonds of 1-10 μm size are seen in (a) SEM image of a vein-like carbon area and (b) CL image of the same area as (a) where diamonds are highlighted in bright spots. ©Adapted from Karczemska (2010)[124].

chondrules and CAIs, whose temperature formation is > 1200 K and ~ 2200 K[125] respectively. GWs were found specifically in the chondrules of QUE 94366 CV, Figure2.32 (a), specifically in an inclusion of type I FeO chondrule, which is probable to have occurred due to the cool from high temperature, which encapsulated a carbon-rich gas inside[123]. Also, they have been found in compacted carbonaceous material within a dark inclusion of NWA 3118 CV3 meteorite and within a CAI rim of Allende meteorite[123]. Moreover, cualiflower-type and onion-type spherule graphite have been detected in Murchinson meteorite[114] which is speculated to be formed in environments of high saturation levels. In onion-type graphite, concentric shells of well-crystallized graphitic layers with nanocrystalline C cores[114] are seen in Figure 2.32 (c), while in cualiflower-type graphite, a turbostratic layering consisting of wavy and contorted graphene sheets[114] is observed in Figure2.32 (d).

Although the reported results from QUE 94366 and Allende CV3-type carbonaceous meteorite, the newest information about the discovery of nanoscale graphene morphologies within them has been revealed. After further analysis of both meteorites, Giri et al. (2021) have done a re-interpretation of the reported GWs and announced the discovery of nanoscale graphene, which has been found incorporated within a chondrule inclusion in QUE 94366 and the refractory CAI rims in Allende chondrite[10]. The composition
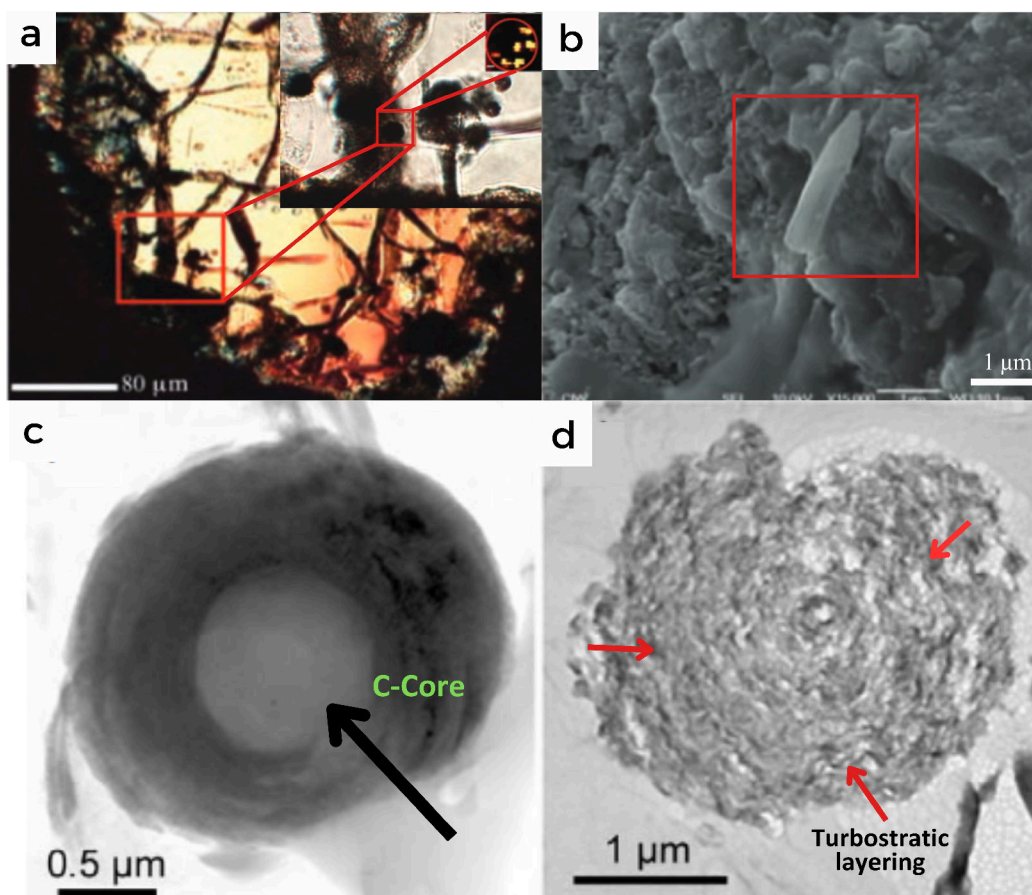
Figure 2.32: **TEM, SEM and transmitted light images of graphite within qUE 94366, Allende and Murchison meteorites.** a) Transmitted light image of chondrule in QUE 94366 meteorite seen in red square and b) SEM image of a whisker-like object with the "halved spindle" within a CAI from Allende meteorite. TEM micrographs of 70-nm-thick ultramicrotome sections of c) onion-type graphites with a nanocrystalline C core and d) cauliflower-type graphite with turbostratic layering from Murchison meteorite. © Adapted from Fries M. & Steel, A.[123] and Bernatowicz et al[114].

of CAIs and their rims are consistent with high-temperature (700 to $\leq$ 1500 K)[10] condensation of individual grains from a nebular gas[126]. One of the resultant confocal Raman imaging spectroscopy (CRIS) done in various GW within an Allende CAI inclusion shows ratio maps of $1 > I_{2D}/I_G < 2$ and $I_{2D}/I_G > 2$[10] in different spots seen in Figure 2.33, which correspond to bi-layer (2LG) and mono-layer graphene (1LG) respectively.
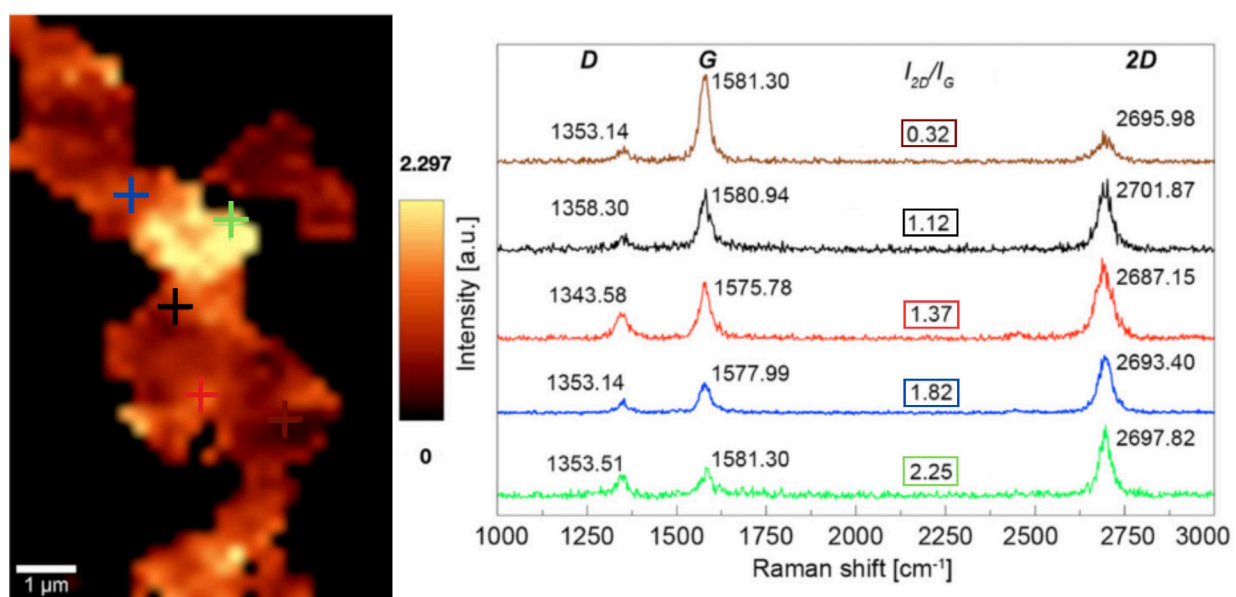
Figure 2.33: **CRIS and Raman spectra of nanoscale graphene and graphite whiskers within a CAI rim of Allende meteorite.** The I_{2D}/I_G on the brown cross corresponds to graphite, the green cross is due to 1LG, and in black, red, and blue crosses are produced by a 2LG. © Adapted from Giri et al. (2021)[10].

Chapter 3

Methodology

In this chapter, we show all the tools employed for the synthesis of graphene, characterization techniques, and the analysis of the results obtained, which are mainly summarized in two parts.

The first part is focused on the Chemical Vapor Deposition (CVD) + Thermal decomposition methods used for growing graphene on 6H-SiC (Size 1, Size 2, and Size 3) and the selected parameters (time, gasses, flow rate) used to achieve it. The second part shows the techniques used for the analysis of the samples, data processing, and peak assignment, based on the data obtained from X-ray Diffraction (XRD), Scanning Electron Microscopy (SEM), and Raman Spectroscopy characterization methods. In Figure 3.1 an experimental flowchart of the main processes is shown.
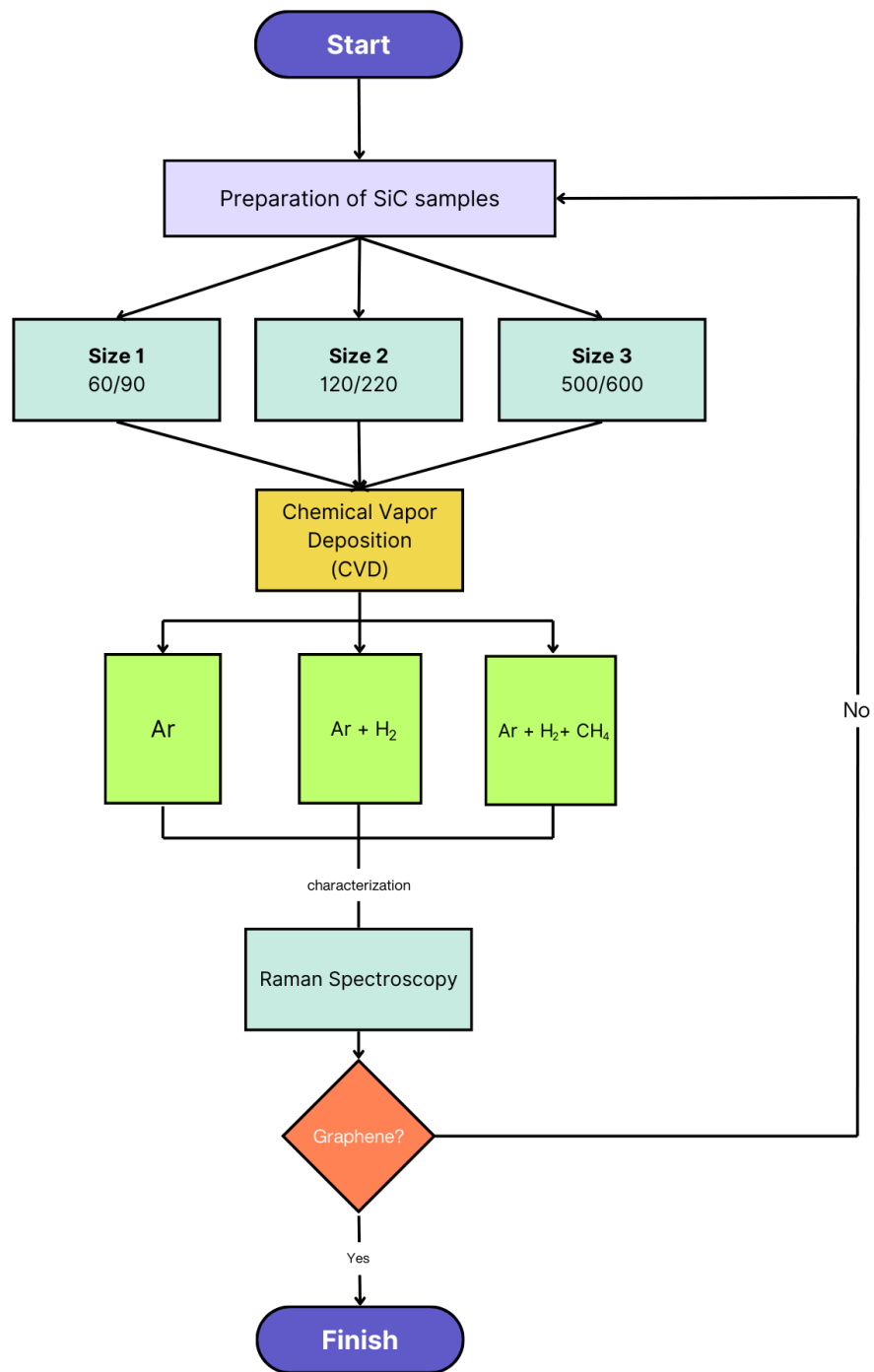
Figure 3.1: **Experimental process flowchart**

3.1   Materials

In this research, silicon carbide (SiC) was employed in three different grain size ranges, as specified in Table 3.1. There exist various international standards to identify the grain size of different abrasive materials in relationship to their mesh or grit size. In our case, the standard table used for classifying the grain size of our SiC samples was the American National Standards Institute (ANSI)[127].

Table 3.1: Silicon Carbide (SiC) grain size

# size	ANSI Grit Size	Particle size (μm)
One	60/90	>160, <250
Two	120/220	>58, <100
Three	500/600	>10.7, <14

Since SiC carbide is very used as an abrasive, it is commonly sold as part of kits for rock polish, for this reason, the material used comes from a Grit Kit for 3 LB Rock Polish (Figure 3.2), which was purchased from the US company "MJR Tumblers". Moreover, this research involved the use of a variety of gasses, such as hydrogen (H_2), methane (CH_4), and argon (Ar) at different flux rates. For the preparation of the SiC and the graphene synthesis, there were used heat-resistant (<1800°C) alumina (Al_2O_3) ceramic boats.

3.2   Preparation of SiC samples

The samples of SiC were prepared at Yachay Tech University (UITEY) before starting each synthesis. In other instances, the preparation was also carried out at San Francisco University (USFQ). In any case, both followed a strict protocol of preparation. First of all, the alumina ceramic boat (Al_2O_3) is placed separately on the atomic balance, Figure 3.3 (a), to be weighed. Then, we wait a few seconds to ensure that the displayed value on the balance is accurate. The same process is repeated for the other two boats. This is done to control the quantity of SiC used for the synthesis. Now, each boat is filled with each size of SiC before being weighed as seen in Figure 3.3 (b).

Figure 3.2: **Silicon Carbide (SiC) & Aluminium Oxide** (Al_2O_3**) grit kit.** Step 1, Step 2, and Step 3 samples are used changing their names to Size 1, Size 2, and Size 3, respectively. Figure taken from eBay website.

3.3   Chemical Vapor Deposition (CVD) + Thermal decomposition of SiC

A total of 8 synthesis attempts were done with different gasses, flow rate, time of synthesis, and temperature, with the use of the chemical vapor deposition chamber at Yachay Tech University and USFQ.

Graphene was synthesized by combining two methods: thermal decomposition of SiC and Chemical Vapor Deposition (CVD). From the first to the fifth attempt, the synthesis was done at Yachay Tech University the parameters used for the synthesis were kept unchanged in order to assess the reproducibility of the results obtained. The synthesis was done for Size 1, Size 2, and Size 3 SiC at the same time. In each case, the three samples were placed inside a quartz tube and moved until reaching the center of it.

The whole process was carried out on the central zone of the CVD chamber at 1000 °C with an Ar flow rate of 300 L/min for 120 mins, as specified in Table 3.2. The temperature of synthesis was reached at 10 °C per minute until 900 °C, after this, the process was slowed down to 5°C per minute until it reached the
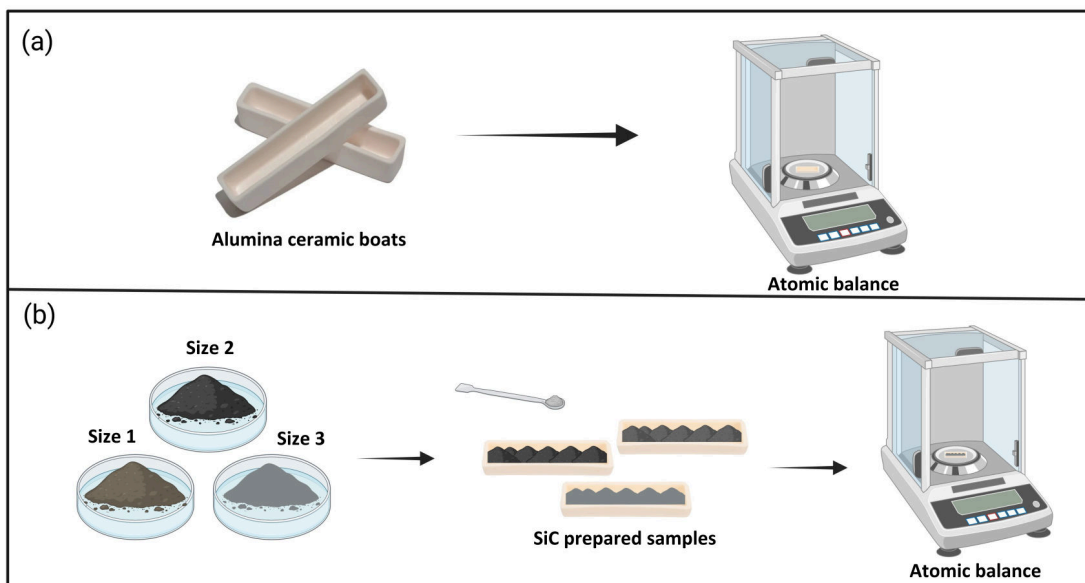
Figure 3.3: **Schematic process of SiC preparation.** Created with BioRender.com.

1000 °C. The actual configuration of the chamber is detailed in Table B.1. The chamber was set to stay at this temperature for 30 minutes to later stop the process. Finally, the system was left to cool down to reach room temperature in an Ar environment. In Figure 3.5 a detailed scheme of the process is illustrated.

Table 3.2: CVD parameters used for Graphene synthesis at UITEY

# Attempt	Gasses	Flux rate (L/*min*)	Total synthesis time
One			
Two			
Three	Argon (Ar)	0.3	120 mins
Four			
Five			
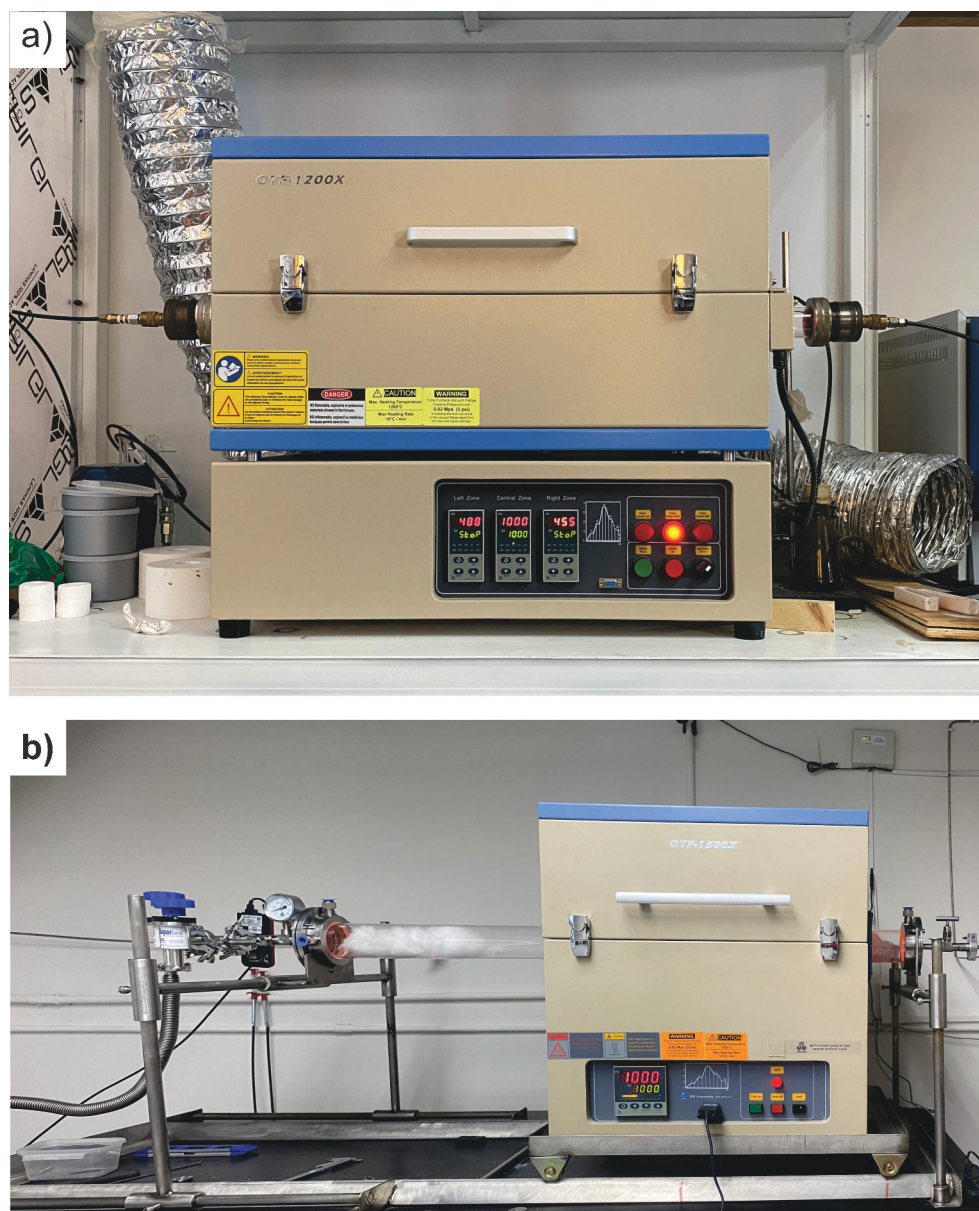
Figure 3.4: **Chemical Vapor Deposition chambers.** CVD furnances from (a) Yachay Tech (OTF-1200X from MTI Corporation) and (b) USFQ (OTF-1500X from MTI Corporation) used for graphene synthesis.
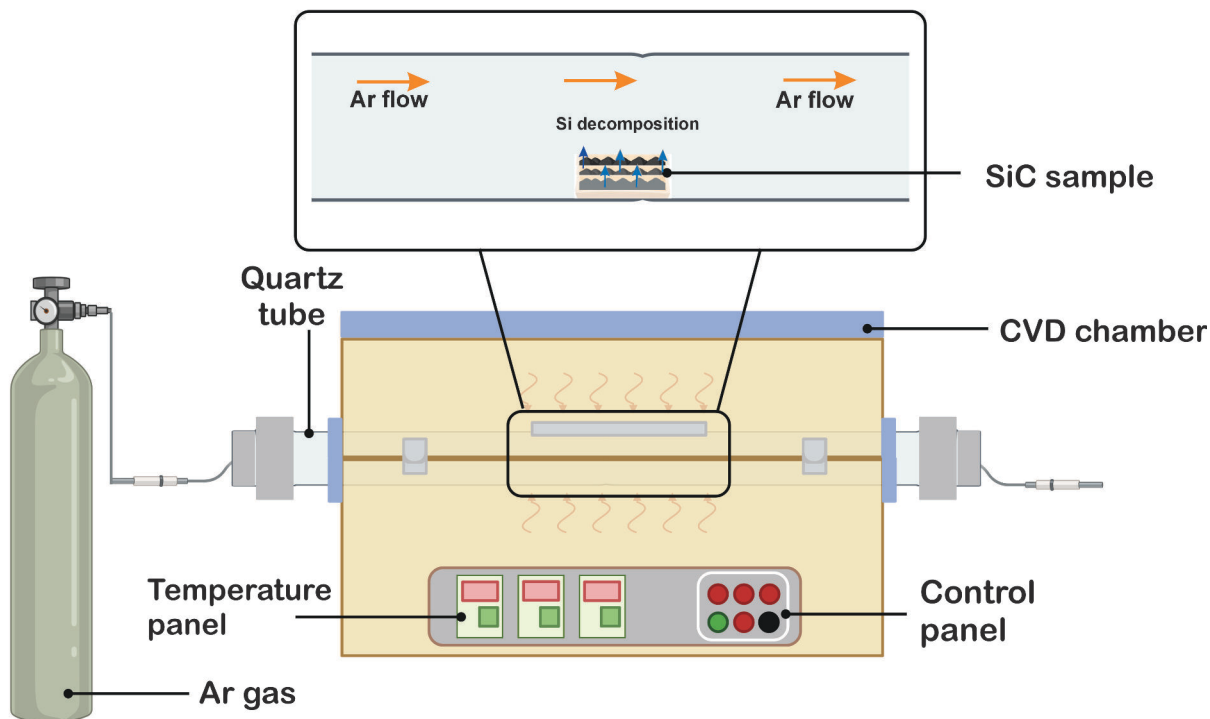
Figure 3.5: **Scheme of SiC CVD process at UITEY.** The three samples of SiC are placed within the quartz tube in an Ar environment to reach 1000 °C. After 70 minutes, silicon (Si) begins to sublimate, and carbon atoms arrange on the surface, forming a graphitic layer. Created with BioRender.com.

Table 3.3: CVD parameters used for Graphene synthesis at USFQ

# Attempt	Gasses	Flux rate (L/min)	Time
	Methane (CH_4)	0.01	10 mins
One	Argon (Ar)	0.5	415 mins
	Hydrogen (H_2)	0.08	30 mins
	Argon (Ar)	0.3	415 mins
Two	Hydrogen (H_2)	0.08	60 mins

Two additional synthesis processes were carried out at USFQ with the addition of two new gasses: H_2 and CH_4. The process parameters do not differ significantly from the previous one. However, the difference relies on the total time of synthesis and the variety of gasses employed. The heating ramp used in both attempts was 5 °C per minute during the whole process, as seen in Table B.1, which was the same temperature rate used for the cooling ramp. Again, the three samples were placed inside a quartz tube and moved to the right of the tube. Later, the tube is closed and set up in vacuum (0.12 Torr) before the synthesis. For the first attempt, seen in Table 3.3, an Ar flux of 0.5 L/min is ejected during all the process (415 mins). Then, a H_2 flux of 0.08 L/min is applied when the CVD chamber reaches 500 °C for 30 mins. Finally, a CH_4 flux of 0.01 L/min is applied during 10 mins, see Figure 3.6. For the second attempt, seen in Table 3.3, an Ar flux of 0.3 L/min is used during all the process (415 mins). Finally, a H_2 flux of 0.08 L/min is applied when the CVD chamber reaches 500 °C for 60 mins, with no methane gas used. After the process, the synthesized samples were collected in eppendorfs for their subsequent analysis.
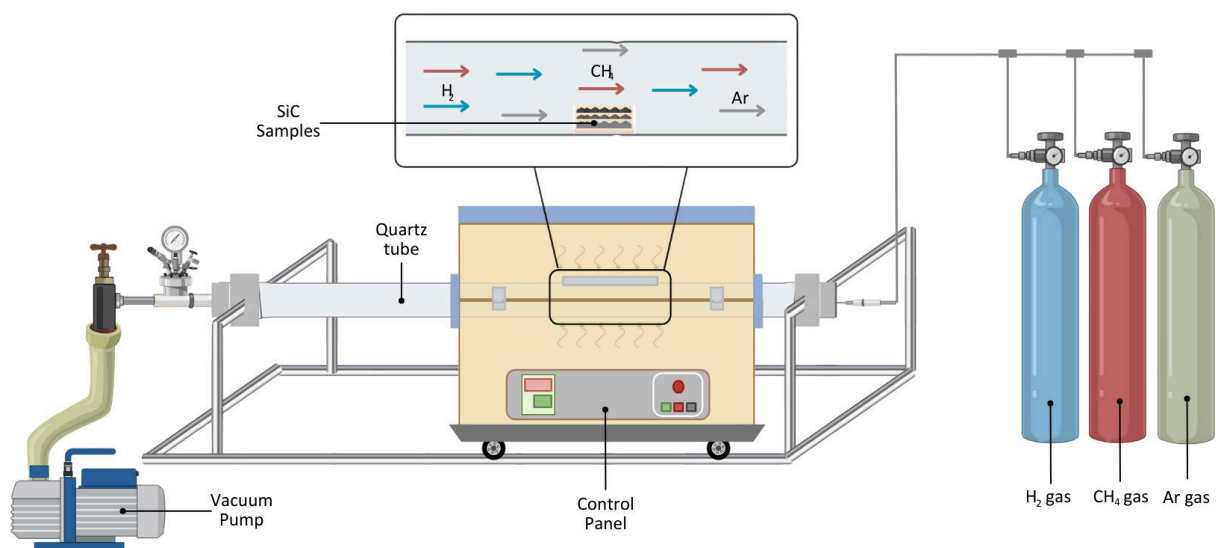
Figure 3.6: **Scheme of SiC CVD process at USFQ.** The three samples of SiC are placed within the quartz tube in an Ar + H_2 + CH_4 environment to reach 1000 °C for 230 mins. Created with BioRender.com.

The last attempt was done at Yachay Tech University using the same parameters as attempts 1-5, with the only difference being that time was increased to 230 mins with a heating ramp of 10° C/min until it reached 200 °C, then it was changed to 5 °C/min until 800 °C, finally the heating rate was set up to 4 °C/min until it reached 1000°C (see Table B.2). All the parameters used for the synthesis are seen in Table 3.4.

Table 3.4: CVD parameters used for Graphene synthesis at UITEY

# Attempt	Gasses	Flux rate (L/*min*)	Total synthesis time
One			
Two			
Three	Argon (Ar)	0.3	230 mins
Four			
Five			

3.4   Characterization Techniques

An important part of this research is the characterization techniques employed for the determination of the structural and elemental composition of our samples. Therefore, in this section, the methodology used in each characterization technique is detailed.

3.4.1   Raman Spectroscopy

The Raman spectroscopy analysis of all our pristine SiC and SiC + Graphene samples was done at Yachay Tech University laboratory, using the LabRam HR Evolution microscope seen in Figure 3.7. The sample preparation was done by putting our Size 1, Size 2, and Size 3 SiC grains on a carbon tape over a slide for later measurement. For both types of samples, the acquisition parameters used were: range from -20 cm^{-1} to 3500 cm^{-1} and an acquisition time of 5 s during 5 accumulations. The laser beam used for the measurements was of 532 nm since this is the excitation wavelength for C-C graphene bonds.
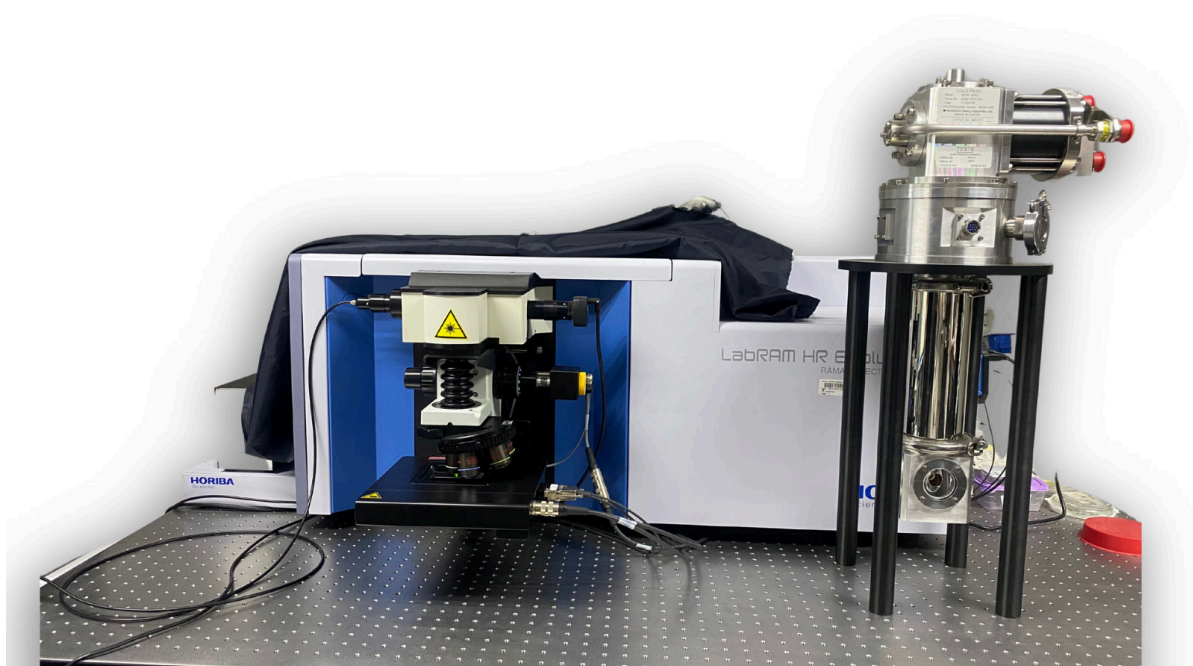
Figure 3.7: **LabRam HR Evolution microscope from UITEY**

SiC + Graphene Raman Mapping

Raman imaging or Raman mapping is a technique used for generating false color images of the composition and structure of a sample, based on hundreds or even millions of Raman spectra[55]. A Raman map was measured over a rectangular area of the synthesized sample (Figure 3.8), by using an objective of 50x and 1 second acquisition time, over a range of 12 x 8 points.
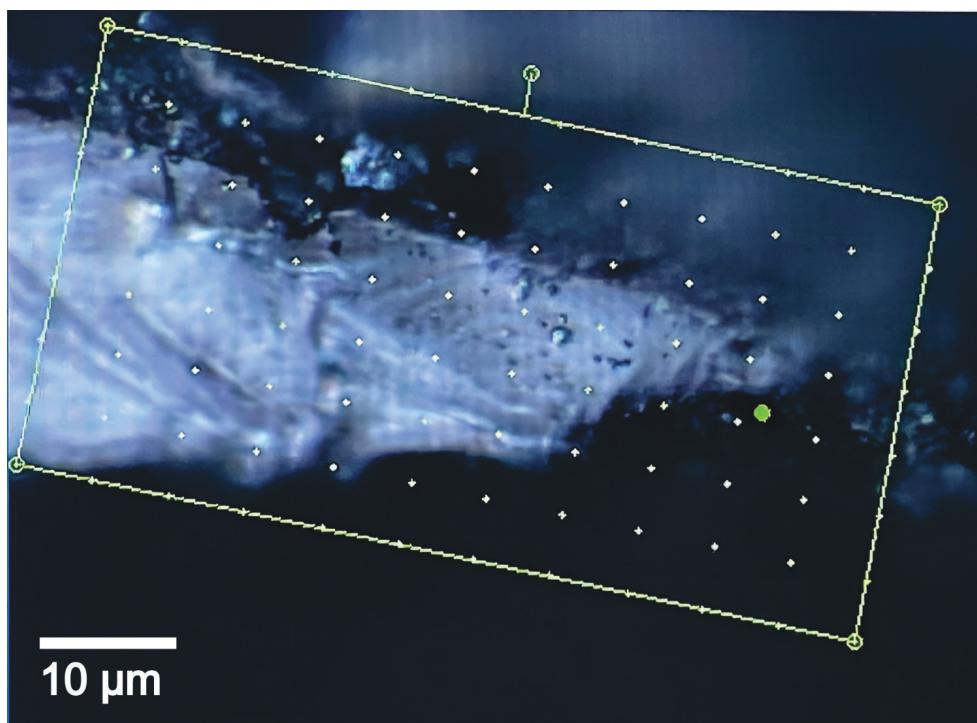
Figure 3.8: **Optical image of Raman mapping area.** The rectangular area was analyzed across a range of 12 x 8 points at 1 second acquisition time by using the LabRam HR Evolution microscope

3.4.2 X-Ray Diffraction (XRD)

This technique was used for the characterization of pristine SiC related to each size, in order to identify its predominant phase. The diffractometer used in this analysis was a Rigaku Mini Flex (G6) from Yachay Tech University, which has an autosampler of 8 positions and a HyPix-400 MF (2D HPAD) detector. Among its additional features, it uses an X-ray source of CuKα radiation operated at 40 kV and 15 mA. It has a potency of 600 W and 60/50 Hz. The 2θ was set up to collect the SiC data from 5° to 80°, in steps

of 0.01°, and a speed of 10 °/min.

Figure 3.9: **Mini Flex (G6) X-ray Diffraction.** Diffractometer used for identifying the phase of SiC grains.

The preparation process of the SiC samples for the XRD measurements, seen in Figure 3.10, was done by putting the samples of Size 1, Size 2, and Size 3 on a sample holder with a spatula. The samples must be adjusted to the size and depth of the holder with a piece of glass so that the sample fits without holes or bulges. After, the borders of the sample holder must be cleaned with a brush to get rid of any waste.

SiC
Size 1

SiC
Size 2

SiC
Size 3
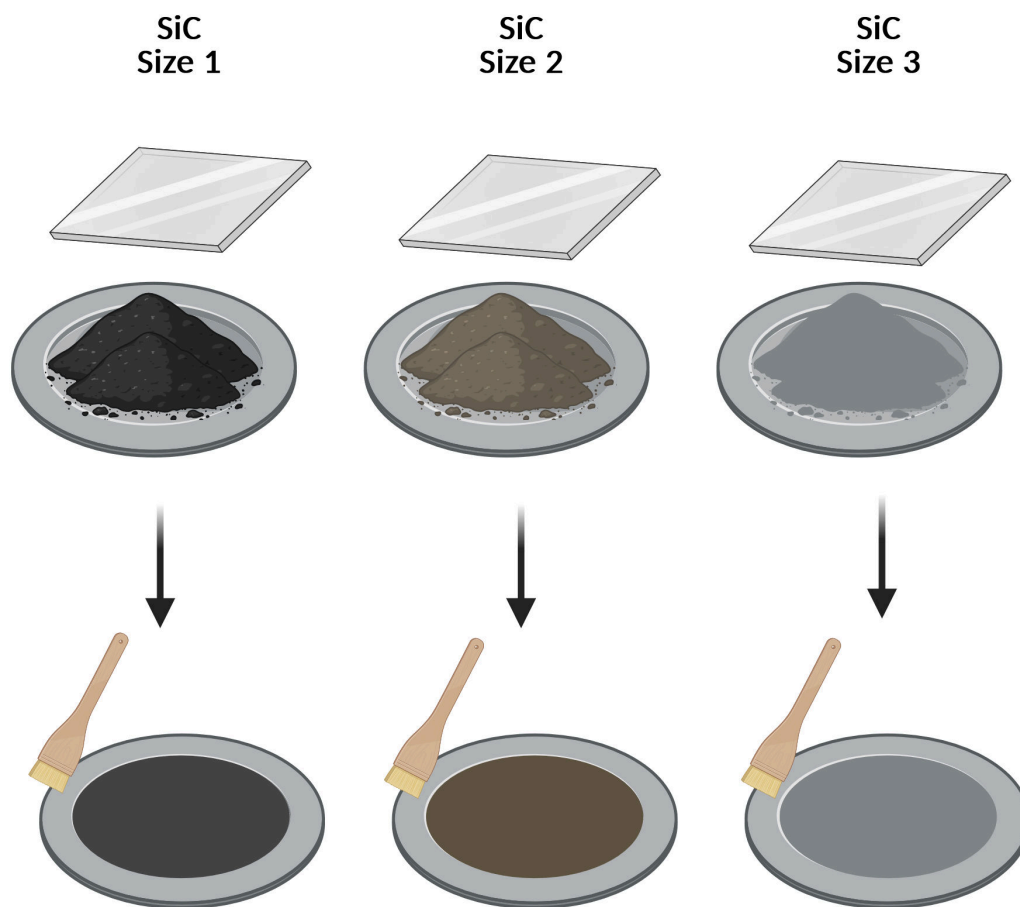
Figure 3.10: **Process of XRD samples preparation.** The samples are adjusted to the size and depth of the holder with a piece of glass, then the borders must be cleaned with a brush to get rid of any waste.

However, in the case of Size 1, it was quite different due to the grain size of SiC. Unfortunately, the mechanism of the Yachay Tech diffractometer works by moving the autosampler at the 2θ angle we are doing the measurement while the laser beam and detector are fixed. For this reason, we used an alternative method to fix the grains over the sample holder by using a double-sided tape so that the grains would not fall during the measurement process, see Figure 3.11 (a). After all, the samples are placed on 3 of the 8 positions of the XRD autosampler as seen in Figure 3.11 (b) (only Size 1 is shown).
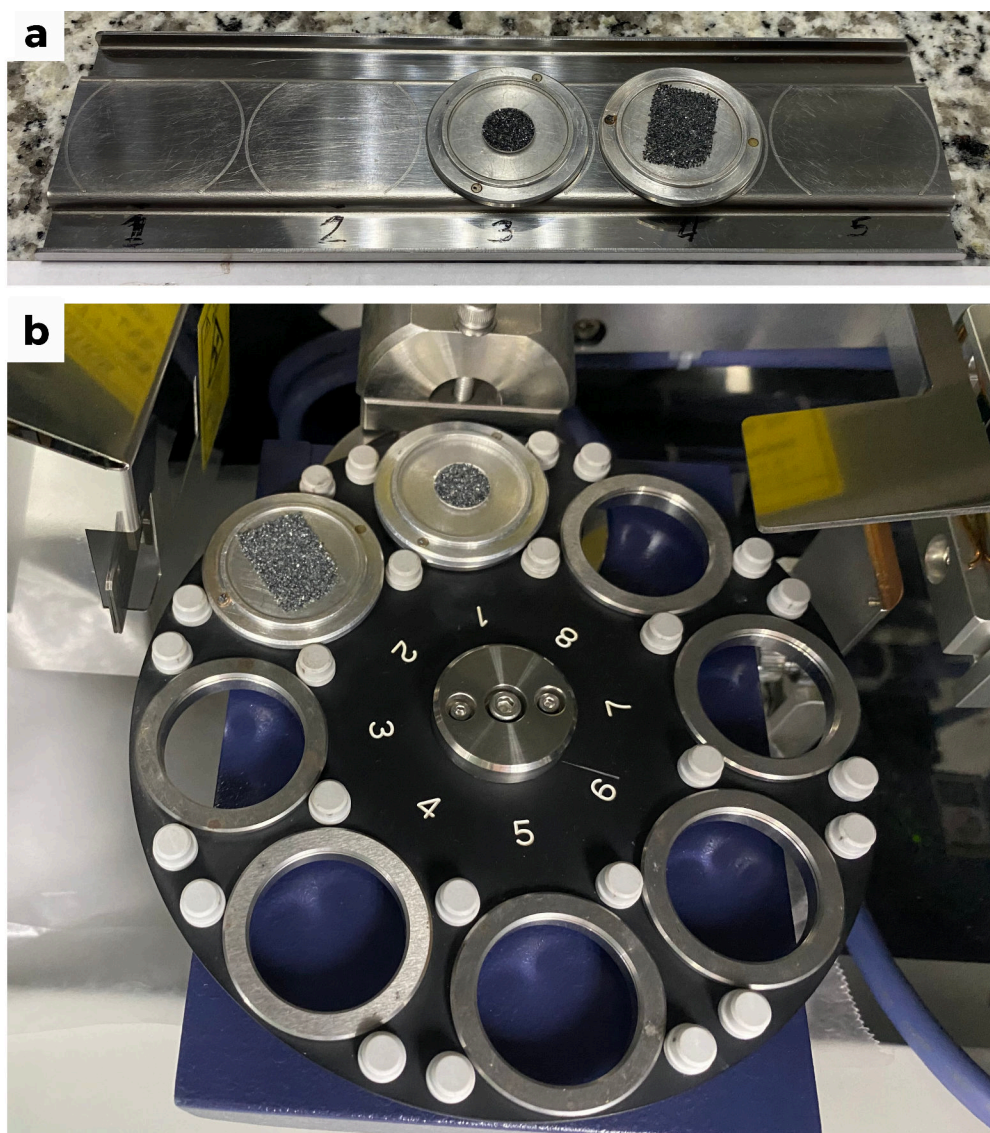
Figure 3.11: **Preparation of Size 1 SiC sample for XRD measurements.** Size 1 SiC (a) pasted in a double-sided tape over a sample holder and finally (b) placed on the autosampler.

3.4.3   Scanning Electron Microscopy (SEM)

Even though the grain size of our SiC samples was already estimated in Section 3.1 from the grit size information seen in the product, it was necessary to confirm that these values were the correct ones. For this reason, a scanning electron microscopy characterization was done in order to measure the mean grain size of the SiC grains. These images were obtained using a SEM feature of the PHI 5000 Versaprobe II XPS (see Figure 3.12). The surface morphology, texture, and topology of the SiC grains are seen as a result of the interaction of a beam of electrons with the sample. Then, secondary electrons are generated, detected, and captured for generating high-resolution images[128]
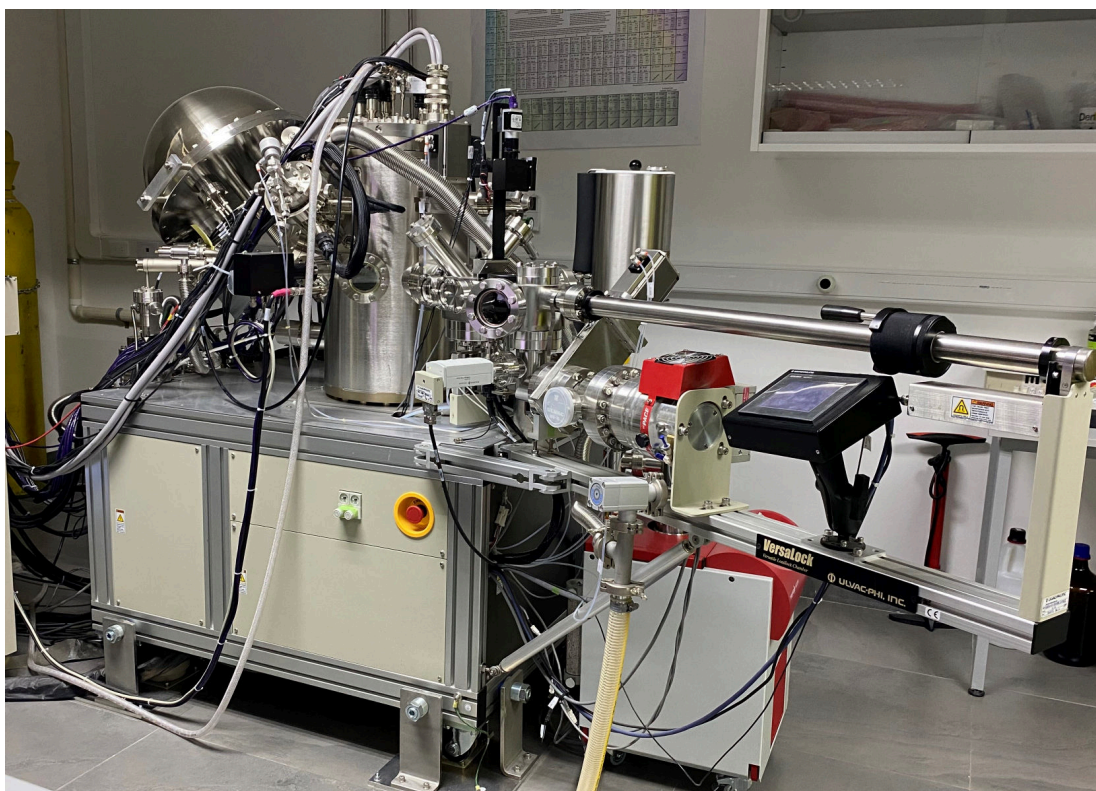
Figure 3.12: **PHI 5000 Versaprobe II XPS used for the SEM characterization of SiC grains.**

Chapter 4

Results & Discussion

This section will discuss all the results obtained from the characterization of our SiC samples and the CVD synthesis, as well as its astrophysical implications, which will be divided into four main sections. In Section 4.1 the polytype identification and peak assignment of our SiC samples via XRD and Raman spectroscopy are shown. Section 4.2 will cover the results from the synthesized SiC in Ar environment samples, where the reproducibility of the experiment, the most probable growth zones, the number of layers, and the defects of the resultant graphene are discussed. After this, the results of the experiment reproduced using different gasses, time, and pressure are presented in Section 4.3. Finally, the astrophysical implications that our results have over previous research done and real interstellar conditions are discussed in Section 4.4.

4.1 SiC samples characterization

4.1.1 X-Ray diffraction

In order to know what polytype we are working with and to understand the behavior of the structures formed over our pristine SiC, XRD measurements for Size 1, Size 2, and Size 3 SiC were done.

First of all, the diffractogram of Size 1 SiC seen in Figure 4.1 shows the most prominent 2θ angles in 21.79°, 25.42°, 34.39°, 35.4°, 37.88°, 41.26°, 43.17°, 45.13°, 52.35°, 54.56°, 57.29°, 59.8°, 65.44°, 68,11°, 71.58°, 73.28°, 75.19°, which match with PDF 96-901-0159, corresponding to 6 hexagonal SiC (α-SiC) or best called Moissanite, also illustrated in Figure 4.1. However, some of these angles differ in a shift of 3° to 30°, which can be attributed to stacking faults, as well as internal stresses that the sample could have suffered[129].
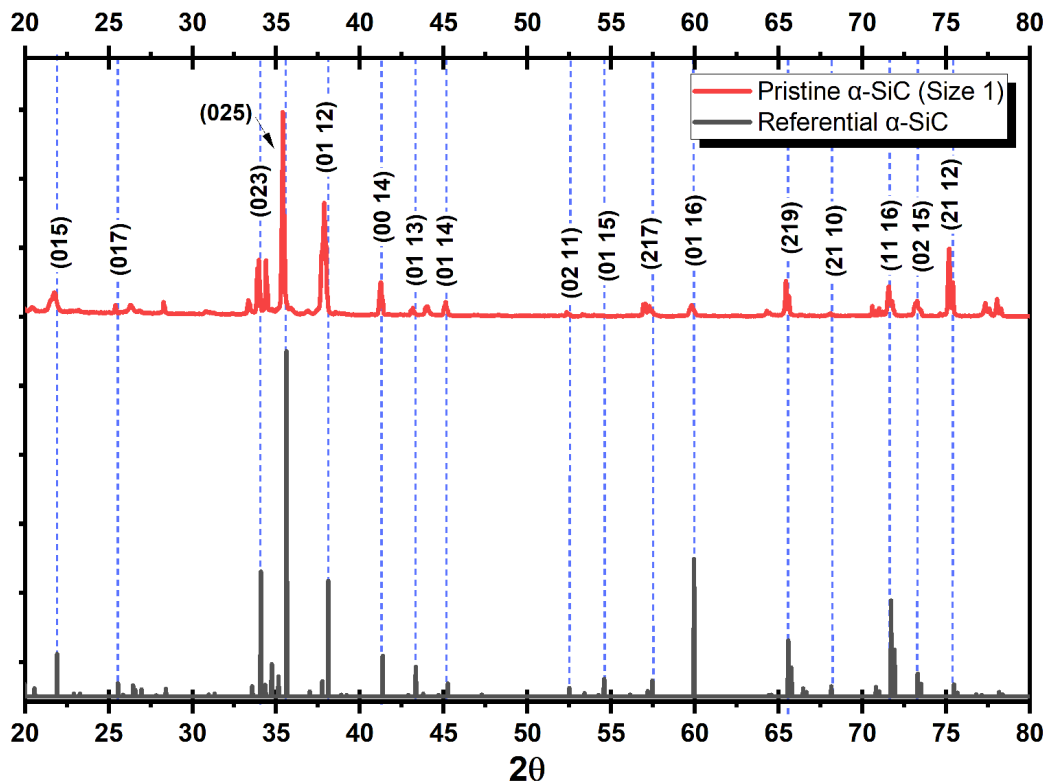
Figure 4.1: **XRD difractogram of Size 1 SiC and referential α-SiC** measured from 5° to 80° and their corresponding planes.

Also, some intensities differ from the ones of the referential α-SiC, which could be due to the arrange-
ment of the grains. Here, the preferred orientation of the sample was altered in the degree of alignment
and direction [130] by fixing the grains over a scotch tape for taking the XRD measurement.
The diffractogram of Size 2 SiC seen in Figure 4.2 also matches with 6 hexagonal SiC (α-SiC), but it shows
almost the same difference in angles as our previous sample. In Table 4.1, we can see that the shift is of
2° to 14°, which is considerably smaller than the one produced in Size 1 SiC. Nevertheless, in Figure 4.3,
the diffractogram for pristine Size 3 SiC shows 2θ angles that match perfectly with hexagonal SiC phase
(6H-SiC) of PDF number 96-101-1054, as seen in Table 4.1. In some cases, the angle only differs in 1°.
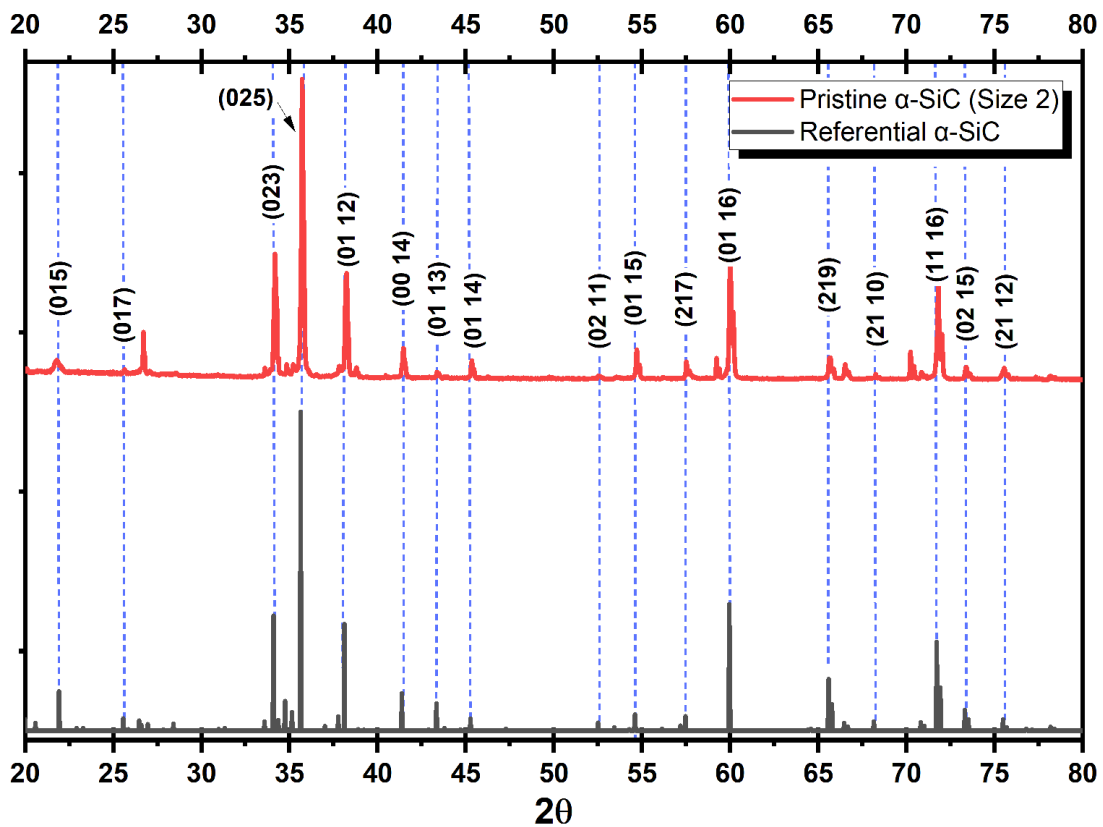
Figure 4.2: **XRD difractogram of Size 2 SiC and referential α-SiC** measured from 5° to 80° and their
corresponding planes.
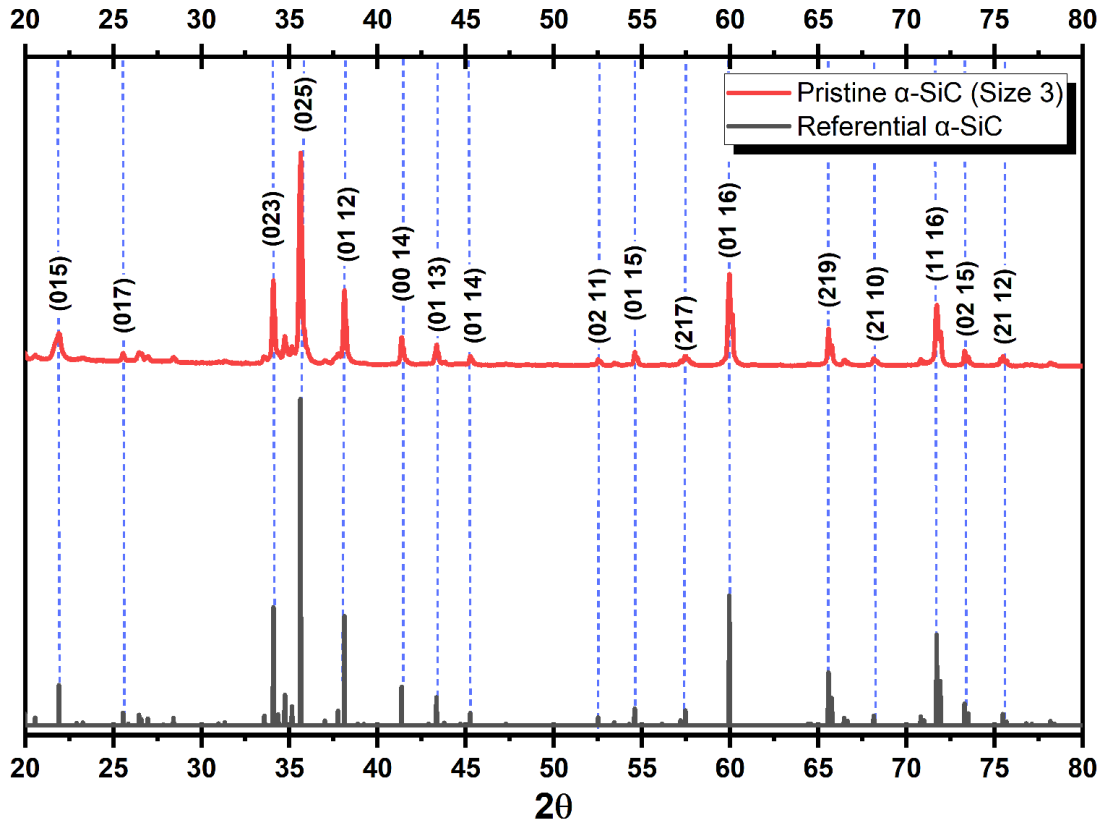
Figure 4.3: **XRD difractogram of Size 3 SiC and referential α-SiC** measured from 5° to 80° and their corresponding planes.

In summary, the appropriate planes ($h\,k\,l$) and angles (2θ) supporting these results can be seen in the comparative Table 4.1. As explained in Section 2.3.3, these planes with Miller indices h, k, l, are the corresponding ones caused by the diffraction pattern of this 6H-SiC polytype. Furthermore, a comparative plot of pristine Size 1, Size 2, and Size 3 is shown in Figure 4.4, which shows the similarities in the diffraction angles with respect to α-SiC.
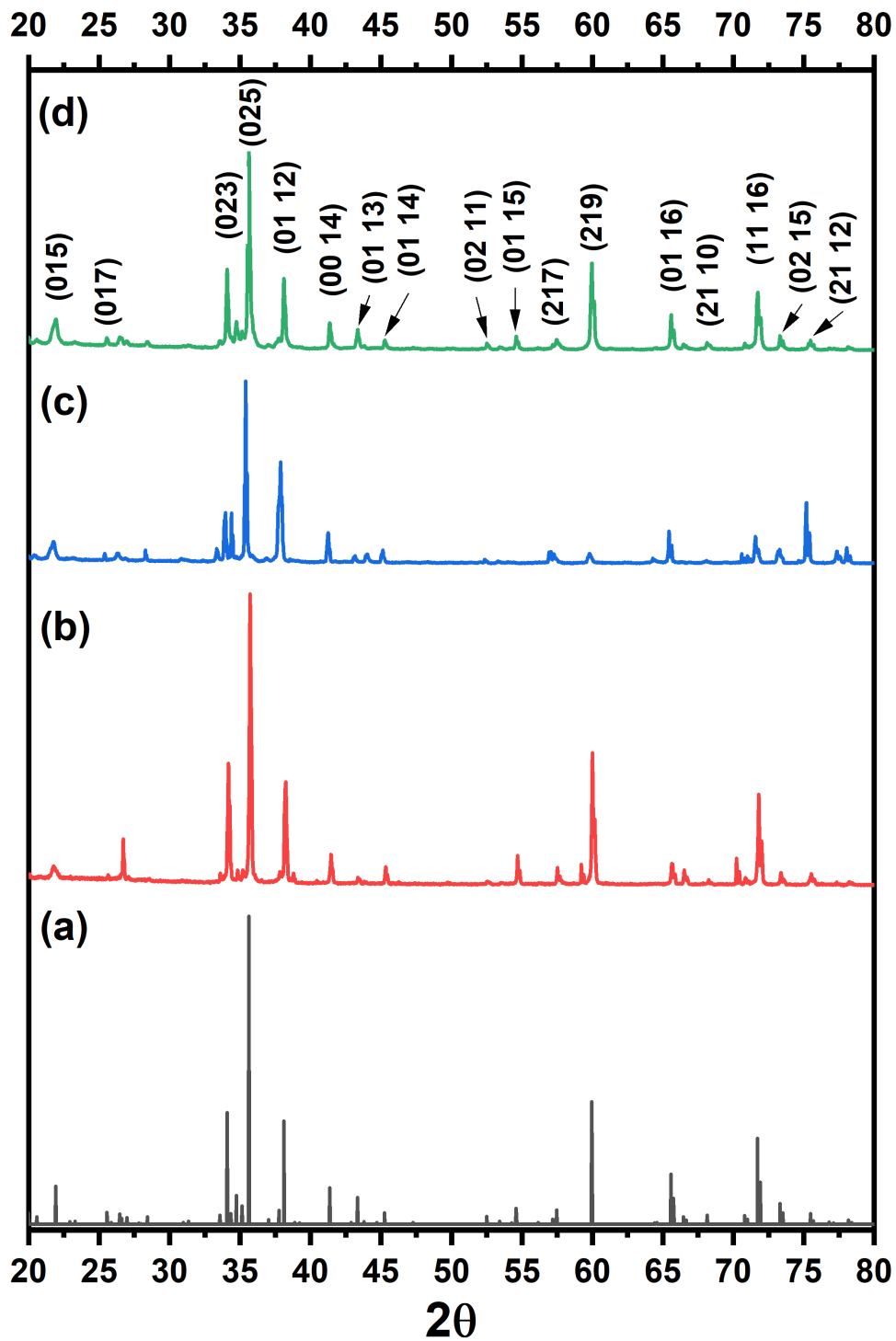
Figure 4.4: **XRD diffractograms of (b) Size 2, (c) Size 1, and (d) Size 3 SiC** measured from 5° to 80°and their corresponding planes, compared with (a) pristine 6H-SiC.

Planes			2θ (°)			
h	k	l	α-SiC	Size 1	Size 2	Size 3
0	1	5	21.92	21.79	21.78	21.91
0	1	7	25.56	25.42	25.64	25.56
0	2	3	34.08	34.39	34.18	34.08
0	2	5	35.62	35.4	35.72	35.63
0	1	12	38.11	37.88	38.25	38.11
0	0	14	41.36	41.26	41.47	41.37
0	1	13	43.34	43.17	43.36	43.35
0	1	14	45.26	45.13	45.34	45.29
0	2	11	52.51	52.35	52.58	52.51
0	1	15	54.59	54.56	54.68	54.59
2	1	7	57.46	57.29	57.51	57.47
0	1	16	59.95	59.8	60.01	59.97
2	1	9	65.58	65.44	65.68	65.59
2	1	10	68.15	68.11	68.25	68.16
1	1	16	71.72	71.58	71.81	71.73
0	2	15	73.31	73.28	73.4	73.31
2	1	12	75.48	75.19	75.55	75.49

Table 4.1: 2θ diffraction angles and its crystallographic planes (*h k l*) for SiC samples.

4.1.2 Scanning Electron Microscopy

In Figure 4.5 (a), (b), and (c), we can see a SEM image of Size 1 SiC grains, where irregular angular morphologies can be seen, specifically subhedral and anhedral shapes, very characteristic of SiC[131]. Regarding its particle size, the measurement done in ImageJ gives us a particle size range from $180\,\mu$m to $700\,\mu$m, as seen in Figure 4.6. In this histogram, we can see that the particle size distribution of the grains is mostly ranging around $250\,\mu$m and $450\,\mu$m. Also, this data has been fitted to a normal distribution, giving us a mean grain size of $\bar{x}$=340.91 μm for this size. These measurements differ significantly from the quantities in Table 3.1 given in the literature[127].

For Size 2 SiC, Figure 4.7 (a) also shows grains with irregular angular shapes, as well as it is visible that the particle size is smaller than the previous one. In this case, the measurement done gives us a particle size range from $90\,\mu$m to $190\,\mu$m, as seen in Figure 4.8 (a). In this histogram, we can see that the particle size distribution of the grains is mostly ranging around $110\,\mu$m and $150\,\mu$m. The Gaussian fit of this data gives an average grain size of $\bar{x}$= 143.45 μm for this size.

Finally, for Size 3 SiC it was a bit difficult to identify the particles; however, in Figure 4.7 (b) we can distinguish some of them. In this case, the measurement done gives us a particle size range from $30\,\mu$m to $90\,\mu$m, as seen in Figure 4.8 (b). For this plot, we can see that the particle size distribution of the grains is mostly ranging around $55\,\mu$m and $85\,\mu$m. The Gaussian fit of this data gives an average grain size of $\bar{x}$= 70.43 μm for this size. Also, in these last cases, the particle size ranges differed from the ones given in Table 3.1.
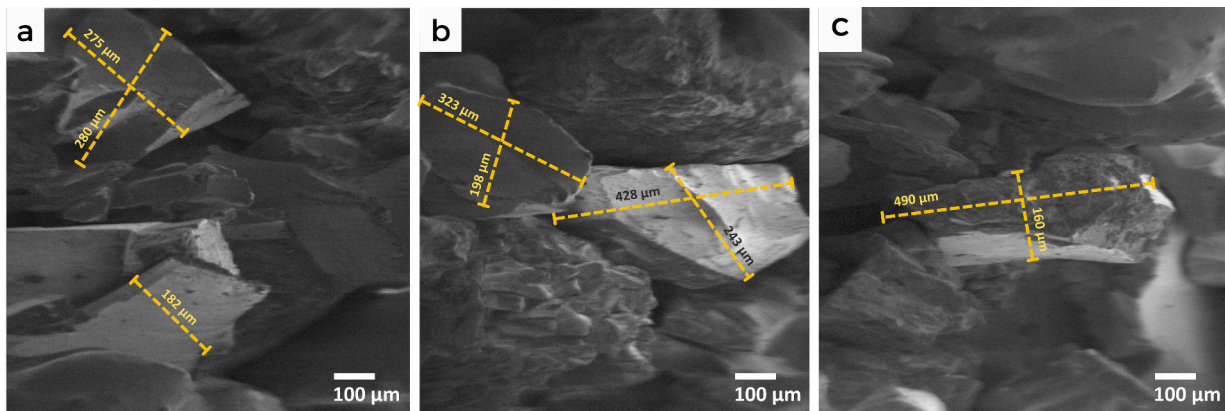
Figure 4.5: **SEM micrographs of Size 1 SiC grains with their respective grain size.**
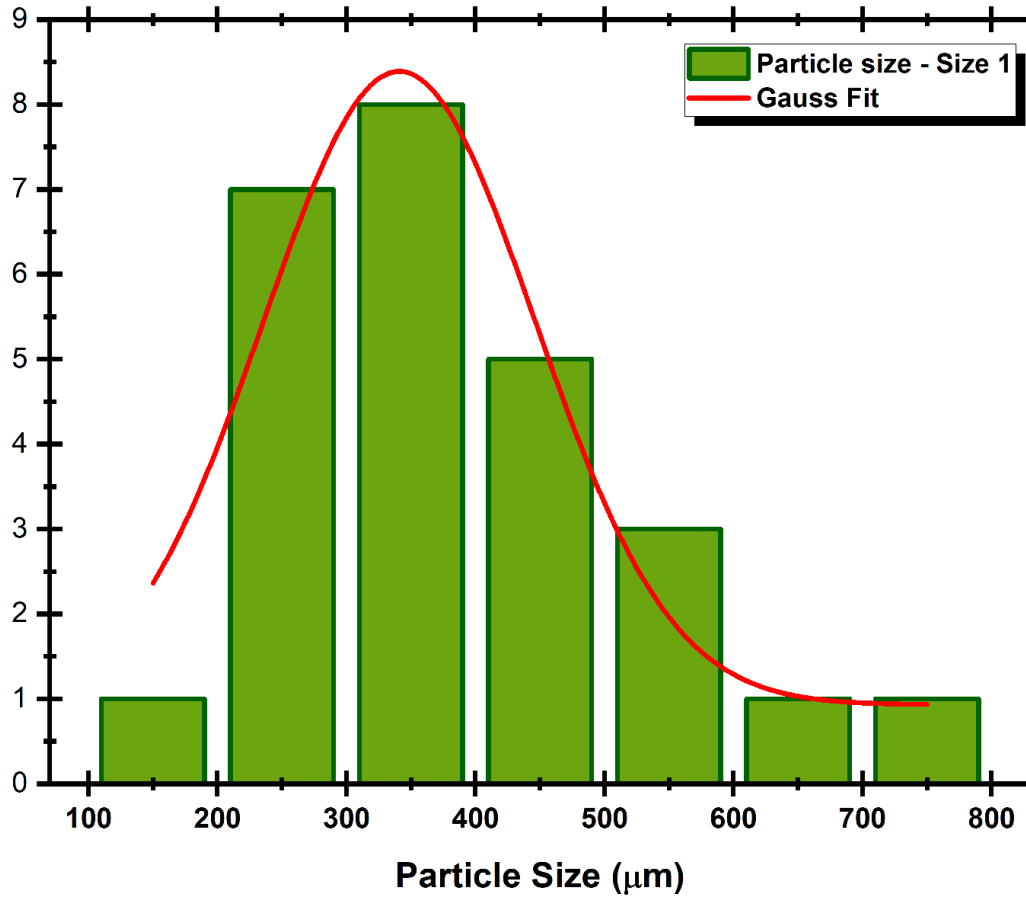
Figure 4.6:   **Histogram and Gauss fitting for Size 1 SiC grains** with a mean grain size of $\bar{x}$=341 μm.
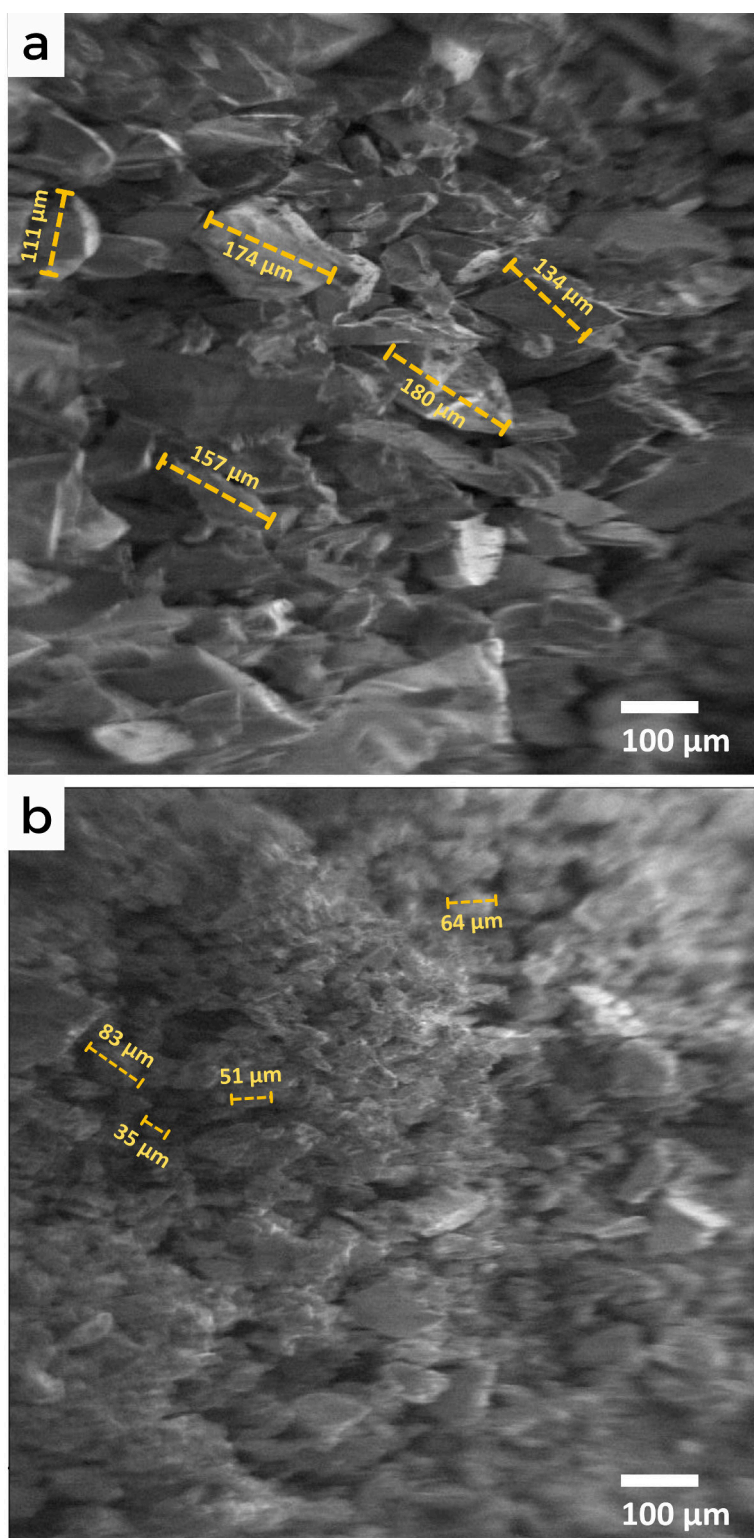
Figure 4.7: **SEM micrographs** of (a) Size 2 and (b) Size 3 SiC grains with their respective grain size.
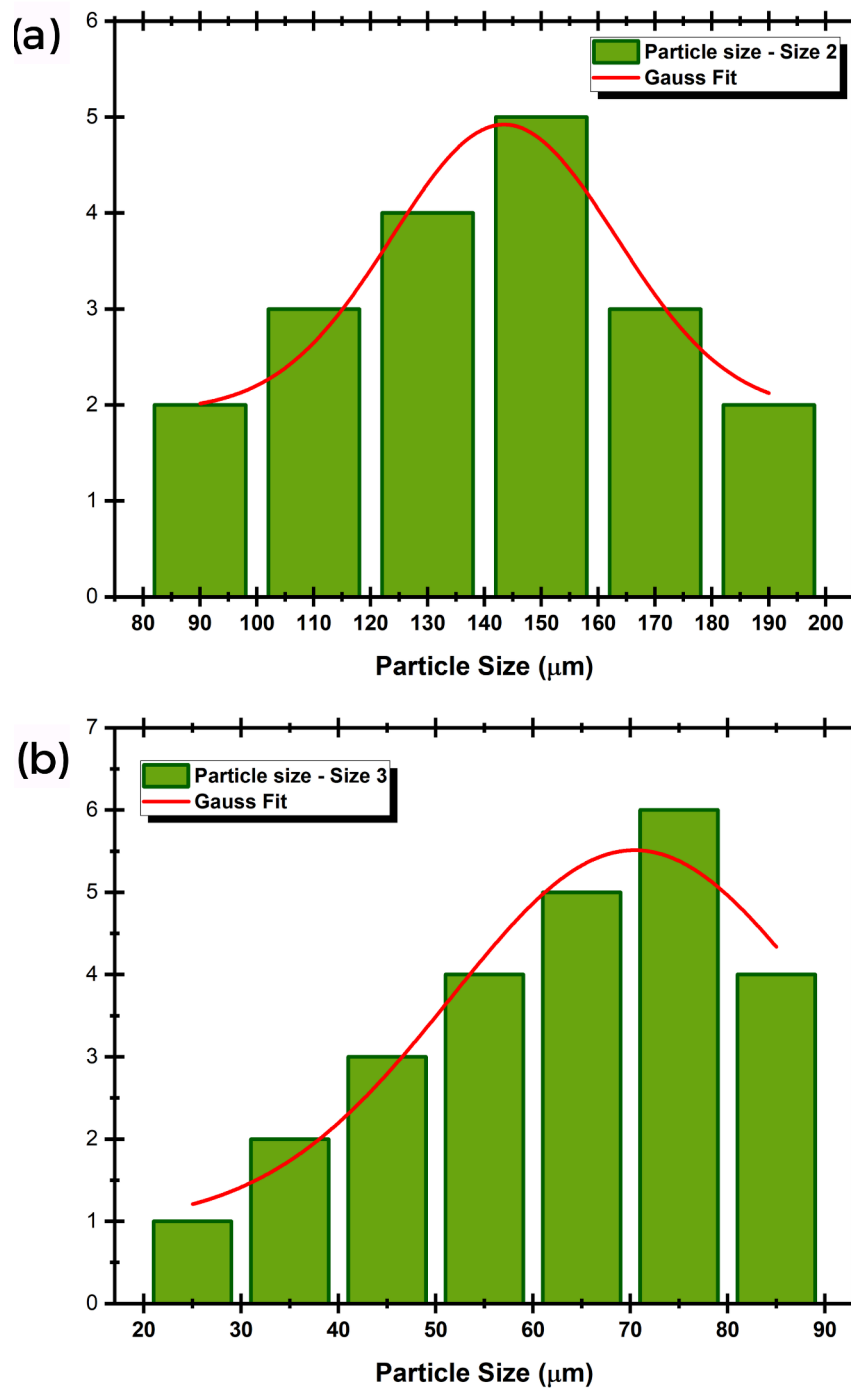
Figure 4.8:   **Histogram and Gauss fitting** for (a) Size 2 and (b) Size 3 SiC grains with a mean grain size of $\bar{x}$= 143.45 μm and $\bar{x}$= 70.43 μm respectively.

4.2   Synthesized SiC samples with Argon

In this section, the Raman spectra of Size 1, Size 2, and Size 3 SiC after the CVD process in an Ar environment are compared with a spectrum of graphene over a Si substrate. The level of defects and estimated number of layers present in the synthesized graphene are discussed in detail.

4.2.1   Raman Spectroscopy

The Raman spectra of the characterized samples from attempt 1 are shown in Figure 4.9. To begin, we can observe FTO (785.63 cm^{-1}) and FLO (970.42 cm^{-1}) Raman modes from the remaining SiC samples, which arise with very low intensities. At first sight, we can notice that there exists a small blueshift of the 2D band with respect to our referential graphene, which shifts to 2711 cm^{-1}, 2698 cm^{-1} and 2713 cm^{-1} for Size 1, Size 2, and Size 3 respectively. This is the result of the interaction between planes in few-layer and multi-layer graphene, which alters its electronic band structure[132] reflected in the dispersive 2D band. This fact is confirmed by the full width and half maximum (FWHM) of each spectrum, calculated with a Voight fitting. The peak width for a single layer graphene is considered to be 24-30 cm^{-1}[133], in our case, this value increases to 46.90 cm^{-1}, 37.697 cm^{-1}, and 57.8987 cm^{-1}, for Size 1, Size 2 and Size 3 samples, implying that Size 2 graphene has a smaller number of layers, compared with Size 1, and Size 3, which have the highest.

Furthermore, in comparison with the pure graphene sample spectrum, our synthesized graphene has a great amount of disorder, derived from the 2D band, which is seen in the formation of the D band. This is supported by the I_D/I_G ratio[61], where Size 3 graphene is the most defective of the three samples, while Size 2 is the lesser one. A summary of the information corresponding to the I_D/I_G ratio, peak position, and FWHM of the 2D band for attempt 1 samples, is seen in Table 4.2.

	Peak position (cm^{-1})	**FWHM** (cm^{-1})	I_D/I_G
Size 1	2711	46.90	0.38
Size 2	2698.38	37.7	0.27
Size 3	2713.5	57.9	0.82

Table 4.2: Synthesized graphene data for Attempt 1

Figure 4.9: **Raman spectra of attempt 1 α-SiC after CVD vs Graphene over a Si substrate.** The presence of graphene from Size 1 (red), Size 2 (blue), and Size 3 (purple) SiC is confirmed from the arising of D, G, and 2D bands. The corresponding level of defects for graphene is given by the I_D/I_G ratio.

From the second attempt shown in Figure 4.10, we can also observe a small shift in the 2D band for Size 1, Size 2, and Size 3 graphene, whose values are 2704.7 cm^{-1}, 2707.43 cm^{-1} and 2712.5 cm^{-1}, respectively. This shift produced by the interaction between graphene planes is confirmed by the FWHM which shows values of almost the double peak width for one-layer graphene (see Table 4.3). In Size 2 and Size 3 spectra, we can notice the presence of remaining SiC Raman modes, FTO and FLO, at 799 cm^{-1} and 975 cm^{-1} respectively. With respect to the level of disorder, we can observe that graphene has a high level of defects in the Size 2 sample, which corresponds to a ratio of I_D/I_G=0.6, while synthesized graphene from Size 1 has a small level of defect, with a ratio of I_D/I_G= 0.39.

	Peak position (cm^{-1})	**FWHM** (cm^{-1})	I_D/I_G
Size 1	2705.7	52.11	0.39
Size 2	2707.43	66.54	0.60
Size 3	2712.5	68.58	0.56

Table 4.3: Synthesized graphene data for Attempt 2

In Figure 4.11, the Raman spectra of synthesized graphene in attempt 3 are shown. In this case, we also see a small shift in the 2D band for each one of the steps. These values are 2728.28 cm^{-1}, 2713.5 cm^{-1}, and 2700.7 cm^{-1} for Size 1, Size 2, and Size 3 synthesized graphene respectively. The cause of this behavior in the band is the existence of many layers of graphene, which is confirmed by the FWHM of each sample. These values are 82.71 cm^{-1}, 72.49 cm^{-1}, and 62.47 cm^{-1}, for Size 1, Size 2, and Size 3 respectively. In the Size 2 spectrum, we can also observe the presence of the FTO (798.68 cm^{-1}) Raman mode of SiC. From the I_D/I_G ratio, we can deduce how defective the graphene produced was in this synthesis, then the values for each case are 0.40, 0.38, and 0.21, respectively. These results can be seen reflected in the intensity of the D bands of each size. A summary of the information corresponding to the I_D/I_G ratio, peak position, and FWHM of the 2D band for attempt 3 samples, is seen in Table 4.4.

	Peak position (cm^{-1})	**FWHM** (cm^{-1})	I_D/I_G
Size 1	2728.28	87.82	0.40
Size 2	2713.5	72.49	0.38
Size 3	2700.7	62.47	0.21

Table 4.4: Synthesized graphene data for Attempt 3

Figure 4.10: **Raman spectra of attempt 2 α-SiC after CVD vs Graphene over a Si substrate.** The presence of graphene from Size 1, Size 2, and Size 3 SiC is confirmed from the arising of D, G, and 2D bands. The corresponding level of defects for graphene is given by the I_D/I_G ratio.
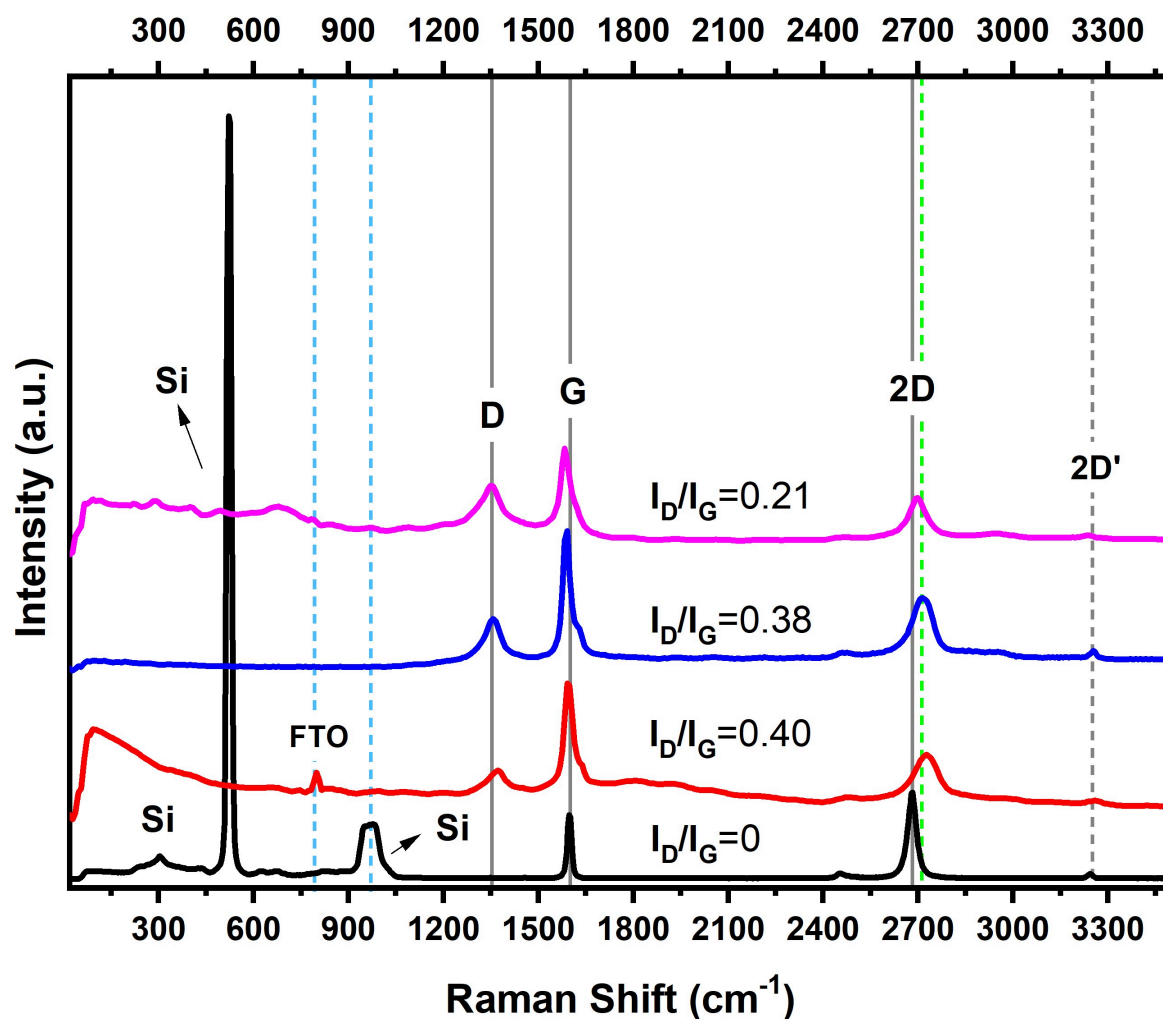
Figure 4.11: **Raman spectra of attempt 3 α-SiC after CVD vs Graphene over a Si substrate (black).** The presence of graphene from Size 1 (red), Size 2 (blue), and Size 3 (purple) SiC is confirmed from the arising of D, G, and 2D bands. The corresponding level of defects for graphene is given by the I_D/I_G ratio.

In attempt 4 seen in Figure 4.12, an interesting behaviour of the 2D band was seen. Here, the graphene synthesized in the three steps showed the same blueshifted peak value for this band (2706.7 cm^{-1}). However, a change in their FWHM value of each size can be seen in Table 4.5. This could have been possible due to the high amount of defects in the graphene structure, which causes the broadening of the 2D band[134]. These defects are quantified by the I_D/I_G ratio, giving us 0.46, 0.74, and 0.66 ratios for Size 1, Size 2, and Size 3 graphene samples respectively. A summary of the information corresponding to the I_D/I_G ratio, peak position, and FWHM of the 2D band for attempt 4 samples, is seen in Table 4.5.

	Peak position (cm^{-1})	**FWHM** (cm^{-1})	I_D/I_G
Size 1	2706.7	50.52	0.46
Size 2	2706.7	45.52	0.74
Size 3	2706.7	40.48	0.66

Table 4.5: Synthesized graphene data for Attempt 4

Finally, for attempt 5 we can also observe a small blueshift in the 2D peak for the synthesized graphene in all sizes (see Figure4.13). In this case, Size 1 graphene has the highest blueshift (2713.5 cm^{-1}), while Size 2 and Size 3 have smaller shifts, 2706.7 cm^{-1} and 2708.9 cm^{-1} respectively. The FWHM confirms that here exists the interaction between 2 and more layers of graphene, which shows values of 67.87 cm^{-1}, 47.01 cm^{-1}, and 65.72 for Size 1, Size 2, and Size 3 respectively. Moreover, the level of defects present in graphene is calculated with the I_D/I_G, (see Table 4.6), where Size 2 graphene appears to be the most defective one (I_D/I_G=0.68).

	Peak position (cm^{-1})	**FWHM** (cm^{-1})	I_D/I_G
Size 1	2713.5	67.87	0.67
Size 2	2706.7	47.01	0.68
Size 3	2708.9	65.71	0.56

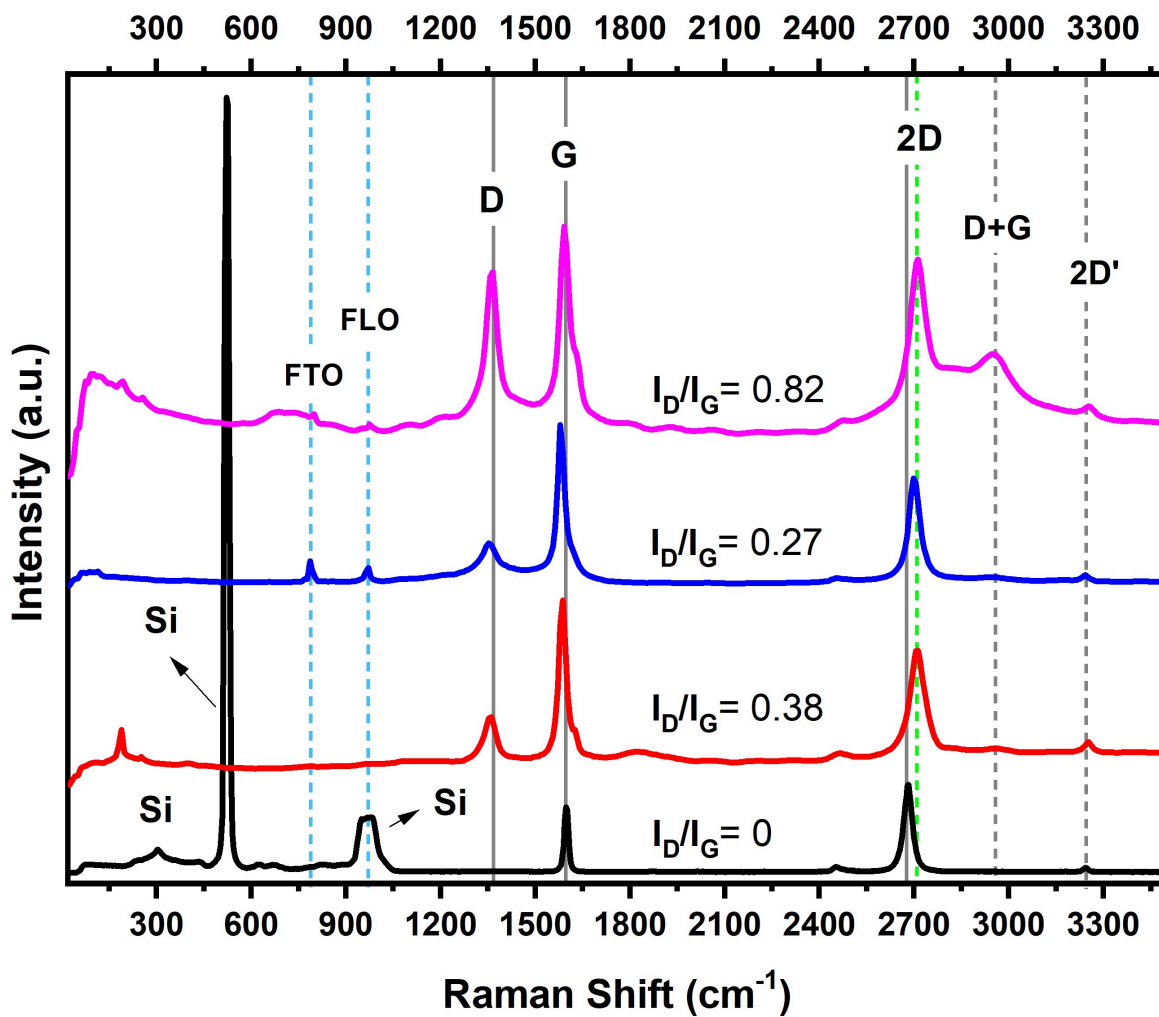Table 4.6: Synthesized graphene data for Attempt 5
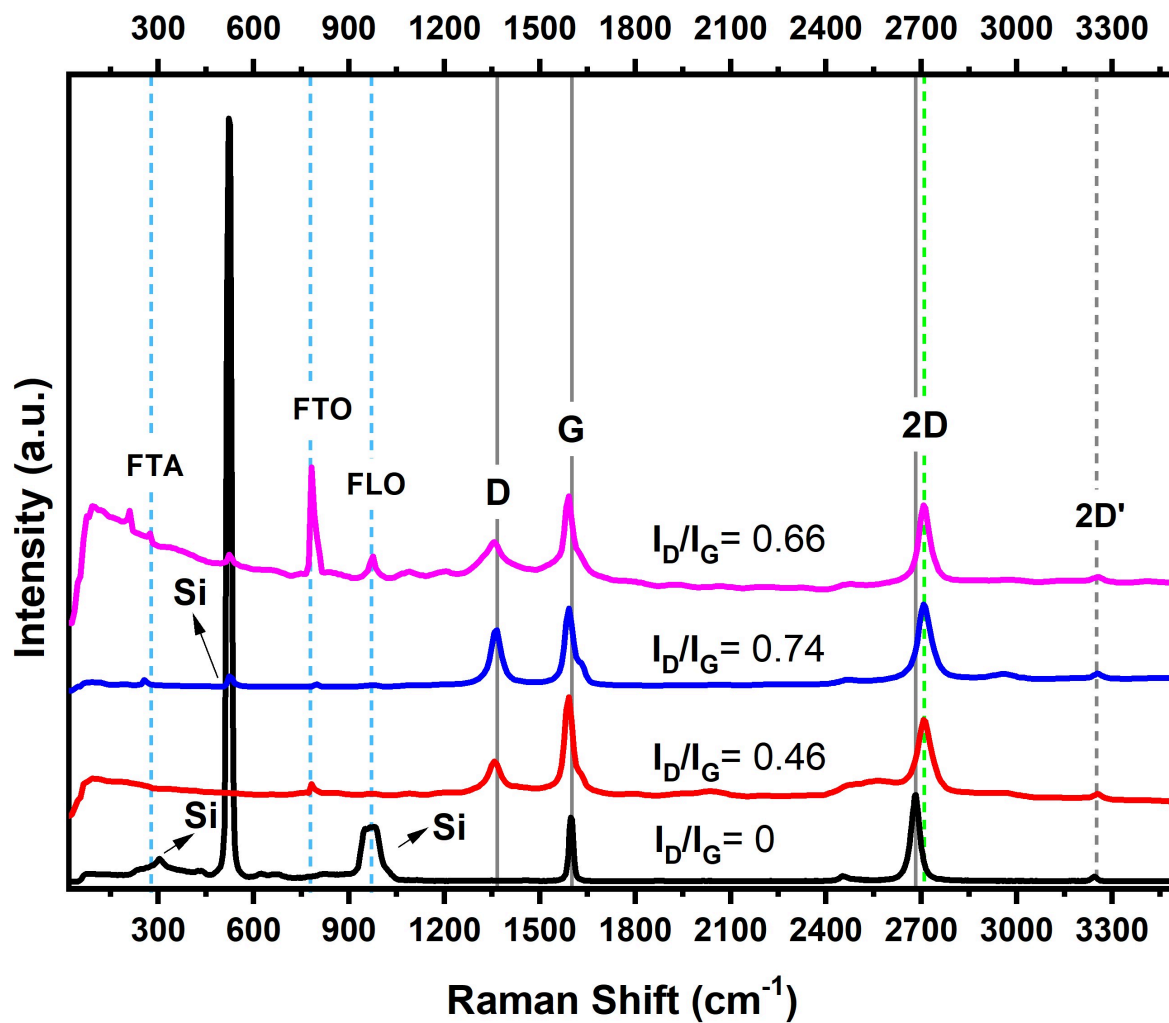
Figure 4.12: **Raman spectra of attempt 4 α-SiC after CVD vs Graphene over a Si substrate (black).** The presence of graphene from Size 1 (red), Size 2 (blue), and Size 3 (purple) SiC is confirmed from the arising of D, G, and 2D bands. The corresponding level of defects for graphene is given by the I_D/I_G ratio.
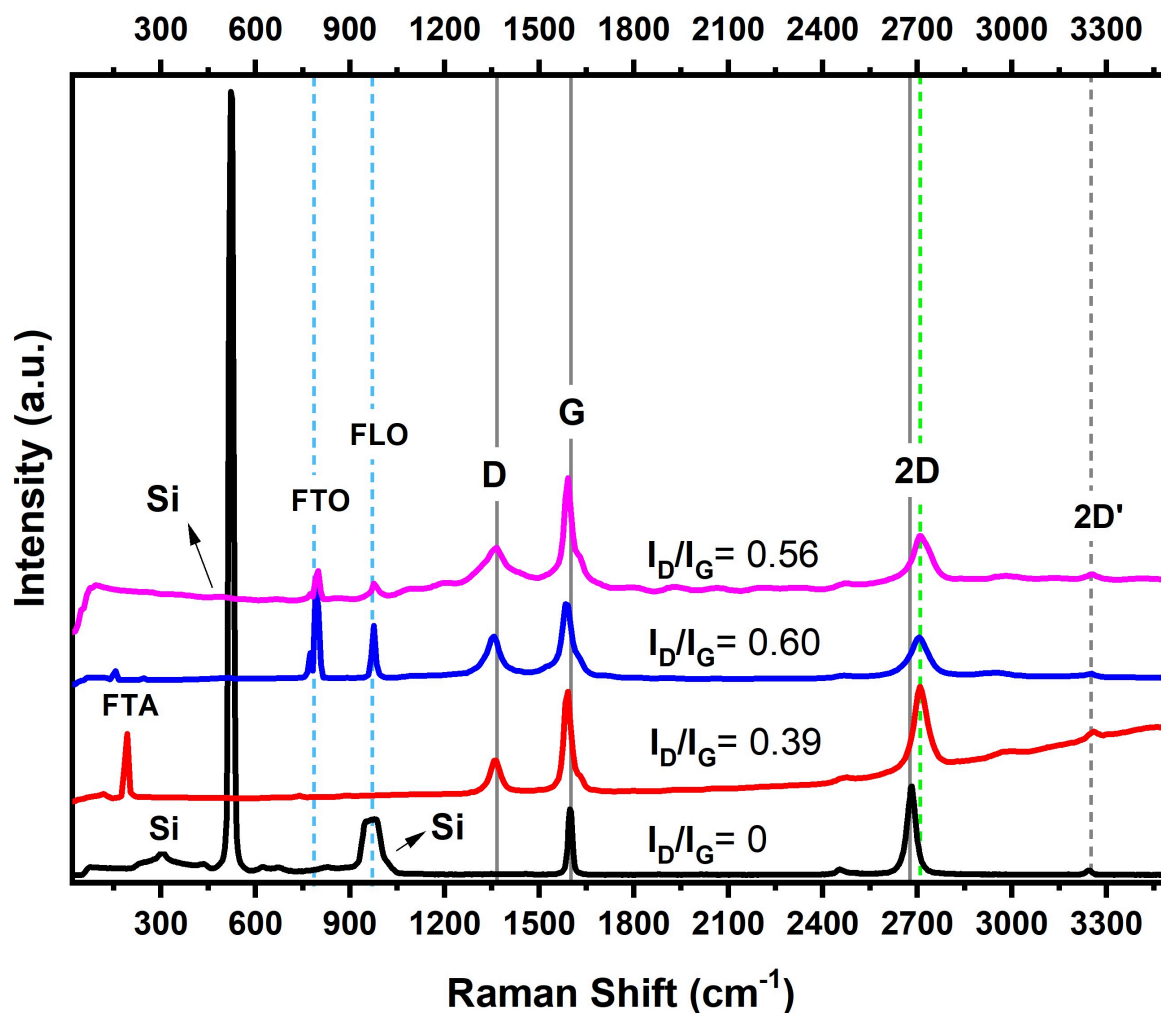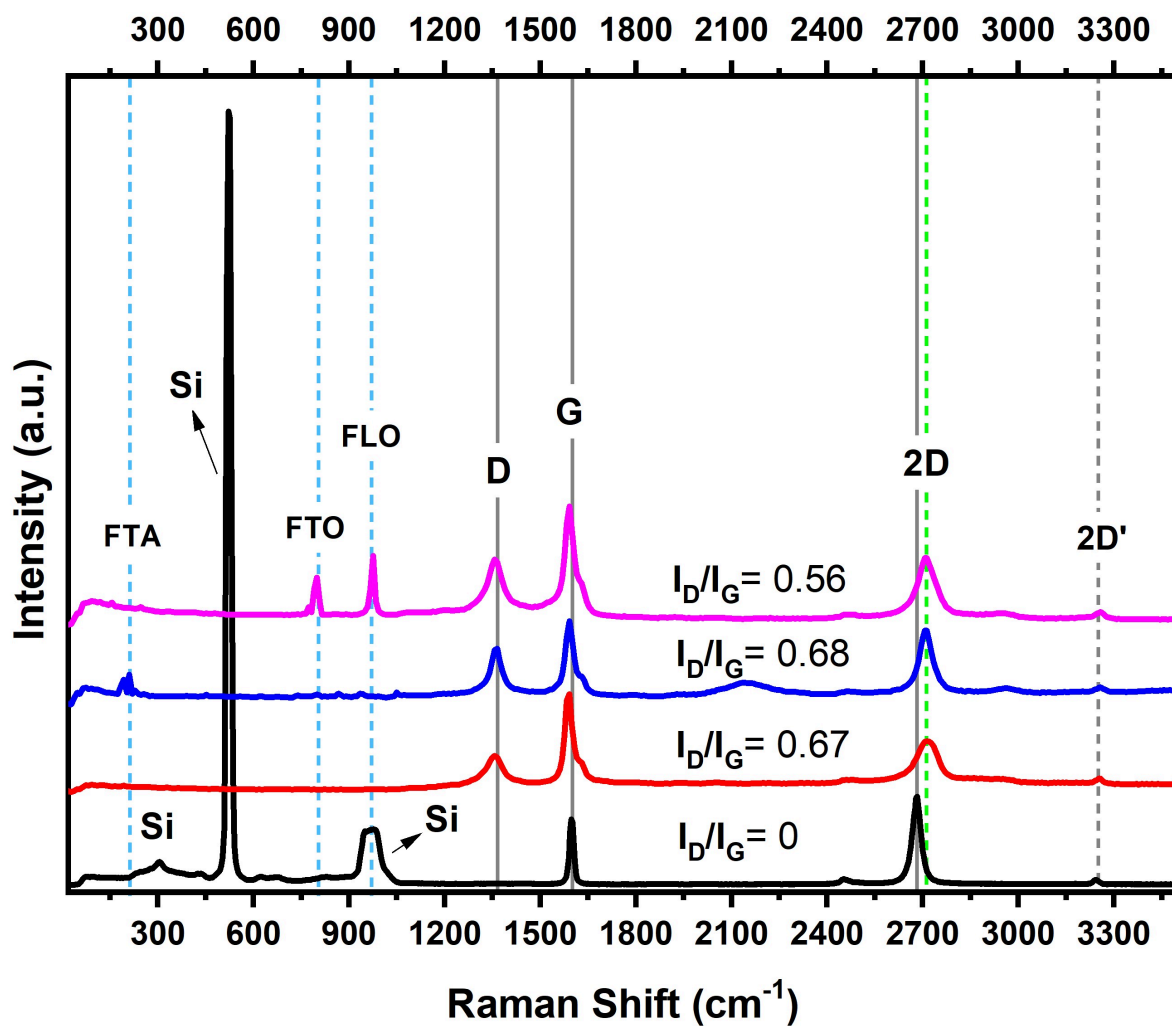
Figure 4.13:   **Raman spectra of attempt 5 α-SiC after CVD vs Graphene over a Si substrate (black).** The presence of graphene from Size 1 (red), Size 2 (blue), and Size 3 (purple) SiC is confirmed from the arising of D, G, and 2D bands. The corresponding level of defects for graphene is given by the I_D/I_G ratio.

We have verified the formation of few-layer graphene with a moderate level of defects, which is due to the poor crystalline nature of our SiC substrate[135]. Furthermore, this can explain the values of FWHM between 50 cm^{-1} and $\sim$ 80 cm^{-1} obtained for each graphene spectra, which indicates the presence of multi-layer graphene (5-7 layers) and substrate-attached stacks[136]. For the case of FWHM around 40 cm^{-1}, it is due to the presence of attached mono-layers and few-layer graphene[136]. From all these results, we can ensure the reproducibility of the experiment done with Ar at 1000 °C. In general, from the characterization of the 5 attempts, we can also observe a very small shoulder arising from the G peak, which is related to the D' peak. This peak is produced by a single phonon intravalley scattering process in graphene BZ occurring from the presence of moderate amount of defects[137].

The existence of remaining SiC Raman modes in some graphene spectra can be due to the presence of the SiC substrate from the epitaxial growth of graphene (EG). It commonly happens when the stacking of SiC terminates in a Si polar face.[76, 135]. However, it has been reported that this may be also possible due to a SiC stacking terminated in a C-face[136]. Moreover, the random behavior of increasing and decreasing of the I_D/I_G, independently of the grain size, could be due to the non-crystalline nature of the SiC grains used, as well as the attachment of oxygen functional groups in the synthesized graphene.

Even though in most cases graphene is not uniformly distributed in the α-SiC surface, it is used to grow at specific points in the borders and non-flat SiC grain areas (e.g. rough zones). In Figure 4.14 we can observe a compilation of optical images of the zones where the graphene Raman signals were taken. As it is noticeable, these zones are characterized for having an obscure rough surface, which in most cases is localized in the edges of SiC grains, as seen in Figure 4.14 (h), (j), (k), (e), and (l). Also, graphene was detected among the wrinkles and grooves of SiC seen in Figure 4.14 (a), (b), (c), (d), (f), and (i), as well as in some random spots as seen in Figure 4.14 (g). These images have left us a small clue of the favorable zones for the growth of graphene, however, it is not enough to assess this fact. For this reason, a Raman mapping of a SiC grain after CVD has been done. The results are shown in the next subsection.
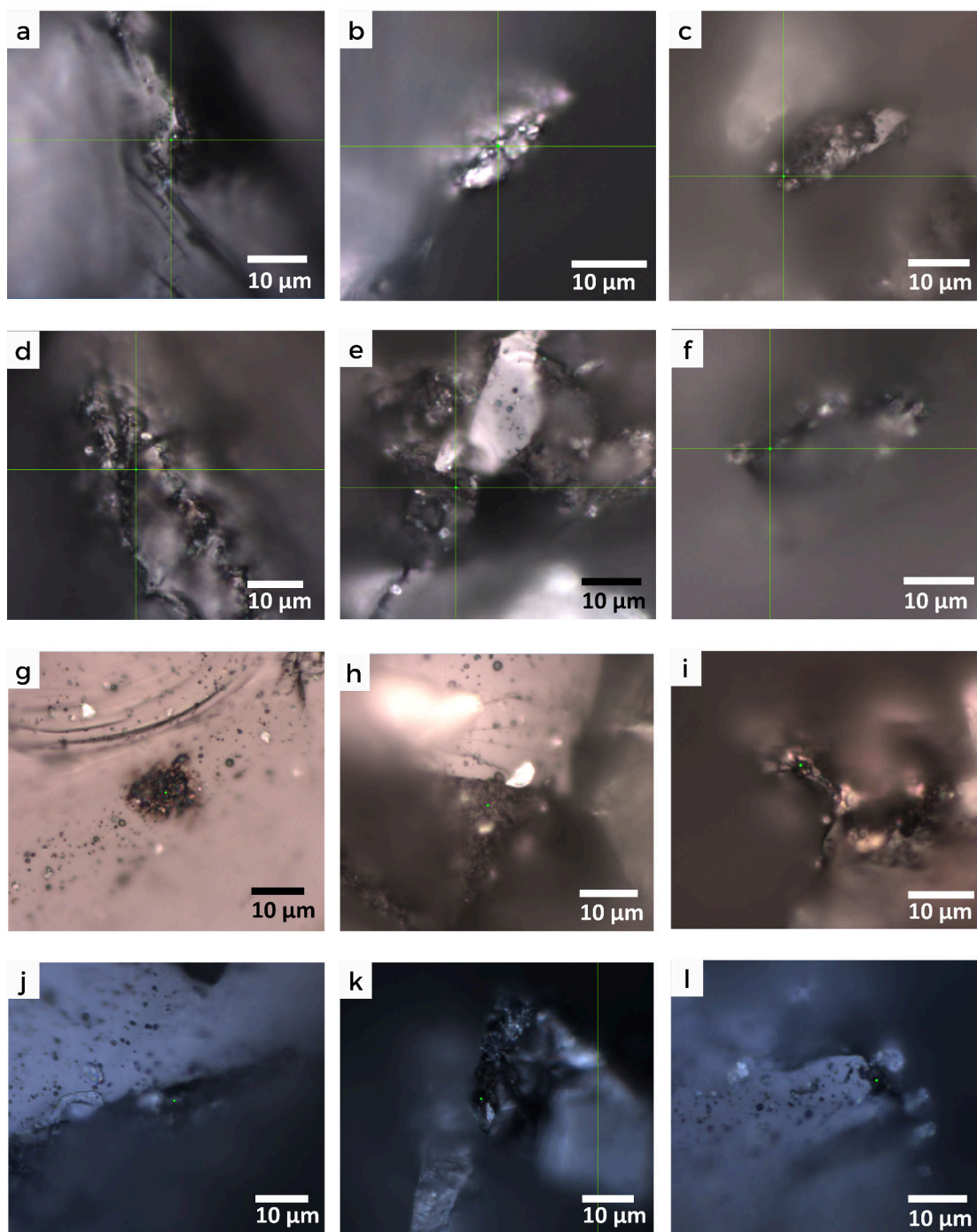
Figure 4.14:   **Optical images of graphene rich zones** from (a), (d), (g), (j) Size 1, (b), (e), (h), (k) Size 2, and (c), (f), (i), (l) Size 3 α-SiC.

4.2.2 Raman Mapping

The Raman mapping of Size 1 SiC grain after CVD is seen in Figure 4.15. The colored areas in yellow, green, and orange, represent the presence of (a) D, (b) G, and (c) 2D bands of graphene, which varies in intensity depending on its contribution. As said before in Section 4.2.1, graphene does not grow uniformly in the same area, in contrast, the intensities are randomly distributed in different spots of the edge. Such random flake growth behavior is a common sign of graphene grown on an α-SiC stacking terminated in a C face[138]. Additionally, the surface morphology of the substrate also affects the growth of the graphene layer[138].

The level of disorder in these graphene flakes is inferred from the arising of the D band, which shows a high intensity at the center of the graphene edge, but a small intensity at the sides. The G and 2D band intensities show up mostly at the center and the right side of the α-SiC grain, with an additional higher contribution of the 2D band in a top-right second spot. The contribution of the D band at this second spot is very low in comparison with that of the 2D, which suggests the presence of low defective graphene. It is noticeable that graphene flakes are all growing in the rough edges of the flake, with a very small contribution of it growing in a groove of the grain. This can be easily seen in the superposed images of the mapping and the optical image of the grain shown in Figure 4.16.

Furthermore, a mean Raman spectrum of graphene from the resultant mapping is shown in Figure 4.17. Here, we can observe the prominent peaks of D, G, and 2D bands, suggesting a high disorder of graphene (I_D/I_G=0.874) grown at the edge of Size 1 α-SiC grain. Also, background noise is detected as a result of the irregular morphology of the SiC grain, which did not allow to focus the sample and do the proper measure of the spectra.
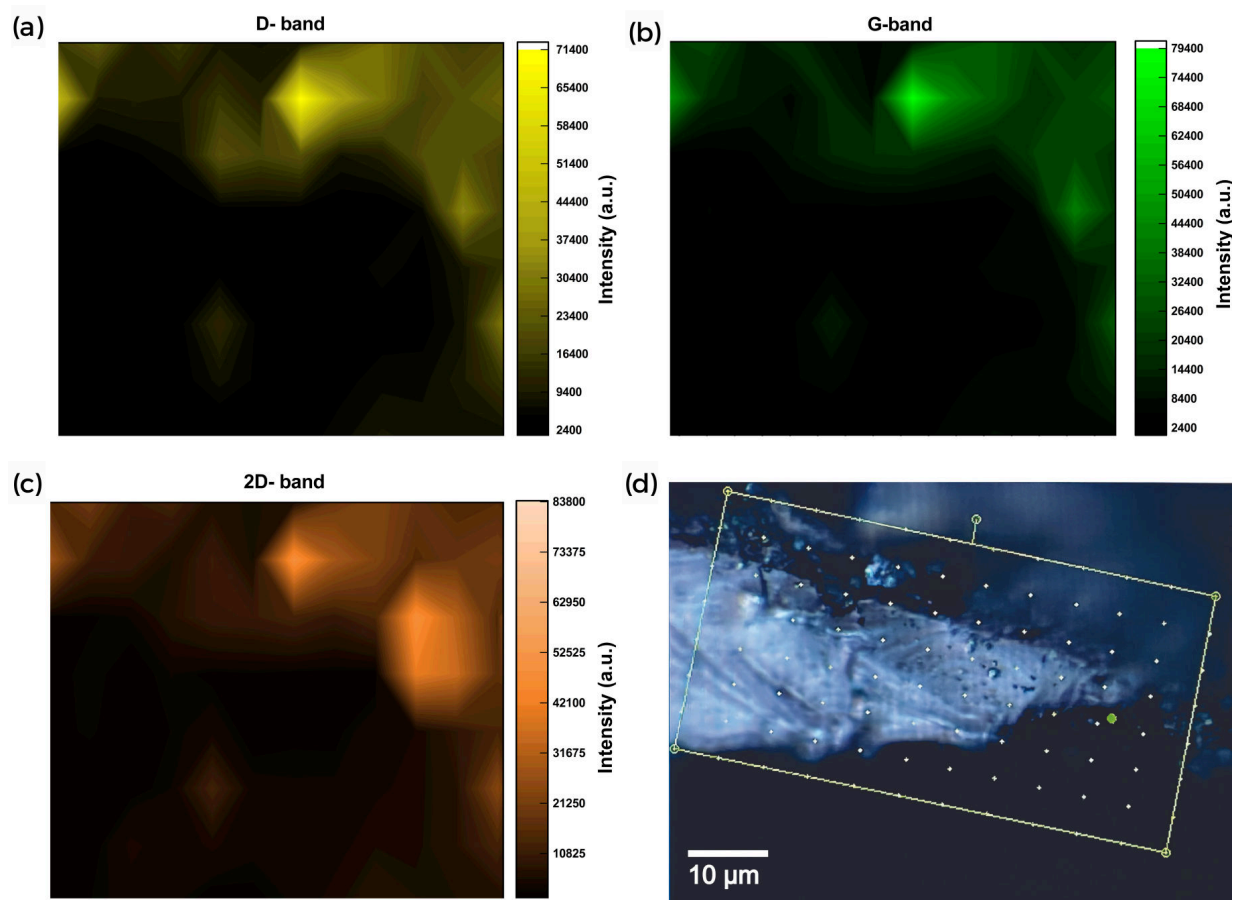
Figure 4.15:   **Raman mapping of Size 1 SiC grain after CVD**. The mapped area (d) is the same as Figure 3.8. This mapping shows the location of graphene grown in SiC and its corresponding intensity for (a) D band, (b) G band, and (c) 2D band.
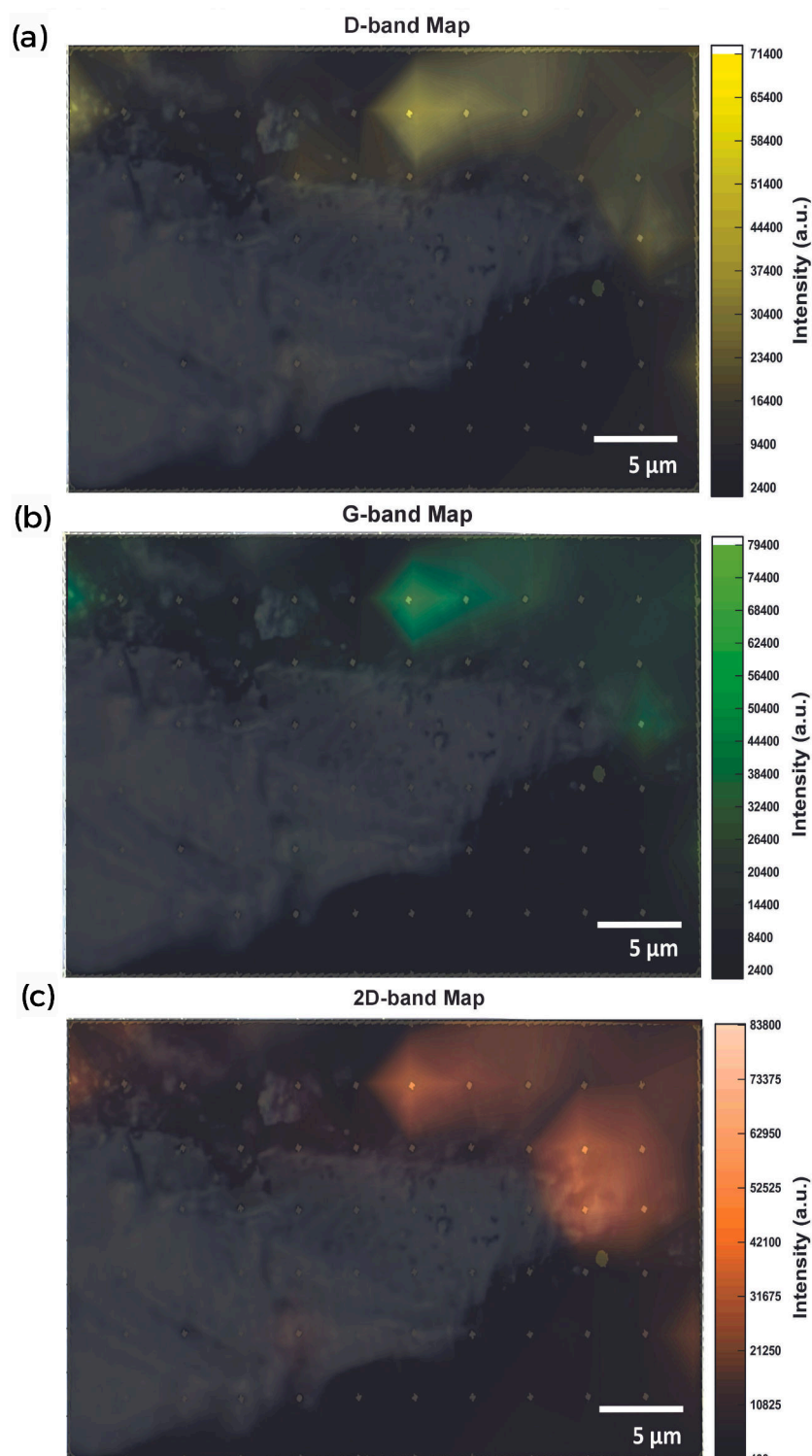
Figure 4.16: **Raman mapping of Size 1 SiC grain after CVD** from area shown in Figure 4.15 (d). This superposition shows the location of graphene grown in SiC and its corresponding intensity for (a) D band, (b) G band, and (c) 2D band.
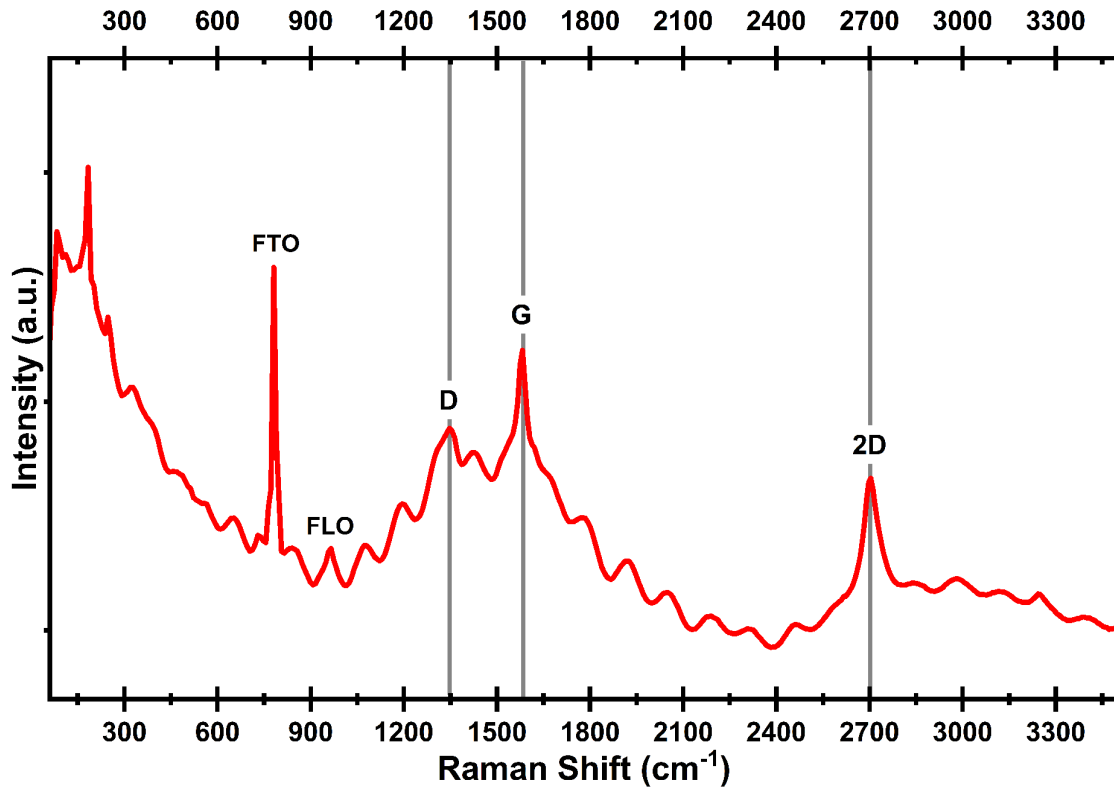
Figure 4.17: **Raman mean spectra of Size 1 SiC grain after CVD** from area shown in Figure 4.15 (d).

4.3   Synthesized SiC samples with Ar + H_2 and Ar + CH_4 +H_2

In this section, the results for the simulated synthesis of graphene under a hydrogen, argon, and methane-rich environment are discussed. The new parameters considered in both cases are a higher time of synthesis t= 230 mins, a temperature of T= 1000 °C (1273 K), a pressure of P= 0.12 Torr, and different flux rates for H_2 (0.08 L/min), Ar (0.5 - 0.3 L/min) and CH_4 (0.01 L/min) gasses.

4.3.1 Synthesized SiC samples with Ar + H_2

In this section, the results obtained from the synthesis of graphene at CVD using Ar and H_2 gasses are discussed. In Figure 4.18 and Figure 4.19 we can observe the Raman spectra of Size 1, (a) Size 2, and (b) Size 3 graphene samples measured at different zones. It is evident the presence of a highly disordered graphene from the intensity of the D band in all samples. Here, a prominent shoulder attached to the G band, corresponding to the D' band (pointed in sky blue arrows), is seen with small intensity, as well as the presence of the D+G disorder band seen around 2900 cm^{-1}. Additionally to this, we can observe the presence of very small peaks between D and G bands, pointed with green arrows, which corresponds to the alteration of the common hybridization of graphene due to the presence of hydrogenated carbon atoms[139]. This occurred as a result of the interaction of graphene with the molecular hydrogen gas used for the CVD process.
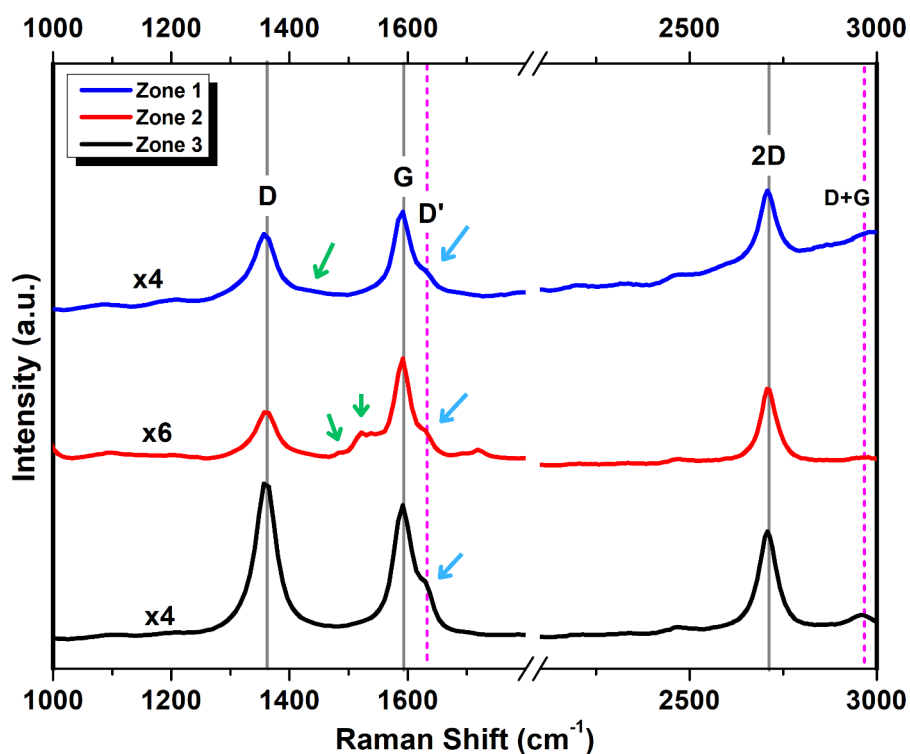
Figure 4.18: **Raman spectra of synthesized graphene in an Ar+H_2 environment.** Graphene grown on Size 1 SiC spectra measured in different zones is seen.
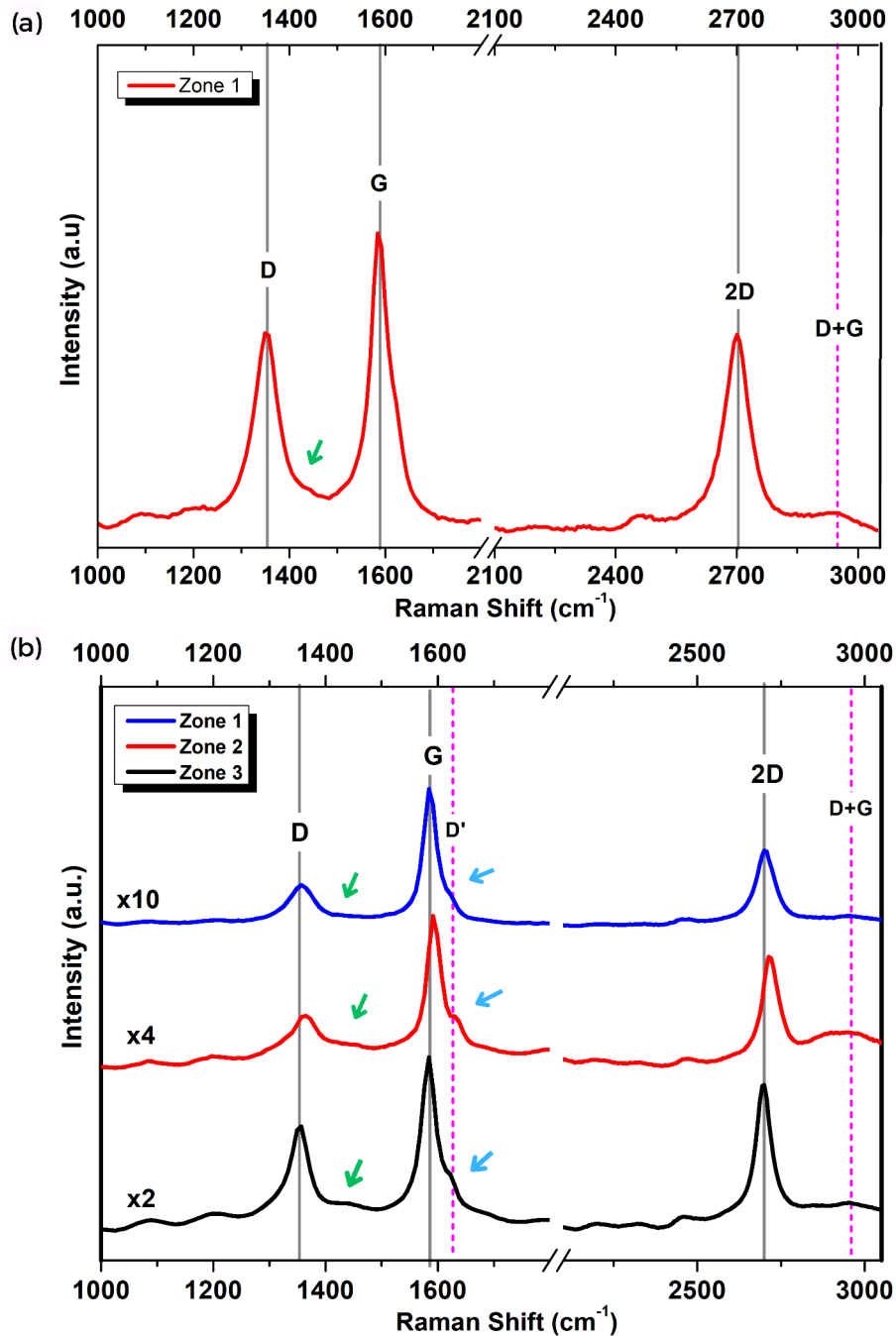
Figure 4.19: **Raman spectra of synthesized graphene in an Ar+H_2 environment.** Graphene grown in (a) Size 2 and (b) Size 3 SiC spectra measured in different zones is seen. The presence of hydrogenated carbon is noticed from the appearance of small peaks between the D and G bands, and the arising of the D' band.

4.3.2 Synthesized SiC samples with Ar + CH_4 + H_2

For this case, it is seen that the level of defects in the D band has increased significantly from the presence of an amorphous D band and a very broad 2D band, which is seen in Figure 4.20. In this figure, the Raman spectra of Size 1, Size 2, and Size 3 synthesized graphene in an Ar+ CH_4 + H_2 gas environment are shown. At first sight, we can notice the presence of intermediate shoulders arising between the D and G bands. In comparison with Figure 4.18, these Raman spectra show peaks of higher intensity (pointed with green arrows) and a higher deformation of G and D bands. This behavior is the result of the interaction between carbon atoms from graphene and the hydrogen atoms from H_2 and CH_4 that originates carbon bond vibrational coupling deviations[139] in the band structure of graphene. Both molecules have produced modifications in the vibrational normal modes of graphene[140], reflected in the D and G bands.
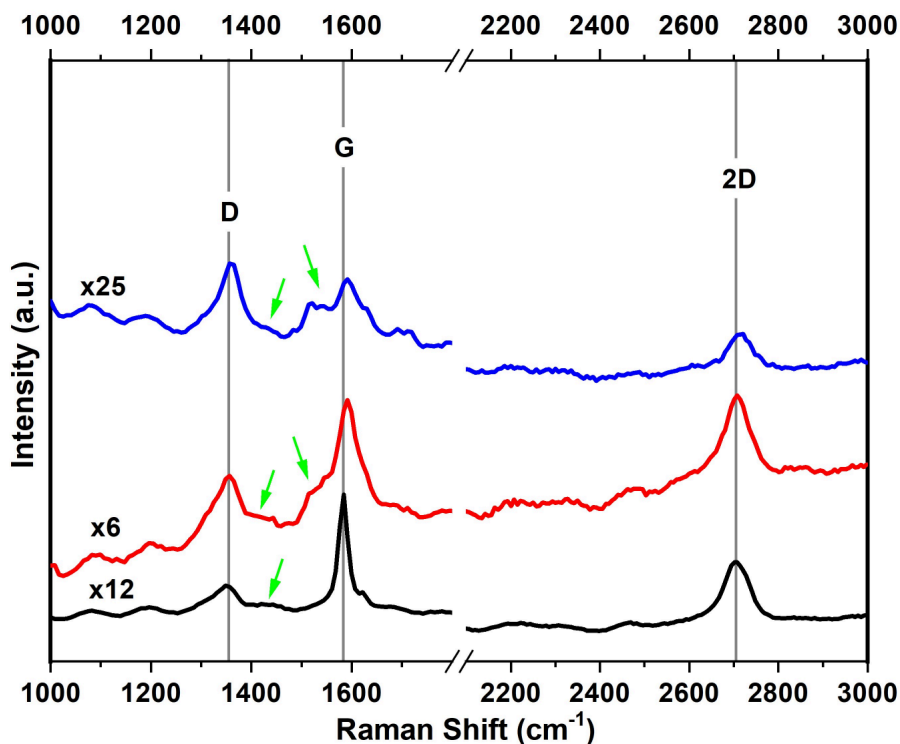
Figure 4.20: **Raman spectra of synthesized graphene in Ar+H_2+CH_4 environment.** Graphene grown in Size 1 (blue), Size 2 (red), and Size 3 (black) SiC grains. The presence of hydrogenated carbon is noticed from the appearance of intermediate peaks between the D and G bands.

From the results given for the synthesis of graphene at different time, temperature, pressure, flow rate, and gasses, it was necessary to analyze how these variables affect the growth of graphene. For this reason, an additional attempt was done with the same time of synthesis used in this section t= 230 mins and an atmospheric pressure of P= 30.18 inHg (766.5 Torr). In Figure 4.21, we can observe an amorphous D band arising as a signal of a defective graphene surface, which gives us a I_D/I_G ratio of 0.58, 0.33, and 0.62 for Size 1, Size 2, and Size 3 graphene samples respectively. This tell us that the most defective graphene was formed over the SiC grain of Size 1, while the less defective graphene was formed in the Size 2 SiC. Also, a small blueshift of the 2D band is noticed, showing a peak position of 2707.65 cm^{-1} for Size 1 and Size 2 graphene, and a non-shifted Size 3 graphene (2687.44 cm^{-1}). On one hand, these results do not show significant changes compared with the results obtained in Section 4.2.1. Then, the time of synthesis is not considered a variable when growing graphene in an Ar-rich environment. However, the difference is seen at first sight when comparing these results with the ones obtained in Subsection 4.3.1 and Subsection 4.3.2. Here, the gasses used are considered as an important variable to take into account.

|	**2D-band Peak position** (cm^{-1})	I_D/I_G
Size 1	2707.65	0.62
Size 2	2707.65	0.33
Size 3	2687.44	0.58

Table 4.7: Synthesized graphene data for Attempt 8
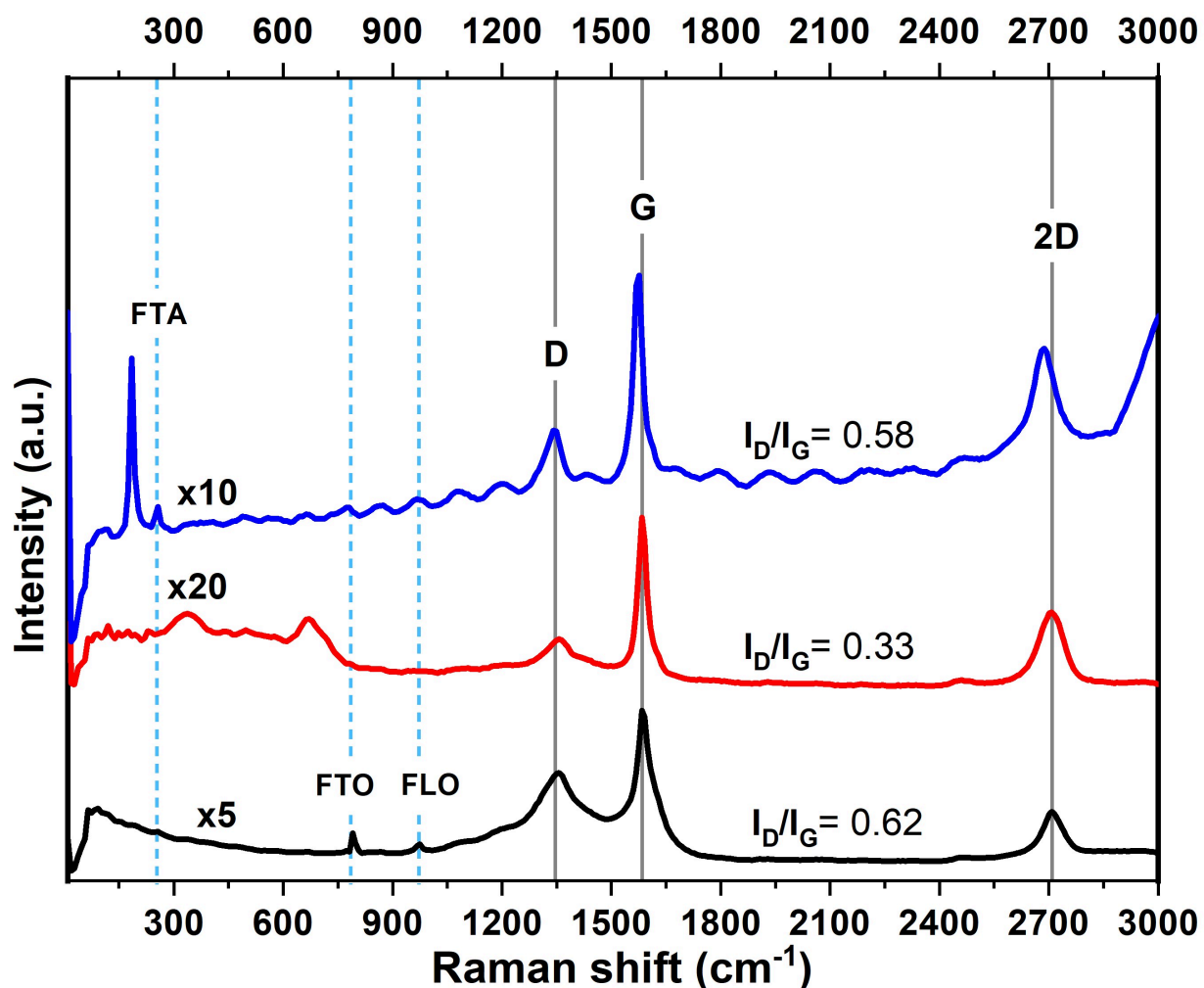
Figure 4.21: **Raman spectra of synthesized graphene in an Ar environment.** Graphene grown in Size 1 (black), Size 2 (red), and Size 3 (blue) SiC grains. The parameters used in this synthesis are t= 230 mins and P= 766.5 Torr.

4.4   Astrophysical Implications

From the astrophysical point of view, the results obtained in the previous sections give an interesting interpretation of the favorable conditions necessary for graphene growth in carbon-rich interstellar environments. This is supported by the results found by Giri et al. (2021) where he reports the presence of nanoscale mono-layer and graphene morphologies in QUE 94366 and Allende CV3-type carbonaceous chondrites[10].

From further investigation, it was found that SiC grains are one of the most rich carbon compounds existing in the vicinity of AGB stars, which is also a component of some carbon meteorites. Therefore, this investigation was carried out from the knowledge of the existence of SiC grains found in Allende Curious Marie calcium–aluminium-rich inclusion (CAI)[141] and, Murray and Murchison chondrites[94] which tell us that this presolar grain can survive to the high temperature of parent body formation of meteorites ($\geq$ 900 °C) for several years[141]. This is possible due to the encapsulation of SiC grains within refractory minerals in meteorites, such as CAIs. However, this implies that everything inside CAIs will not suffer chemical changes due to its exposure to high temperatures. Taking this into account, the only possibility for graphene to be found within these CAIs is that graphene was grown before its incorporation into carbonaceous chondrites or, that the growth of graphene was condensed from a carbon-rich gas during the formation of CAIs in the close proximities to the proto-Sun as stated by Giri et al.[10]. From our results, we can assess that both possibilities are plausible from the exposure of SiC grains to temperatures oscillating 1000° C (1200 K). This is enough to get a graphene-rich surface, which environmental conditions are satisfied by the circumstellar envelope of AGB carbon-rich stars[107]. This is also supported by Merino et al. (2014), who stated that SiC grains end up covered with graphene when exposed to high temperatures between 2000-1500 K[121].

Otherwise, there exist some factors that have not been widely studied in this research. First of all, the normal SiC grain size that has been found embedded in meteorites, ranges from < 0.2 μm to 6 μm[95]. In our case, the synthesis was done over α-SiC grains ranges of 30 μm up to 700 μm. However, the main purpose of working with different grain sizes was to see how the size can affect the growth of graphene on the grain surface. As a result, the changes in the particle grain size did not show alteration in the Raman spectra, since graphene was formed in all cases. Second, the UHV condition to simulate the extraterrestrial environment was not considered in our experiments. Nevertheless, we know this variable is an important factor for simulating the real conditions in outer space.

Chapter 5

Conclusions & Outlook

The core of this thesis was to investigate the formation of graphene species in experimental extraterrestrial conditions. In order to achieve this goal, 4 important sections related the results of this project.

In Section 4.1, the polytype identification of the SiC samples was done by using XRD and SEM characterization methods. The polytype found for the three different sizes of SiC (Size 1, Size 2, Size 3) was 6H-SiC (α-SiC) also called Moissanite. Furthermore, the grain size measured from the SEM images of the samples gave us mean values of 340.91 μm, 143.45 μm, and 70.43 μm for Size 1, Size 2, and Size 3 SiC respectively, values that were not in accordance with the ones given by ANSI[127].

For section 4.2 covered the five synthesis attempts of graphene over the α-SiC samples in an Ar environment characterized via Raman spectroscopy. These attempts were done using the same parameters of synthetization time (190 mins), gasses (Ar), flow rate (0.3 L/min), and pressure (766.5 Torr). This assessed the reproducibility of the experiment, which was visible from almost the same peak positions. In general, the synthesized graphene in the three sizes showed a blueshift in their 2D band peak < 30 cm^{-1} and a FWHM between 30 cm^{-1} and 80 cm^{-1}, which clearly showed the growth of few-layer and multi-layer graphene. Also, the level of defects in these samples was measured from the I_D/I_G ratio, which showed values between 0.20 and 0.82 corresponding to a moderate level of defects caused by the double resonant phonon process responsible for the arising of the D disorder band[63]. Moreover, a Raman mapping was done in order to assess that the favorable zones for the growth of graphene are mostly the edges of the α-SiC grains and their grooves.

In section 4.3, the experiment was reproduced using different gasses (Ar, H_2, CH_4), synthesis time (230 mins), and pressure (0.12 Torr), which showed significant differences in the Raman spectra of graphene. For the case of synthesized SiC with Ar and H_2, it was evident the presence of a highly disordered graphene

from the shoulder attached to the G band of all samples, corresponding to a D' band. Additionally, the presence of very small peaks between the D and G bands is seen, which corresponds to the alteration of the common hybridization of graphene due to the presence of hydrogenated carbon atoms[139]. Finally, for the case of the addition of H_2, CH_4 gasses, we notice the presence of an amorphous D band and a broad 2D band as a result of the interaction between carbon atoms from graphene and the hydrogen atoms from H_2 and CH_4 that originates carbon bond vibrational coupling deviations[139].

Finally, in Section 4.4 the astrophysical implications that the results have over previous research done conclude that graphene can be formed from the exposure of SiC grains to temperatures oscillating 1000° C (1200 K). This is enough to get a graphene-rich surface, in which environmental conditions are satisfied by the circumstellar envelope of AGB carbon-rich stars. This is also supported by Merino et al. (2014), who stated that SiC grains end up covered with graphene when exposed to high temperatures between 2000-1500 K. Furthermore, the grain size is not a determining factor for growing graphene, but the gasses flowing around become an extremely relevant factor to be considered in order to explain the formation of graphene in the outer space. In this case, the best suitable interstellar environment for growing graphene is in the presence of argon gas, which gas is the result of the s-process in AGB stars[142].

All these interesting results impulse us to search for more astrophysical clues that could help to mainly reproduce the conditions of the extraterrestrial medium that could have helped the growth of graphene. Reproducing these experiments working on a UHV environment to simulate the real extraterrestrial medium will give us more realistic results on the graphene synthesis time, and the possible consequences caused by the change of pressure in the material. Moreover, more attempts at graphene synthesis in hydrogen and methane environments adding time as a variable must be done in order to get more conclusive results. Finally, further experimental research must be done related to the conditions that caused the graphene to be found embedded inside refractory inclusions in chondrites. There exist many possibilities to think about how it could have happened, for this reason, the analysis of the conditions (e.g. gasses, particles) present in meteorite formation zones is of outmost importance.

Appendix A

Weight measurements of 6H-SiC before and after CVD

	Boat (g)	SiC + boat		Difference (g)
		After CVD (g)	Before CVD (g)	
Size 1	1.9233	2.1742	2.1726	- 0.0016
Size 2	2.0121	2.2414	2.2410	- 0.0004
Size 3	2.0207	2.2668	2.2666	- 0.0002

Table A.1: Attempt 1 with Ar gas at 120 mins

	Boat (g)	SiC + boat		Difference (g)
		After CVD (g)	Before CVD (g)	
Size 1	1.9229	2.0633	2.0632	- 0.0001
Size 2	2.0117	2.1376	2.1374	- 0.0004
Size 3	2.0205	2.1922	2.1922	- 0.0000

Table A.2: Attempt 2 with Ar gas at 120 mins

	Boat (g)	SiC + boat		Difference (g)
		After CVD (g)	Before CVD (g)	
Size 1	1.9230	2.1206	2.1205	- 0.0001
Size 2	2.0204	2.1937	2.1933	- 0.0004
Size 3	2.0119	2.1931	2.1933	- 0.0002

Table A.3: Attempt 3 with Ar gas at 120 mins

	Boat (g)	SiC + boat		Difference (g)
		After CVD (g)	Before CVD (g)	
Size 1	2.0205	2.1473	2.1465	- 0.0008
Size 2	2.0123	2.1297	2.1295	- 0.0002
Size 3	1.9230	2.0240	2.0240	- 0.0000

Table A.4: Attempt 4 with Ar gas at 120 mins

	Boat (g)	SiC + boat		Difference (g)
		After CVD (g)	Before CVD (g)	
Size 1	2.0215	2.2622	2.2617	- 0.0005
Size 2	1.9304	2.1126	2.1067	- 0.0059
Size 3	1.9279	2.1460	2.1418	- 0.0042

Table A.5: Attempt 5 with Ar gas at 120 mins

	Boat (g)	SiC + boat		Difference (g)
		After CVD (g)	Before CVD (g)	
Size 1	1.9248	2.1105	2.1107	+ 0.0002
Size 2	2.0202	2.1720	2.1719	- 0.0001
Size 3	1.9234	2.1014	2.1013	- 0.0001

Table A.6: Attempt 1 with Ar gas at 230 mins

	Boat (g)	SiC + boat		Difference (g)
		After CVD (g)	Before CVD (g)	
Size 1	2.0180	2.1436	2.1435	- 0.0001
Size 2	2.0812	2.2127	2.2123	- 0.0004
Size 3	1.9659	2.1431	2.1424	- 0.0007

Table A.7: Attempt 1 with Ar + H_2 gasses at 230 mins

Appendix B

CVD parameters configuration

Temperature (°C)		Time (mins)	
C1	0	t_1	10
C2	100	t_2	10
C3	200	t_3	10
C4	300	t_4	10
C5	500	t_5	10
C6	700	t_6	10
C7	800	t_7	10
C8	900	t_8	20
C9	1000	t_9	30
C10	1000	t_{10}	-121

Table B.1: CVD parameters for attempts 1-5 with Ar gas at 120 mins

Temperature (°C)		Time (mins)	
C1	0	t_1	10
C2	100	t_2	10
C3	200	t_3	20
C4	300	t_4	20
C5	400	t_5	20
C6	500	t_6	20
C7	600	t_7	20
C8	700	t_8	20
C9	800	t_9	25
C10	900	t_{10}	25
C11	1000	t_{11}	30
C12	1000	t_{12}	-121

Table B.2: CVD parameters for attempt 1 with Ar gas at 230 mins

Temperature (°C)		Time (mins)	
C1	0	t_1	20
C2	100	t_2	20
C3	200	t_3	20
C4	300	t_4	20
C5	400	t_5	20
C6	500	t_6	20
C7	600	t_7	20
C8	700	t_8	20
C9	800	t_9	20
C10	900	t_{10}	20
C11	1000	t_{11}	30
C12	1000	t_{12}	-121

Table B.3: CVD parameters for attempt 1 with Ar + H_2 and Ar + H_2 + CH_4 gasses at 230 mins.

Bibliography

[1] Chang, H.; Wu, H. Graphene-based nanomaterials: Synthesis, properties, and optical and optoelectronic applications. *Advanced Functional Materials* **2013**, *23*, 1984–1997.

[2] Zhang, Y.; Zhang, L.; Zhou, C. Review of chemical vapor deposition of graphene and related applications. *Accounts of chemical research* **2013**, *46*, 2329–2339.

[3] Martinez-Gordillo, R.; Varvenne, C.; Amara, H.; Bichara, C. Ni 2 C surface carbide to catalyze low-temperature graphene growth. *Physical Review B* **2018**, *97*.

[4] Wang, J.-b.; Ren, Z.; Hou, Y.; Yan, X.-l.; Liu, P.-z.; Zhang, H.; Zhang, H.-x.; Guo, J.-j. A review of graphene synthesisatlow temperatures by CVD methods. *New Carbon Materials* **2020**, *35*, 193–208.

[5] Phiri, J.; Gane, P.; Maloney, T. C. General overview of graphene: Production, properties and application in polymer composites. *Materials Science and Engineering: B* **2017**, *215*, 9–28.

[6] Fuchs, J.-N.; Goerbig, M. O. Introduction to the physical properties of graphene. *Lecture notes* **2008**, *10*, 11–12.

[7] Mishra, N.; Boeckl, J.; Motta, N.; Iacopi, F. Graphene growth on silicon carbide: A review. *physica status solidi (a)* **2016**, *213*, 2277–2289.

[8] Cooper, D. R.; D'Anjou, B.; Ghattamaneni, N.; Harack, B.; Hilke, M.; Horth, A.; Majlis, N.; Massicotte, M.; Vandsburger, L.; Whiteway, E.; Yu, V. Experimental review of graphene. 2011.

[9] Van Bommel, A.; Crombeen, J.; Van Tooren, A. LEED and Auger electron observations of the SiC(0001) surface. *Surface Science* **1975**, *48*, 463–472.

[10] Giri, C.; Steele, A.; Fries, M. Evidence for protosolar graphene in Allende and QUE 94366 CV3 meteorites. *Planetary and Space Science* **2021**, *203*, 105267.

[11] Chen, X.; Li, A.; Zhang, K. On graphene in the interstellar medium. *The Astrophysical Journal* **2017**, *850*, 104.

[12] Jacobberger, R. M.; Arnold, M. S. Graphene Growth Dynamics on Epitaxial Copper Thin Films. *Chemistry of Materials* **2013**, *25*, 871–877.

[13] Hicks, J.; Shepperd, K.; Wang, F.; Conrad, E. H. The structure of graphene grown on the SiC (0,0,0,) surface. *Journal of Physics D: Applied Physics* **2012**, *45*, 154002.

[14] Real, M. A.; Lass, E. A.; Liu, F.-H.; Shen, T.; Jones, G. R.; Soons, J. A.; Newell, D. B.; Davydov, A. V.; Elmquist, R. E. Graphene epitaxial growth on SiC (0001) for resistance standards. *IEEE Transactions on Instrumentation and Measurement* **2013**, *62*, 1454–1460.

[15] Hoppe, P.; Zinner, E. Presolar dust grains from meteorites and their stellar sources. *Journal of Geophysical Research: Space Physics* **2000**, *105*, 10371–10385.

[16] Daulton, T. L. Nanodiamonds in the Cosmos. *Synthesis, properties and applications of ultra-nanocrystalline diamond* **2005**, 49–62.

[17] Straniero, O.; Abia, C.; Domínguez, I. The carbon star mystery: 40 years later: Theory and observations. *The European Physical Journal A* **2023**, *59*, 17.

[18] Elsila, J. E.; Aponte, J. C.; Blackmond, D. G.; Burton, A. S.; Dworkin, J. P.; Glavin, D. P. Meteoritic amino acids: Diversity in compositions reflects parent body histories. *ACS Central Science* **2016**, *2*, 370–379.

[19] Sears, D. W. *The origin of chondrules and chondrites*; Cambridge University Press, 2004; Vol. 3.

[20] Scott, E.; Krot, A. Chondrites and their components. *Treatise on geochemistry* **2003**, *1*, 711.

[21] Shu, F. H.; Shang, H.; Lee, T. Toward an astrophysical theory of chondrites. *Science* **1996**, *271*, 1545–1552.

[22] Scott, E. R. Chondrites and the protoplanetary disk. *Annu. Rev. Earth Planet. Sci.* **2007**, *35*, 577–620.

[23] Shanos, G. Published by the Astronomical League A Beginner's Guide to Collecting Meteorites Asteroid Van Zandt Imaging Distant Galaxy Clusters Virginia Beach Boardwalk Astronomers From Around the League: League Officer Nominations Winning Journalism Award Essays. **2016**,

[24] Kallemeyn, G. W.; Wasson, J. T. The compositional classification of chondrites—I. The carbonaceous chondrite groups. *Geochimica et Cosmochimica Acta* **1981**, *45*, 1217–1230.

[25] Sohl, F.; Spohn, T. In *Encyclopedia of Astrobiology*; Gargaud, M., Amils, R., Quintanilla, J. C., Cleaves, H. J. J., Irvine, W. M., Pinti, D. L., Viso, M., Eds.; Springer Berlin Heidelberg: Berlin, Heidelberg, 2011; pp 246–246.

[26] McSween Jr, H. Y. Are carbonaceous chondrites primitive or processed? A review. *Reviews of Geophysics* **1979**, *17*, 1059–1078.

[27] Bischoff, A. Aqueous alteration of carbonaceous chondrites: Evidence for preaccretionary alteration—A review. *Meteoritics & Planetary Science* **1998**, *33*, 1113–1122.

[28] Llorca, J. Organic matter in meteorites. *Int Microbiol* **2004**, *7*, 239–248.

[29] Thompson, M. A.; Telus, M.; Edwards, G. H.; Schaefer, L.; Dhaliwal, J.; Dreyer, B.; Fortney, J. J.; Kim, K. Outgassing Composition of the Murchison Meteorite: Implications for Volatile Depletion of Planetesimals and Interior-atmosphere Connections for Terrestrial Exoplanets. *The Planetary Science Journal* **2023**, *4*, 185.

[30] Schmitt-Kopplin, P.; Gabelica, Z.; Gougeon, R. D.; Fekete, A.; Kanawati, B.; Harir, M.; Gebefuegi, I.; Eckel, G.; Hertkorn, N. High molecular diversity of extraterrestrial organic matter in Murchison meteorite revealed 40 years after its fall. *Proceedings of the National Academy of Sciences* **2010**, *107*, 2763–2768.

[31] Kletetschka, G.; Kohout, T.; Wasilewski, P. J. Magnetic remanence in the Murchison meteorite. *Meteoritics & Planetary Science* **2003**, *38*, 399–405.

[32] Pizzarello, S. Chemical evolution and meteorites: an update. *Origins of Life and Evolution of the Biosphere* **2004**, *34*, 25–34.

[33] Neuland, M.; Mezger, K.; Riedo, A.; Tulej, M.; Wurz, P. The chemical composition and homogeneity of the Allende matrix. *Planetary and Space Science* **2021**, *204*, 105251.

[34] Krot, A.; Petaev, M.; Meibom, A.; Keil, K. In situ growth of Ca-rich rims around Allende dark inclusions. *Geochemistry International* **2000**, *38*, S351.

[35] Barbero, A. H.; Lopez, H. G. V.; Lopez, A. L. M.; Castaeda, J. A. C.; Laviada, D. L.; de la Cruz, K. E. C.; Laguna, V. M.; Basiuk, V. A.; Chvez, I. R.; Mendoza, A. N. Possible Relevance of the Allende Meteorite Conditions in Prebiotic Chemistry: An Insight into the Chondrules and Organic Compounds. *Advances in Biological Chemistry* **2023**, *13*, 82–99.

[36] Jones, C. L.; Brearley, A. J. Experimental aqueous alteration of the Allende meteorite under oxidizing conditions: Constraints on asteroidal alteration. *Geochimica et Cosmochimica Acta* **2006**, *70*, 1040–1058.

[37] Rubin, A. E.; Wasson, J. T. Chondrules in the Murray CM2 meteorite and compositional differences between CM-CO and ordinary chondrite chondrules. *Geochimica et Cosmochimica Acta* **1986**, *50*, 307–315.

[38] Roberta Score, E. S., Brian Mason Sample Petrographic Description of QUE 94366 meteorite. `https://curator.jsc.nasa.gov/antmet/samples/petdes.cfm?sample=QUE94366`.

[39] Dieing, T.; Hollricher, O.; Toporski, J. *Confocal Raman Microscopy*; Springer Series in Optical Sciences; Springer Berlin Heidelberg, 2011.

[40] Rao, C.; Biswas, K.; Subrahmanyam, K.; Govindaraj, A. Graphene, the new nanocarbon. *Journal of Materials Chemistry* **2009**, *19*, 2457–2469.

[41] Li, X.; Yu, J.; Wageh, S.; Al-Ghamdi, A. A.; Xie, J. Graphene in photocatalysis: a review. *Small* **2016**, *12*, 6640–6696.

[42] Raza, H. *Graphene nanoelectronics: Metrology, synthesis, properties and applications*; Springer Science & Business Media, 2012.

[43] LANDAU, L.; AKHIEZER, A.; LIFSHITZ, E. In *General Physics*; LANDAU, L., AKHIEZER, A., LIFSHITZ, E., Eds.; Pergamon: Oxford, 1967; pp 115–143.

[44] Roth, S.; Carroll, D. *Foundations of Solid State Physics: Dimensionality and Symmetry*; Wiley-VCH Verlag GmbH & Company, 2019.

[45] Misra, P. *Physics of Condensed Matter*; Elsevier Science, 2011.

[46] Chen, J.; Xu, Z.; Chen, Y. *Electronic structure and surfaces of sulfide minerals: Density functional theory and applications*; Elsevier, 2020.

[47] Santosh K. Tiwari, A. H. R. O. A. D. A., Vijay Kumar; Nayak, G. C. Magical Allotropes of Carbon: Prospects and Applications. *Critical Reviews in Solid State and Materials Sciences* **2016**, *41*, 257–317.

[48] Sang, M.; Shin, J.; Kim, K.; Yu, K. J. Electronic and thermal properties of graphene and recent advances in graphene based electronics applications. *Nanomaterials* **2019**, *9*, 374.

[49] Luo, S.; Wang, Y.; Tong, X.; Wang, Z. Graphene-based optical modulators. *Nanoscale research letters* **2015**, *10*, 1–11.

[50] Liu, Z.; Zhang, X.; Yan, X.; Chen, Y.; Tian, J. Nonlinear optical properties of graphene-based materials. *Chinese science bulletin* **2012**, *57*, 2971–2982.

[51] Li, X.; Colombo, L.; Ruoff, R. S. Synthesis of graphene films on copper foils by chemical vapor deposition. *Advanced Materials* **2016**, *28*, 6247–6252.

[52] Lee, H. W.; Yonn, Y. Selective dispersion of high purity semiconducting single-walled carbon nanotubes with regioregular poly(3-alkylthiophene)s. *Nat. Commun.* **2011**, *2*, 541.

[53] Bhuyan, M. S. A.; Uddin, M. N.; Islam, M. M.; Bipasha, F. A.; Hossain, S. S. Synthesis of graphene. *International Nano Letters* **2016**, *6*, 65–83.

[54] Berger, C.; Song, Z.; Li, T.; Li, X.; Ogbazghi, A. Y.; Feng, R.; Dai, Z.; Marchenkov, A. N.; Conrad, E. H.; First, P. N.; de Heer, W. A. Ultrathin Epitaxial Graphite: 2D Electron Gas Properties and a Route toward Graphene-based Nanoelectronics. *The Journal of Physical Chemistry B* **2004**, *108*, 19912–19916.

[55] Raman Spectroscopy. `https://www.horiba.com/fra/scientific/technologies/raman-imaging-and-spectroscopy/raman-spectroscopy/`, Accessed: 2023-11-17.

[56] Polina S. Fomina, B. M. . D. S. V., Mikhail A. Proskurnin Infrared Spectroscopy in Aqueous Solutions: Capabilities and Challenges. *Critical Reviews in Analytical Chemistry* **2023**, 1748–1765.

[57] Szymanski, H. A. *Raman Spectroscopy: Theory and Practice*; Springer New York, NY, 2012; pp 1–3.

[58] Smith, D. G., E. *Modern Raman Spectroscopy*; John Wiley Sons.Ltd, 2005.

[59] Herziger, F. *Double-resonant Raman scattering in graphene, few-layer graphene, and carbon nan-otubes*; Technische Universitaet Berlin (Germany), 2015.

[60] Jones, H. D. Z. L. e. a., R.R. Raman Techniques: Fundamentals and Frontiers. *Nanoscale Research Letters* **2019**, 3–4.

[61] Childres, I.; Jauregui, L. A.; Park, W.; Cao, H.; Chen, Y. P. Raman spectroscopy of graphene and related materials. *New developments in photon and materials research* **2013**, *1*, 1–20.

[62] Graf, D.; Molitor, F.; Ensslin, K.; Stampfer, C.; Jungen, A.; Hierold, C.; Wirtz, L. Spatially resolved Raman spectroscopy of single-and few-layer graphene. *Nano letters* **2007**, *7*, 238–242.

[63] Malard, L. M.; Pimenta, M. A.; Dresselhaus, G.; Dresselhaus, M. S. Raman spectroscopy in graphene. *Physics reports* **2009**, *473*, 51–87.

[64] Lucchese, M. M.; Stavale, F.; Ferreira, E. M.; Vilani, C.; Moutinho, M. V. d. O.; Capaz, R. B.; Achete, C. A.; Jorio, A. Quantifying ion-induced defects and Raman relaxation length in graphene. *Carbon* **2010**, *48*, 1592–1597.

[65] Heo, G.; Kim, Y.; Chun, S.-H.; Seong, M.-J. Polarized Raman spectroscopy with differing angles of laser incidence on single-layer graphene. *Nanoscale Research Letters* **2015**, *10*.

[66] Cançado, L. G.; Jorio, A.; Ferreira, E. H. M.; Stavale, F.; Achete, C. A.; Capaz, R. B.; Moutinho, M. V. O.; Lombardo, A.; Kulmala, T. S.; Ferrari, A. C. Quantifying Defects in Graphene via Raman Spectroscopy at Different Excitation Energies. *Nano Letters* **2011**, *11*, 3190–3196.

[67] Mishra, R.; Militky, J. In *Nanotechnology in Textiles*; Mishra, R., Militky, J., Eds.; The Textile Institute Book Series; Woodhead Publishing, 2019; pp 163–179.

[68] Margadonna, S.; Prassides, K. Fullerenes. *Encyclopedia of Materials: Science and Technology* **2001**, 3379–3383.

[69] Pan, Y.; Liu, X.; Zhang, W.; Liu, Z.; Zeng, G.; Shao, B.; Liang, Q.; He, Q.; Yuan, X.; Huang, D.; Chen, M. Advances in photocatalysis based on fullerene C60 and its derivatives: Properties, mechanism, synthesis, and applications. *Applied Catalysis B: Environmental* **2020**, *265*, 118579.

[70] Maruyama, T. In *Handbook of Carbon-Based Nanomaterials*; Thomas, S., Sarathchandran, C., Ilangovan, S., Moreno-Piraján, J. C., Eds.; Micro and Nano Technologies; Elsevier, 2021; pp 299–319.

[71] You, P.; Kamarudin, S. Recent progress of carbonaceous materials in fuel cell applications: An overview. *Chemical Engineering Journal* **2017**, *309*, 489–502.

[72] Inagaki, M.; Kang, F.; Toyoda, M.; Konno, H. In *Advanced Materials Science and Engineering of Carbon*; Inagaki, M., Kang, F., Toyoda, M., Konno, H., Eds.; Butterworth-Heinemann: Boston, 2014; pp 15–40.

[73] Hazen, R. M.; Downs, R. T.; Jones, A. P.; Kah, L. Carbon mineralogy and crystal chemistry. *Reviews in Mineralogy and Geochemistry* **2013**, *75*, 7–46.

[74] Sengupta, R.; Bhattacharya, M.; Bandyopadhyay, S.; Bhowmick, A. K. A review on the mechanical and electrical properties of graphite and modified graphite reinforced polymer composites. *Progress in Polymer Science* **2011**, *36*, 638–670, Special Issue on Conducting Polymers.

[75] Gyngard, F.; Zinner, E.; Nittler, L. R.; Morgand, A.; Stadermann, F. J.; Hynes, K. M. Automated NanoSIMS measurements of spinel stardust from the Murray meteorite. *The Astrophysical Journal* **2010**, *717*, 107.

[76] Yazdi, G. R.; Iakimov, T.; Yakimova, R. Epitaxial graphene on SiC: a review of growth and characterization. *Crystals* **2016**, *6*, 53.

[77] Liu, G.; Tuttle, B. R.; Dhar, S. Silicon carbide: A unique platform for metal-oxide-semiconductor physics. *Applied Physics Reviews* **2015**, *2*.

[78] Abderrazak, H.; Hmida, E. Silicon carbide: synthesis and properties. *Properties and applications of Silicon Carbide* **2011**, 361–388.

[79] Kimoto, T.; Cooper, J. A. *Fundamentals of silicon carbide technology: growth, characterization, devices and applications*; John Wiley & Sons, 2014.

[80] Tairov, Y. M.; Tsvetkov, V. Investigation of growth processes of ingots of silicon carbide single crystals. *Journal of crystal growth* **1978**, *43*, 209–212.

[81] Guy, O.; Lodzinski, M.; Teng, K.; Maffeis, T.; Tan, M.; Blackwood, I.; Dunstan, P.; Al-Hartomy, O.; Wilks, S.; Wilby, T.; Rimmer, N.; Lewis, D.; Hopkins, J. Investigation of the 4H–SiC surface. *Applied Surface Science* **2008**, *254*, 8098–8105, V International Workshop on Semiconductor Surface Passivation.

[82] Lyakhovich, V. Origin of accessory moissanite. *International Geology Review* **1980**, *22*, 961–970.

[83] Di Pierro, S.; Gnos, E.; Grobety, B. H.; Armbruster, T.; Bernasconi, S. M.; Ulmer, P. Rock-forming moissanite (natural α-silicon carbide). *American Mineralogist* **2003**, *88*, 1817–1821.

[84] Nakashima, S.-i.; Harima, H. Raman investigation of SiC polytypes. *physica status solidi (a)* **1997**, *162*, 39–64.

[85] Bunaciu, A. A.; UdriŞTioiu, E. G.; Aboul-Enein, H. Y. X-ray diffraction: instrumentation and applications. *Critical reviews in analytical chemistry* **2015**, *45*, 289–299.

[86] Frentrup, M.; Lee, L. Y.; Sahonta, S.-L.; Kappers, M. J.; Massabuau, F.; Gupta, P.; Oliver, R. A.; Humphreys, C. J.; Wallis, D. J. X-ray diffraction analysis of cubic zincblende III-nitrides. *Journal of Physics D: Applied Physics* **2017**, *50*, 433002.

[87] Sun, S.; Zhang, X.; Cui, J.; Liang, S. Identification of the Miller indices of a crystallographic plane: a tutorial and a comprehensive review on fundamental theory, universal methods based on different case studies and matters needing attention. *Nanoscale* **2020**, *12*, 16657–16677.

[88] Ameh, E. A review of basic crystallography and x-ray diffraction applications. *The international journal of advanced manufacturing technology* **2019**, *105*, 3289–3302.

[89] Mas'udah, K. W.; Diantoro, M.; Fuad, A. *Synthesis and structural analysis of silicon carbide from silica rice husk and activated carbon using solid-state reaction*; 2018; Vol. 1093; p 012033.

[90] Iwanowski, R.; Fronc, K.; Paszkowicz, W.; Heinonen, M. XPS and XRD study of crystalline 3C-SiC grown by sublimation method. *Journal of alloys and compounds* **1999**, *286*, 143–147.

[91] Yang, Z.; Yin, Z.; Zhao, Z.; Yu, J.; Ren, Z.; Yu, G.; Zhang, G. Effect of sintering aids on microstructure and properties of textured SiC ceramics prepared in 6 T. *Journal of Asian Ceramic Societies* **2021**, *9*, 85–95.

[92] Zhiying, h.; Zheng, D.; Tu, R.; Yang, M.; Li, Q.; Han, M.; Zhang, S.; Zhang, L.; Goto, T. Structural Controlling of Highly-Oriented Polycrystal 3C-SiC Bulks via Halide CVD. *Materials* **2019**, *12*, 390.

[93] Daulton, T.; Bernatowicz, T.; Lewis, R.; Messenger, S.; Stadermann, F.; Amari, S. Polytype distribution of circumstellar silicon carbide: Microstructural characterization by transmission electron microscopy. *Geochimica et Cosmochimica Acta* **2003**, *67*, 4743–4767.

[94] Anders, E.; Zinner, E. Interstellar grains in primitive meteorites: Diamond, silicon carbide, and graphite. *Meteoritics* **1993**, *28*, 490–514.

[95] Amari, S.; Lewis, R. S.; Anders, E. Interstellar grains in meteorites: I. Isolation of SiC, graphite and diamond; size distributions of SiC and graphite. *Geochimica et Cosmochimica Acta* **1994**, *58*, 459–470.

[96] Virag, A.; Wopenka, B.; Amari, S.; Zinner, E.; Anders, E.; Lewis, R. S. Isotopic, optical, and trace element properties of large single SiC grains from the Murchison meteorite. *Geochimica et cosmochimica acta* **1992**, *56*, 1715–1733.

[97] Ehrenfreund, P.; Sephton, M. A. Carbon molecules in space: from astrochemistry to astrobiology. *Faraday discussions* **2006**, *133*, 277–288.

[98] Zamirri, L.; Casassa, S.; Rimola, A.; Segado-Centellas, M.; Ceccarelli, C.; Ugliengo, P. IR spectral fingerprint of carbon monoxide in interstellar water–ice models. *Monthly Notices of the Royal Astronomical Society* **2018**, *480*, 1427–1444.

[99] Dartois, E. Interstellar carbon dust. *C* **2019**, *5*, 80.

[100] Lépine-Szily, A.; Descouvemont, P. Nuclear astrophysics: nucleosynthesis in the Universe. *International Journal of Astrobiology* **2012**, *11*, 243–250.

[101] Prantzos, N. In *Lectures in Astrobiology: Volume II*; Gargaud, M., Martin, H., Claeys, P., Eds.; Springer Berlin Heidelberg: Berlin, Heidelberg, 2007; pp 1–43.

[102] Ziurys, L.; Halfen, D.; Geppert, W.; Aikawa, Y. Following the interstellar history of carbon: from the interiors of stars to the surfaces of planets. *Astrobiology* **2016**, *16*, 997–1012.

[103] Jeltema, T. E.; Sher, M. Triple-alpha process and the anthropically allowed values of the weak scale. *Physical Review D* **1999**, *61*.

[104] Herwig, F. Evolution of Asymptotic Giant Branch Stars. *Annual Review of Astronomy and Astrophysics* **2005**, *43*, 435–479.

[105] Ishihara, D.,; Kaneda, H.,; Onaka, T.,; Ita, Y.,; Matsuura, M.,; Matsunaga, N., Galactic distributions of carbon- and oxygen-rich AGB stars revealed by the AKARI mid-infrared all-sky survey. *AA* **2011**, *534*, A79.

[106] Kaiser, R. I. Experimental Investigation on the Formation of Carbon-Bearing Molecules in the Interstellar Medium via NeutralNeutral Reactions. *Chemical Reviews* **2002**, *102*, 1309–1358, PMID: 11996539.

[107] McCarthy, M. C.; Gottlieb, C. A.; Cernicharo, J. Building blocks of dust: A coordinated laboratory and astronomical study of the archtype AGB carbon star IRC+10216. *Journal of Molecular Spectroscopy* **2019**, *356*, 7–20.

[108] Hasegawa, T. I.; Kwok, S. Neutral Carbon in Post-Asymptotic Giant Branch Stars and Planetary Nebulae. *The Astrophysical Journal* **2003**, *585*, 475.

[109] Guzman-Ramirez, L.; Lagadec, E.; Wesson, R.; Zijlstra, A. A.; Mller, A.; Jones, D.; Boffin, H. M.; Sloan, G. C.; Redman, M. P.; Smette, A. Witnessing the emergence of a carbon star. *Monthly Notices of the Royal Astronomical Society: Letters* **2015**, *451*, L1–L5.

[110] Patra, N.; Král, P.; Sadeghpour, H. Nucleation and stabilization of carbon-rich structures in interstellar media. *The Astrophysical Journal* **2014**, *785*, 6.

[111] Thakur, A. K.; Muralidharan, K.; Zega, T. J.; Ziurys, L. A nanometric window on fullerene formation in the interstellar medium: Insights from molecular dynamics studies. *The Journal of Chemical Physics* **2022**, *156*.

[112] Bernal, J.; Haenecour, P.; Howe, J.; Zega, T.; Amari, S.; Ziurys, L. Formation of Interstellar C 60 from Silicon Carbide Circumstellar Grains. *The Astrophysical Journal* **2019**, *883*, L43.

[113] Chiar, J.; Tielens, A.; Adamson, A.; Ricca, A. The structure, origin, and evolution of interstellar hydrocarbon grains. *The Astrophysical Journal* **2013**, *770*, 78.

[114] Bernatowicz, T. J.; Croat, T. K.; Daulton, T. L. Origin and evolution of carbonaceous presolar grains in stellar environments. *Meteorites and the early solar system II* **2006**, 109–126.

[115] Díaz-Cano, L. S.; Jones, A. Carbonaceous dust in interstellar shock waves: hydrogenated amorphous carbon (aC: H) vs. graphite. *Astronomy & Astrophysics* **2008**, *492*, 127–133.

[116] Scott, A.; Duley, W. The decomposition of hydrogenated amorphous carbon: a connection with polycyclic aromatic hydrocarbon molecules. *The Astrophysical Journal* **1996**, *472*, L123.

[117] Dartois, E.; Engrand, C.; Brunetto, R.; Duprat, J.; Pino, T.; Quirico, E.; Remusat, L.; Bardin, N.; Briani, G.; Mostefaoui, S. Interstellar and interplanetary carbonaceous solids in the laboratory. *Geochemical Journal* **2014**, *48*, 511–518.

[118] Huss, G. R. Meteoritic Nanodiamonds: Messengers from the Stars. *Elements* **2005**, *1*, 97–100.

[119] Clayton, D.; Meyer, B.; Sanderson, C.; Russell, S.; Pillinger, C. Carbon and Nitrogen Isotopes in Type II Supernova Diamonds. *The Astrophysical Journal* **1995**, *447*, 894.

[120] Ustinova, G. Production of anomalous Xe in nanodiamond in chondrites during the last supernova explosion predating the origin of the Solar system. *Geochemistry International* **2011**, *49*, 555–567.

[121] Merino, P.; Švec, M.; Martinez, J.; Jelinek, P.; Lacovig, P.; Dalmiglio, M.; Lizzit, S.; Soukiassian, P.; Cernicharo, J.; Martin-Gago, J. Graphene etching on SiC grains as a path to interstellar polycyclic aromatic hydrocarbons formation. *Nature Communications* **2014**, *5*, 3054.

[122] King, A.; Henkel, T.; Chapman, S.; Busemann, H.; Rost, D.; Guillermier, C.; Lee, M.; Franchi, I.; Lyon, I. Amorphous carbon grains in the Murchison meteorite. **2011**,

[123] Fries, M.; Steele, A. Graphite whiskers in CV3 meteorites. *Science* **2008**, *320*, 91–93.

[124] Karczemska, A. Diamonds in meteorites–Raman mapping and cathodoluminescence studies. *J. Achiev. Materials Manufact. Eng* **2010**, *43*, 94–107.

[125] Nuth, J. A.; Kimura, Y.; Lucas, C.; Ferguson, F.; Johnson, N. M. The formation of graphite whiskers in the primitive solar nebula. *The Astrophysical Journal Letters* **2010**, *710*, L98.

[126] Bolser, D.; Zega, T. J.; Asaduzzaman, A.; Bringuier, S.; Simon, S. B.; Grossman, L.; Thompson, M. S.; Domanik, K. J. Microstructural analysis of Wark-Lovering rims in the Allende and Axtell CV 3 chondrites: Implications for high-temperature nebular processes. *Meteoritics & Planetary Science* **2016**, *51*, 743–756.

[127] Imin Kao, C. C. *Wafer Manufacturing*; John Wiley Sons, Ltd, 2021; Chapter 3, pp 71–96.

[128] Gutierrez, R. M. P.; Mendez, J. V. M.; Vazquez, I. A. In *Nanostructures for Oral Medicine*; Andronescu, E., Grumezescu, A. M., Eds.; Micro and Nano Technologies; Elsevier, 2017; pp 27–59.

[129] Ungár, T. Microstructural parameters from X-ray diffraction peak broadening. *Scripta Materialia* **2004**, *51*, 777–781, Viewpoint set no. 35. Metals and alloys with a structural scale from the micrometer to the atomic dimensions.

[130] Holder, C. F.; Schaak, R. E. Tutorial on Powder X-ray Diffraction for Characterizing Nanoscale Materials. *ACS Nano* **2019**, *13*, 7359–7365.

[131] Pierro, S.; Gnos, E.; Grobety, B.; Armbruster, T.; Früeh-Green, G.; Ulmer, P. Rock-forming moissanite (Natural -silicon carbide). *Am Mineral* **2003**, *88*.

[132] Karamat, S.; Sonuşen, S.; Çelik, ; Uysallı, Y.; Özgönül, E.; Oral, A. Synthesis of few layer single crystal graphene grains on platinum by chemical vapour deposition. *Progress in Natural Science: Materials International* **2015**, *25*, 291–299.

[133] Papanai, G. S.; Sharma, I.; Gupta, B. K. Probing number of layers and quality assessment of mechanically exfoliated graphene via Raman fingerprint. *Materials Today Communications* **2020**, *22*, 100795.

[134] Shlimak, I.; Butenko, A.; Kogan, E.; Kaveh, M. Irradiation-induced broadening of the Raman spectra in monolayer graphene. *Journal of Applied Physics* **2019**, *126*.

[135] Ni, Z.; Wang, Y.; Yu, T.; Shen, Z. Raman spectroscopy and imaging of graphene. *Nano Research* **2008**, *1*, 273–291.

[136] Pitsch, S. A.; Sumathi, R. R. Effect of Polar Faces of SiC on the Epitaxial Growth of Graphene: Growth Mechanism and Its Implications for Structural and Electrical Properties. *Crystals* **2023**, *13*, 189.

[137] Eckmann, A.; Felten, A.; Mishchenko, A.; Britnell, L.; Krupke, R.; Novoselov, K. S.; Casiraghi, C. Probing the nature of defects in graphene by Raman spectroscopy. *Nano letters* **2012**, *12*, 3925–3930.

[138] Ben Gouider Trabelsi, A.; Kusmartsev, F.; Gaifullin, M.; Forrester, M.; Kusmartseva, A.; Oueslati, M. Epitaxial Graphene morphological imperfections: from a hindrance to the generation of new photo-responses in the visible domain. *Nanoscale* **2017**, *9*.

[139] Vecera, P.; Chacón-Torres, J. C.; Pichler, T.; Reich, S.; Soni, H. R.; Görling, A.; Edelthalhammer, K.; Peterlik, H.; Hauke, F.; Hirsch, A.; Hirsch, A. Precise determination of graphene functionalization by in situ Raman spectroscopy. *Nature communications* **2017**, *8*, 15192.

[140] Basta, L.; Bianco, F.; Moscardini, A.; Fabbri, F.; Bellucci, L.; Tozzini, V.; Heun, S.; Veronesi, S. Deterministic Covalent Organic Functionalization of Monolayer Graphene with 1, 3-Dipolar Cycloaddition Via High Resolution Surface Engineering. *arXiv preprint arXiv:2202.06609* **2022**,

[141] Pravdivtseva, O.; Tissot, F.; Dauphas, N.; Amari, S. Evidence of presolar SiC in the Allende Curious Marie calcium–aluminium-rich inclusion. *Nature astronomy* **2020**, *4*, 617–624.

[142] Davidson, J.; Busemann, H.; Alexander, C.; Nittler, L.; Hoppe, P.; Franchi, I.; Grady, M. Were Presolar Grains Destroyed by the Nebular Process Responsible for the Volatile Element Fractionation? **2008**,